
PE&RS
June 2023
Volume 89, Number 6
The official journal for imaging and geospatial information science and technology
PHOTOGRAMMETRIC ENGINEERING & REMOTE SENSING

2023 ASPRS International Technical Symposium

June 12-16, 2023
VIRTUAL

ASPRS is happy to announce the dates of its virtual conference. The 2023 ASPRS International Technical Symposium will take place.

The symposium will consist of:

- 15-minute oral presentations
- 5-minute Ignite-style presentations
- Poster Gallery
- Sustaining Member Vendor Spotlights
- ASPRS Society Highlights

Sessions will run each day from 10:00 AM to 6:00 PM Eastern Daylight Time (UTC - 4). All sessions will be recorded and made available on-demand to conference registrants. Presenters are eligible to submit full manuscripts for publication in the ISPRS Archives.

Registration Fees

• ASPRS Member	$150 USD
• ASPRS Student Member	$ 50 USD
• ASPRS Emeritus Member	$ 25 USD
• Non Member	$250 USD

Sponsorship Opportunities

- Vendor Spotlight/Product Demo
- Day Sponsor
- Session Sponsor
- Workshop Sponsor

"We are happy to offer this educational opportunity to the geospatial community. Virtual events are an excellent way to exchanammunity without the cost and time constraints of travel," said Karen Schuckman, ASPRS Executive Director

https://my.asprs.org/2023Symposium/

ANNOUNCEMENTS

NV5 Global, Inc., a provider of technology, conformity assessment, and consulting solutions, announced today the closing of its acquisition of L3Harris Technologies, Inc.'s Visual Information Solutions commercial geospatial technology and software business ("VIS"). First announced in December, the acquisition has received regulatory approvals and enhances NV5's position as North America's premiere provider of geospatial data solutions, accompanying the acquisition of Axim Geospatial completed earlier this year.

"This acquisition supports NV5's expansion in a subscription-based geospatial product and service model and strengthens our role in supporting the nation's defense and intelligence communities through geospatial information management and analytics," said Dickerson Wright, PE, Chairman and CEO of NV5. "As the only provider of software solutions to analyze over 200 geospatial data types and comprehensive in-house lidar, topobathymetric lidar, and full ocean depth sonar capabilities, NV5 has built a distinct competitive advantage and robust platform to support accelerated organic growth."

The VIS acquisition includes 16 U.S. Patents for geospatial data analytics. NV5 will also receive ownership of an additional 13 U.S. and non-U.S. Trademark Registrations for leading geospatial software applications with approximately 500,000 global users. These software products include prominent applications such as ENVI, IDL, Jagwire, Amplify, and Helios, which are relied upon by the United States Department of Defense and federal civilian agencies for the analysis and management of geospatial data.

For more information on NV5, visit www.nv5.com.

UP42, the geospatial developer platform and marketplace, has significantly expanded its aerial imagery and elevation data portfolio through a partnership with **Vexcel**–a 30-year industry leader in the photogrammetric and remote sensing space. The Vexcel Data Program delivers geospatial data products with high accuracy, spatial resolution, and consistency.

Vexcel's aerial data collection initiative is the largest in the world capturing ultra-high-resolution imagery (at 7.5 to 15cm resolution) and related geospatial data in more than 30 countries, including the U.S., Canada, U.K., Western and Eastern Europe, Australia, New Zealand, and Japan. Known for their remarkable image quality, Vexcel products are used extensively by local governments, utilities, telecoms, and AEC (architecture, engineering, construction) companies.

"With a rich heritage in the geospatial industry, the Vexcel name is synonymous with reliability and quality," said Sean Wiid, CEO of UP42. "Our partnership with Vexcel highlights UP42's commitment to offer our customers a portfolio of products that continues to grow in diversity and geographic coverage."

Vexcel has built its excellent reputation over decades in the geospatial sector, first as developer of the market-leading UltraCam airborne sensor line deployed globally by aerial mappers. Leveraging the UltraCam's ultra-high resolution and accuracy combined with world-class processing software, Vexcel launched its data collection program and amassed a comprehensive library of cloud-based aerial imagery and elevation data.

"Our aerial data helps end users solve some of the toughest geospatial challenges, especially when it comes to infrastructure and asset management," shared Jason Jones, Director of Channels and Alliances for Vexcel. "End users are able to support better decision-making, enhance workflows, and generate more accurate automated insights using our premium imagery. We're thrilled our partnership with UP42 provides this opportunity to their customers."

The clear and accurate Vexcel aerial imagery now available on the UP42 marketplace enables users to gain greater context and insights from the world around them. These products include: oblique and true ortho urban images at 7.5 cm resolution, or better; orthos at 15-20 cm; and Digital Surface Models (DSM) at 7.5cm resolution and Digital Terrain Models (DTM) at 15-20 cm resolution

The consistent quality of Vexcel image products across all geographic locations delivers insights and analysis in a variety of applications, including: vegetation management and infrastructure monitoring by energy utilities and telecommunication companies; vite inspection and property assessment by AEC firms; and urban planning and environmental protection by local governments.

"We launched UP42 with the objective of becoming the one-stop-shop that changes the way geospatial data is accessed and analyzed — and our partnership with Vexcel further assists us in achieving that goal," said UP42's Wiid.

For more information visit https://vexceldata.com/au or https://up42.com.

ACCOMPLISHMENTS

Dewberry, a privately held professional services firm, has announced that Executive Vice President and Federal Market Leader Phil Thiel has been named to the National Geospatial Advisory Committee (NGAC) by the U.S. Department of the Interior.

The NGAC provides advice and recommendations on national geospatial policy and management issues, the development of the National Spatial Data Infrastructure (NSDI), and the implementation of the Geospatial Data Act of 2018.

Thiel serves as principal-in-charge for Dewberry's major geospatial contracts with the Federal Emergency Management Agency, National Oceanic and Atmospheric Administration, U.S. Army Corps of Engineers, U.S. Fish and Wildlife Service, U.S. Geological Survey, and numerous other federal agencies and clients, providing surveying, remote sensing, geographic information systems, information technology, and other professional services.

"The National Geospatial Advisory Committee plays a vital role in advancing the nation's adoption and implementation of geospatial technologies, and I'm truly honored and humbled to join the committee," Thiel says.

For more information on Dewberry, visit www.dewberry.com.

In December 2022, the US joined an international coalition committed to preserving 30 percent of the planet's lands and oceans by 2030, an initiative known as 30 by 30. An inherently geographic issue, one major tool already in use to achieve this goal is mapping technology. **Esri**, the global leader in location intelligence, has been at the forefront of applying maps and analytics to conservation since its inception. One key mission for founders Jack and Laura Dangermond has been understanding the connection between humans and the planet to help build a more sustainable world. In recognition of their work, the International Land Conservation Network (ILCN) has awarded Jack and Laura Dangermond the Conservation Visionary Award.

"We have always been passionate about protecting the natural world, and this award is an incredible honor for us," said Jack Dangermond, Esri founder and president. "We hope our work inspires and motivates individuals and other organizations to pursue similar opportunities to conserve remaining natural areas important to the health of our planet, especially as we embark on the ambitious goal of protecting a third of the planet's lands and oceans."

Jack and Laura Dangermond founded Esri in Redlands, California in 1969, and it is now the leading geographic information system (GIS) software company in the world. Esri has supported environmental efforts by offering low-cost access to software, content, and resources through its Nonprofit Organization Program. The company has also donated or pledged more than $1 billion worth of free Esri software to schools and environmental organizations.

In addition to company support, the Dangermonds personally established the Jack and Laura Dangermond Preserve at Point Conception, California, in 2017. Their $165 million donation to The Nature Conservancy helped protect 24,000 acres of California's central coastal land. Currently, the organization is building a digital twin of the preserve available online, and empowering researchers to study the preserve from anywhere in the world.

The ILCN connects civic and private organizations around the world to accelerate the protection and strengthen land and natural resource management. The organization's Conservation Visionary Award honors individuals who have made outstanding contributions to the field of conservation. Recent awardees have included Minister of the Environment of Chile, Marcelo Mena; Director for Biodiversity in the European Commission's Directorate General for the Environment, Humberto Delgado Rosa; and Conservation Director at the Fundacion Catalunya al Pedrera, Miquel Rafa Fornieles.

The Dangermonds' award was presented to Jack and Laura at the 2023 Esri Geodesign Summit.

For more information on Esri, visit www.esri.com.

CALENDAR

- 12-16 June, **ASPRS 2023 International Technical Symposium.** For more information, visit https://my.asprs.org/2023Symposium/.
- 16-19 October, **GIS-Pro 2023**, Columbus, Ohio. For more information, visit www.urisa.org/gis-pro.

PE&RS
PHOTOGRAMMETRIC ENGINEERING & REMOTE SENSING
The official journal for imaging and geospatial information science and technology
June 2023 Volume 89 Number 6

COLUMNS

ANNOUNCEMENTS

DEPARTMENTS

See the Cover Description on Page 336

COVER DESCRIPTION

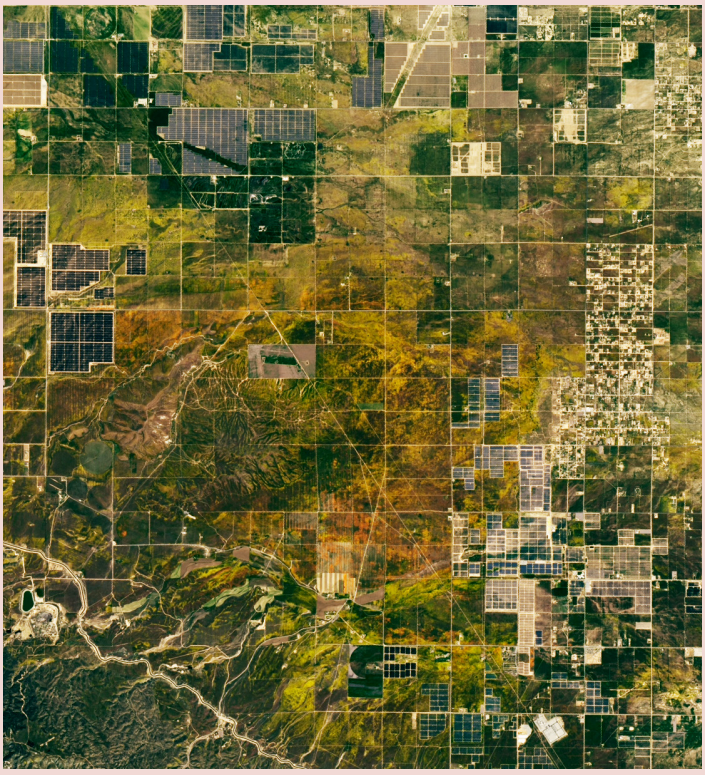

A bright spot has emerged after California's particularly wet and dreary winter: a sea of wildflowers in Southern California. In the western tip of the Mojave Desert, orange, gold, and yellow flowers have flooded the valleys and hills of Antelope Valley California Poppy Reserve.

On April 7, 2023, the Operational Land Imager (OLI) on Landsat 8 acquired the image (cover) of the valley. Bright golden-orange California poppies (Eschscholzia californica) are on full display with yellow California goldfields (Lasthenia californica), among other species of flowers.

On April 15, 2023, the Operational Land Imager-2 (OLI) on Landsat 9 captured another vibrant view of the bloom (above). By this time, the golden-orange poppies had faded in places, while canary yellow flowers in the upper left of the image pop out. The yellow flowers are surrounded by panels from a solar farm.

During the same week in April 2020, orange hues of the California poppy dominated images of the reserve. But in these views in 2023, a mosaic of orange and yellow is on display.

Although wildflowers make their appearance on these hills almost every spring, this year California is experiencing a larger "super bloom." Much of California had a wetter-than-average winter, and this abundant precipitation fuels the large wildflower blooms.

For more information, visit https://landsat.visibleearth.nasa.gov/view.php?id=151227.

NASA Earth Observatory images by Lauren Dauphin, using Landsat data from the U.S. Geological Survey. Story by Emily Cassidy.

asprs
THE IMAGING & GEOSPATIAL INFORMATION SOCIETY

PHOTOGRAMMETRIC ENGINEERING & REMOTE SENSING

JOURNAL STAFF

Publisher ASPRS
Editor-In-Chief Alper Yilmaz
Director of Publications Rae Kelley
Electronic Publications Manager/Graphic Artist
Matthew Austin

Photogrammetric Engineering & Remote Sensing is the official journal of the American Society for Photogrammetry and Remote Sensing. It is devoted to the exchange of ideas and information about the applications of photogrammetry, remote sensing, and geographic information systems. The technical activities of the Society are conducted through the following Technical Divisions: Geographic Information Systems, Photogrammetric Applications, Lidar, Primary Data Acquisition, Professional Practice, Remote Sensing Applications, and Unmanned Autonomous Systems. Additional information on the functioning of the Technical Divisions and the Society can be found in the Yearbook issue of *PE&RS*.

All written correspondence should be directed to the American Society for Photogrammetry and Remote Sensing, PO Box 14713, Baton Rouge, LA 70898, including general inquiries, memberships, subscriptions, business and editorial matters, changes in address, manuscripts for publication, advertising, back issues, and publications. The telephone number of the Society Headquarters is 301-493-0290; the fax number is 225-408-4422; web address is www.asprs.org.

PE&RS. *PE&RS* (ISSN0099-1112) is published monthly by the American Society for Photogrammetry and Remote Sensing, 8550 United Plaza Blvd, Suite 1001, Baton Rouge, Louisiana 70809 . Periodicals postage paid at Bethesda, Maryland and at additional mailing offices.

SUBSCRIPTION. *PE&RS* is available as an e-Subscription (single-site and multi-site licenses) and an e-Subscription with print add-on (single-site license only). PE&RS subscriptions are on a calendar-year, beginning in January and ending in December.

The rate for a single-site e-Subscription for the USA/Non-USA is $1040 USD, for Canadian* is $1092 USD.

The rate for a multi-site e-Subscription for the USA/Non-USA is $1040 USD plus $250 USD for each additional license, for Canadian* is $1092 USD plus $263 for each additional license.

The rate for e-Subscription with print add-on for the USA is $1525 USD, for Canadian* is $1612 USD, and for Non-USA is $1565 USD.

*Note: Subscription prices for Canada includes 5% of the total amount for Canada's Goods and Services Tax (GST #135123065). **PLEASE NOTE: All Subscription Agencies receive a 20.00 USD discount.**

POSTMASTER. Send address changes to PE&RS, ASPRS, PO Box 14713, Baton Rouge, LA 70898. CDN CPM #(40020812).

MEMBERSHIP. Membership is open to any person actively engaged in the practice of photogrammetry, photointerpretation, remote sensing and geographic information systems; or who by means of education or profession is interested in the application or development of these arts and sciences. Membership is for one year, with renewal based on the anniversary date of the month joined. Membership Dues include a 12-month electronic subscription to *PE&RS*. Annual Individual Membership dues are $175.00 USD and Student Membership dues are $50.00 USD. A tax of 5% for Canada's Goods and Service Tax (GST #135123065) is applied to all members residing in Canada.

Top Geospatial Trends to Watch in 2023

by Qassim Abdullah, Ph.D., PLS, CP
Woolpert Vice President
and Chief Scientist

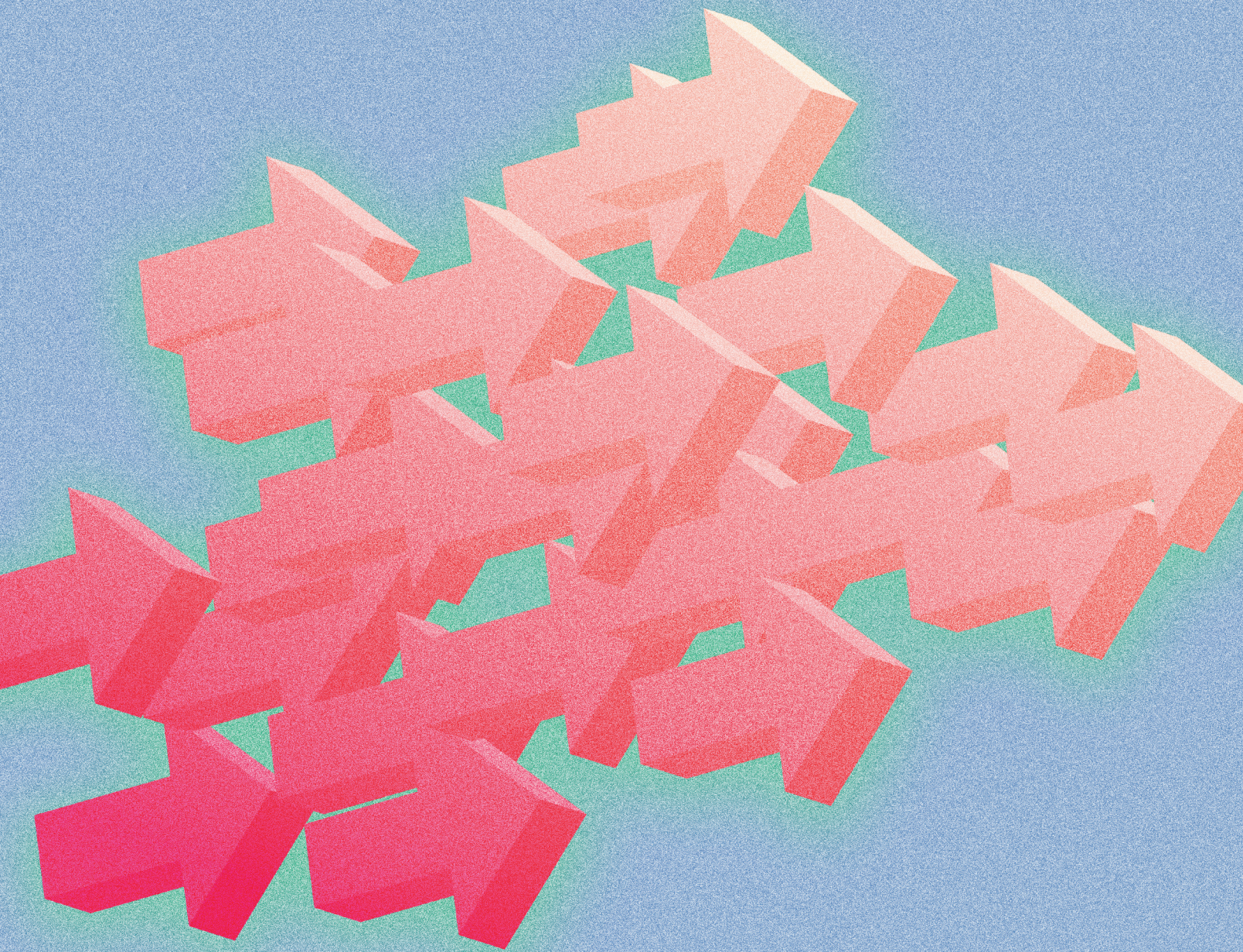

For the last six years, I have been writing this "Top Geospatial Trends" column, which is usually published in January or February. Some years, the columns write themselves, as advancements in the industry emerge or innovative perspectives demand input and conversation. This year, because the industry is still working to shake off the dust from the pandemic, this column is being published in June.

For this year's edition, I'll revisit how the trends highlighted last year fared and if they will continue to shape our year ahead, spotlight some things to watch in the last half of 2023, and provide my perspective about the future of geospatial through the lens of our revised American Society for Photogrammetry and Remote Sensing (ASPRS) Accuracy Standards for Digital Geospatial Data, which are due to be published later this year.

>Navigating Recovery, Gaining Strength

Four months into 2023, the pandemic continues to impact the geospatial industry. In 2021 and 2022, supply chains and productivity were disrupted, leading to shortages of critical materials, parts, and products, some of which compromised vital survey hardware. However, our industry has shown resilience as many companies and manufacturers have implemented new workplace safety protocols, increased automation, and diversified supply chains to mitigate the impact of future disruptions. In addition, geospatial hardware manufacturers have continued to advance new and unique capabilities for data acquisition.

Digital Twin: Last year, I shared how BIM and GIS provide the foundation for digital twin, and how the nearly synonymous term of "metaverse" was gaining traction. Over the last year, the collective benefits and returns on investment for the digital twin have continued to expand. As the value of the digital twin is increasingly realized, demand for this technology will skyrocket. A digital twin is a digital replica of a physical environment, whether it is an asset, process, highway corridor, river, ocean, or even the Earth. This digital representation comprises the entire life cycle of the asset or the project, from the planning stage to design and construction, and continuing through operating the asset—all in one place.

Since the digital twin mimics the real-world characteristics of the physical environment in real time, with the help of Internet of Things (IoT) sensors, a facility engineer can remotely observe the operational environment of a building to manage environmental controls, power consumption, air quality, fire alarm systems, etc. A city emergency response team can simulate disaster scenarios to identify evacuation routes and aid access through a digital twin, or a port authority can manage its assets and port operations, guiding incoming and outgoing ships through its navigation channel by way of precision navigation. This capability can save billions of dollars at commercial ports that have restricted visibility due to fog or other environmental conditions that can impede navigation.

Additionally, the smart city concept coupled with the IoT will continue to expand, generating a wealth of data and information that can be used for geospatial analysis through artificial intelligence. The digital twin concept is fertile ground for using AI tools to extract useful information and

Photogrammetric Engineering & Remote Sensing
Vol. 89, No. 6, June 2023, pp. 337-341.
0099-1112/22/337-341

doi: 10.14358/PERS.89.6.337

predict future trends and phenomena. Increasingly, software companies are providing platforms for building and hosting digital twins. Companies like Microsoft, through its Azure digital twin platform, and Bentley, Autodesk, and Esri have developed capabilities to support digital twin development.

Virtual Collaboration Rooms and Mixed Reality: Several technologies that support virtual collaboration and data visualization were spotlighted in 2022. Those platforms generate the need for 3D data while providing a new means of data modeling and interpretation. These include Microsoft Mesh and HoloLens 2; Bentley's mixed reality platform, SYNCHRO XR; and the NVIDIA Omniverse platform. Demand for higher-resolution 3D geospatial data has grown rapidly in the past year. This will continue to fuel multiverses that interface to human factors through augmented and virtual reality, offering new possibilities for visualization, design, and analysis. This mixed reality tech trend will trend upward as more applications of AR and VR are discovered and applied to support multiple industries.

Deep into Miniaturized Sensors: Smartphones continue to branch out geospatially, putting lidar capabilities in the hands of the masses while expanding opportunities for professional surveyors and mappers to conduct geospatial survey on small projects. A sneak preview of smartphones coming out this year indicates that they will include even more advanced lidar systems. This underscores how sensor systems will continue to get smaller, more efficient, and more technologically advanced.

High-Definition Maps for Autonomous Driving: I made a plea last year for the geospatial industry to take the lead on creating and standardizing high-definition maps for a global road network in support of autonomous vehicles. Sadly, a year has passed, and the situation remains unaltered. This precision location data should include lane numbers, freeway exit lanes, pedestrian crosswalks, bridges, overpasses, tunnels, locations of traffic control devices, 3D trajectories for road edges and boundaries, etc., with accuracy to the centimeter level, meter-by-meter road grade, and road superelevation. Addressing this situation continues to be an immense opportunity for our industry and the future of safe autonomous transportation.

Rising Drone Demand: As predicted, uncrewed aircraft system-based lidar took off in 2022 and will continue to rise, providing a healthy offering of new and affordable lidar. In 2021, growth was spurred by the DJI lidar system, Zenmuse L1, which provided high accuracy at a comparably lower cost. Today, while most affordable UAS-based lidar systems are based on Livox laser technology, UAS-based lidar systems based on Hesai technology (or Hesai scanners) are gaining growing interest, having proved to be more robust and better suited for general survey, mapping, and inspection applications. An example of this is the RESEPI XT32 by Inertial Labs, which features a 360-degree field of view and 32 lasers.

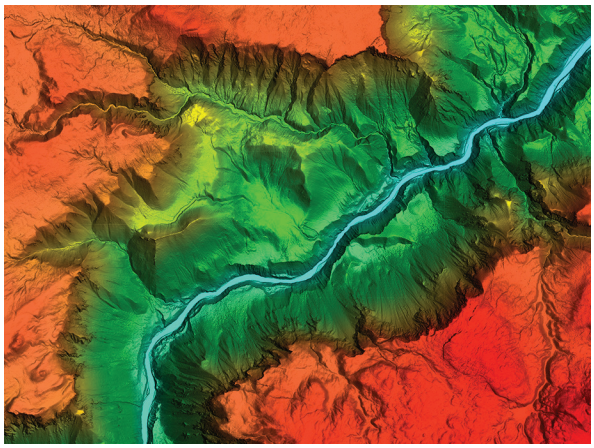

Woolpert collected lidar data of this Wyoming canyon in Yellowstone National Park to create a digital elevation model for the U.S. Geological Survey. *Image courtesy of the United States Geological Survey.

The geospatial industry can advance the future of safe, autonomous transportation by standardizing high-definition maps for a global road network. Photo courtesy of Getty Images.

Lidar continues to be a mover and a shaker for the geospatial industry and will remain so for the foreseeable future. Graphic courtesy of Woolpert

The manufacturer claims the RESEPI XT32 provides 1-centimeter accuracy.

For drones overall, the industry demand is strong, especially for mapping and inspection applications.

Whirl Around the Coastal Regions: Coastal wind energy contracts were highlighted in my article last year as part of a larger effort by the U.S. to transition to cleaner, renewable sources of energy and to reduce reliance on fossil fuels. In 2022 and into 2023, this effort continues to grow, with coastal wind farms approved and constructed along the nation's coastlines.

On a larger scale, the demand for airborne lidar bathymetric data is on the rise and best demonstrated by the Florida Seafloor Mapping Initiative (FSMI), which is being managed by Florida Department of Environmental Protection, as well as a multitude of projects in the Pacific. These projects are aimed at collecting critical foundation data needed for coastal inundation modeling, resilience planning, and engineering projects.

Data Democratization: In the past year we witnessed an explosion in the demand for high-resolution, high-frequency geospatial information from denser point clouds to more crowd-sourced location data. New market entrants are using AI to extract infrastructure features in exquisite detail. The market is hungry for good, raw 3D data to feed these algorithms. With the higher demand for geospatial data, we should see prices fall and higher shelf-life decrease. The quality and availability of publicly available data will also increase.

AI and the Cloud: AI and machine learning both play a significant role in geospatial analysis and mapping. Thanks to private sector investments, cloud data hosting and processing, serverless cloud computing, off-the-shelf and open-source technologies, and streamlined workflows with AI tools all continue to trend upward. I am still hoping that federal and public funding can be used to entice further creativity in this field. Without these investments outside the private sector, the most cutting edge geoanalytics will not be available to the broader market.

Lidar Growth: As you likely have seen from its mention in multiple topics above, lidar continues to be a mover and a shaker for the geospatial industry and will remain so for the foreseeable future. Lidar efficiencies continue to expand across other industries to support robotic applications such as autonomous driving and machine learning.

Bathymetric lidar also has been getting more attention. Leica recently announced the release of its newest deep bathymetric lidar sensor, the Leica HawkEye-5, which reportedly has a 25% increase in performance. Woolpert and the Joint Airborne Lidar Bathymetry Technical Center of Expertise (JALBTCX) announced Bathymetric Unmanned Littoral LiDar for Operational GEOINT (BULLDOG) technologies and sensor. These technologies enable the collection of high-resolution topo-bathy data at a higher altitude, resulting in a broader swath than previously developed lidar systems.

The introduction of these new bathymetric lidar capabilities is timely, as they are being employed to serve the many vital statewide and national coastal mapping initiatives, as noted above with initiatives like FSMI. States are using this federal funding window to collect data essential to everything from asset management to infrastructure planning to disaster response. What is key to these opportunities is that contracting agencies make sure they collect consistent, high-quality data so they can reap the rewards of this funding for years to come. Miniature lidar manufacturing, especially for sensors mounted on drones, is getting a healthy share of the lidar market as more surveying and mapping businesses embrace the technology.

Other noteworthy trends

Here are a few other quick-hitting geospatial trends in technologies and methodologies to watch in 2023:

- Indoor mapping will continue to become more sophisticated, opening the door for improved indoor wayfinding and asset management.
- Location data will be subjected to increasing privacy and security regulations and standards. For the extra layer of security it provides, we may witness increased use of blockchain technology in geospatial data management and sharing.
- With more user-friendly data visualization tools available to all industries, 3D geospatial data will be increasingly used in training, gaming, planning, design, asset management, navigation, and other applications.

>ASPRS Accuracy Standards Update

When we published the ASPRS Positional Accuracy Standards for Digital Geospatial Data Standards in 2014, we knew we would have to modify it based on user experience and feedback. And sure enough, after eight years of fast-changing sensor technologies and evolving applications, it became clear that significant changes needed to be made to the standards to make them more adaptable to today's mapping practices.

One of the most important changes that our revision working group has endorsed is easing the accuracy of field surveying requirements for ground control and checkpoints. As we are producing more accurate products, we have realized that the current accuracy requirement for checkpoints of three times better than the accuracy of the tested product have rendered nearly useless our affordable RTK-GPS

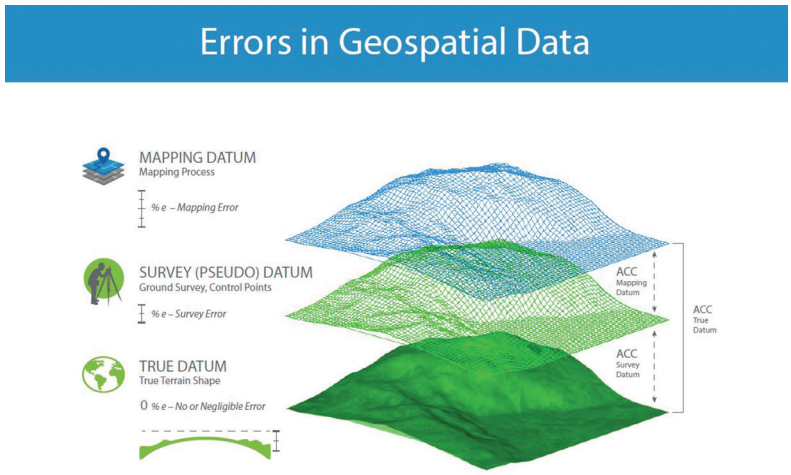

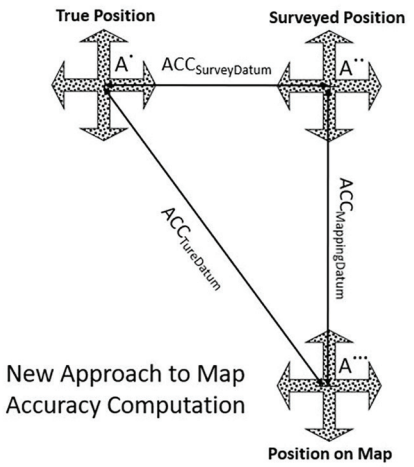

techniques, which are predominately used for surveying. This requirement has forced contracting agencies to specify more expensive surveying techniques, which has proved to be a cost prohibitive for completing these contracts.

Another important change is the addition of five addendums on best practices and guidelines in project notes and data reporting, photogrammetry, lidar, UAS, and field surveying. When we published the first edition in 2014, we designed it to be a modular standard to accommodate additional materials as the industry evolved. Since then, we have witnessed an unprecedented acceleration in geospatial technologies and practices. This growth necessitated guidelines and best practices in multiple aspects of geospatial mapping to help users of the standards navigate these rapidly changing advancements. These addendums were crafted by industry leaders who specialize in these fields.

In addition, an important change is coming regarding the way we evaluate product accuracy. Currently, we ignore the error in survey checkpoints. That practice was acceptable when geospatial mapping product accuracy was low, and the surveying techniques applied did not represent a substantial enough source of error to be considered in computing product accuracy. As we are moving into more accurate products, i.e., in the range of a few centimeters, it has become apparent that the 2cm error embedded in the RTK-GPS survey technique can no longer be ignored. The new method will consider the fit of the product to the checkpoints plus the error of the survey.

The second edition of these standards will be published in the next few months. Keep an eye out for a forthcoming article that highlights the changes and their ramifications which are designed to advance the geospatial industry. Above all else, this will have a long-lasting impact on the geospatial industry.

Woolpert Vice President and Chief Scientist Qassim Abdullah, Ph.D., PLS, CP, has more than 40 years of combined industrial, R&D, and academic experience in analytical photogrammetry, digital remote sensing, and civil and surveying engineering. When he's not presenting at geospatial conferences around the world, Abdullah teaches photogrammetry and remote sensing courses at the University of Maryland and Penn State, authors a monthly column for the ASPRS journal *PE&RS*, and mentors R&D activities within Woolpert.

This article is running in running in *PE&RS* Journal and *Lidar Magazine*.

The layman's perspective on technical theory and practical applications of mapping and GIS

MAPPING MATTERS

YOUR QUESTIONS ANSWERED

by Qassim Abdullah, Ph.D., PLS, CP
Woolpert Vice President and Chief Scientist

- **Have you ever wondered about what can and can't be achieved with geospatial technologies and processes?**
- **Would you like to understand the geospatial industry in layman's terms?**
- **Have you been intimidated by formulas or equations in scientific journal articles and published reports?**
- **Do you have a challenging technical question that no one you know can answer?**

If you answered "YES" to any of these questions, then you need to read Dr. Qassim Abdullah's column, Mapping Matters.

In it, he answers all geospatial questions—no matter how challenging—and offers accessible solutions.

Send your questions to Mapping_Matters@asprs.org

To browse previous articles of Mapping Matters, visit http://www.asprs.org/Mapping-Matters.html

"Your mapping matters publications have helped us a lot in refining our knowledge on the world of Photogrammetry. I always admire what you are doing to the science of Photogrammetry. Thank You Very much! the world wants more of enthusiast scientists like you."

"I read through your comments and calculations twice. It is very clear understandable. I am Honored there are experienced professionals like you, willing to help fellow members and promote knowledge in the Geo-Spatial Sciences."

YOUR COMPANION TO SUCCESS

GIS Tips & Tricks

Srinu Ratnala, Andrew Peters, GISP, and Al Karlin, Ph.D. CMS-L, GISP

Easy Contours in Global Mapper

While many GIS Tips & Tricks columns focus on the Esri-based ArcGIS and ArcGIS Pro software packages, there are many other software packages that offer similar GIS-based analytical tools. In this column we will explore using Global Mapper™ to quickly produce contour lines from a Digital Elevation Model. This workflow is relatively straightforward; it uses a basic Global Mapper license, no extensions required, and only requires a bare earth Digital Elevation Model (DEM) which can easily be downloaded from the USGS National Map (https://apps.nationalmap.gov/downloader/) or the NOAA Digital Coast (https://coast.noaa.gov/dataviewer/#/), both of which have been discussed in other GIS Tips & Tricks columns. Global Mapper™ provides the end-user with multiple options for constructing contours, including custom intervals, major and minor contours, and smoothing algorithms accessed directly from a simple dialog box system.

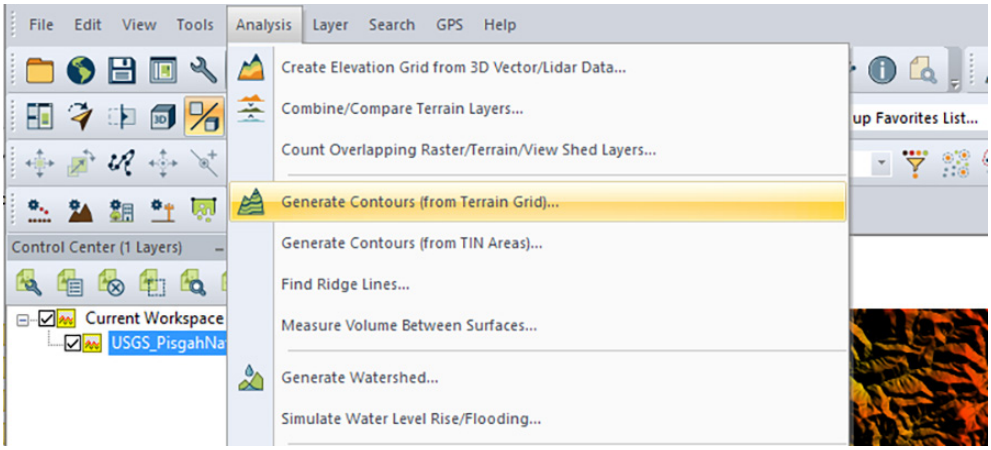

Figure 1. Starting the Generate Contours Dialog Box from the Analysis Tab in Global Mapper™.

The Basic Workflow

Step 1 — Load a bare earth DEM into Global Mapper,
Step 2 — Select the "Analysis" Tab on the Ribbon,
Step 3 — Select the "Generate Contours (from Terrain Grid) tool on the dropdown,
Step 4 — Update/Fill-in a few parameters on a dialog box,
Step 5 — [optional] Export the generated contours to a permanent file of your choice.

Example Workflow

Note: For this example, we downloaded a 1-meter DEM for the Pisgah National Forest area in North Carolina from the U.S. National Map. The DEM was referenced to UTM Zone 17N/NAD83 in meters (EPSG:26917). The file format is a 32-bit Floating Point GeoTIFF.

Step 1 — Load the bare earth DEM.
Step 2 — From the menu bar, click the Analysis Tab and select the "Generate Contours (from Terrain Grid) tool as in Figure 1).
Step 3 — Fill in the Contour Generation Options Dialog. Notice that there are four Tabs across the top of this Dialog.

The Contour Generation Options Tab (Figure 2) is used to specify the contour interval and other optional characteristics of the lines. In this case, we will generate 10-meter contours with Minor Contours every 10-meters and Major Contours every 100 meters in this very rugged terrain. Notice that Global Mapper™ reports the elevation ranges in the DEM (345.9 to 861 meters in this example) and there are options for resampling the DEM, smoothing the contour lines, and removing closed (small circular looping) contour lines on this Tab.

TIP #1

The "Discard Closed Contour Lines Shorter than" will omit closed (looping) contour lines of a length less than the specified measure. This is important if you want to remove small circular contours that can be prevalent in lidar-derived DEMs. Depending on your use-case, this value can range to hundreds of meters and may require empirical testing.

Photogrammetric Engineering & Remote Sensing
Vol. 89, No. 6, June 2023, pp. 343-346.
0099-1112/22/343-346

doi: 10.14358/PERS.89.6.343

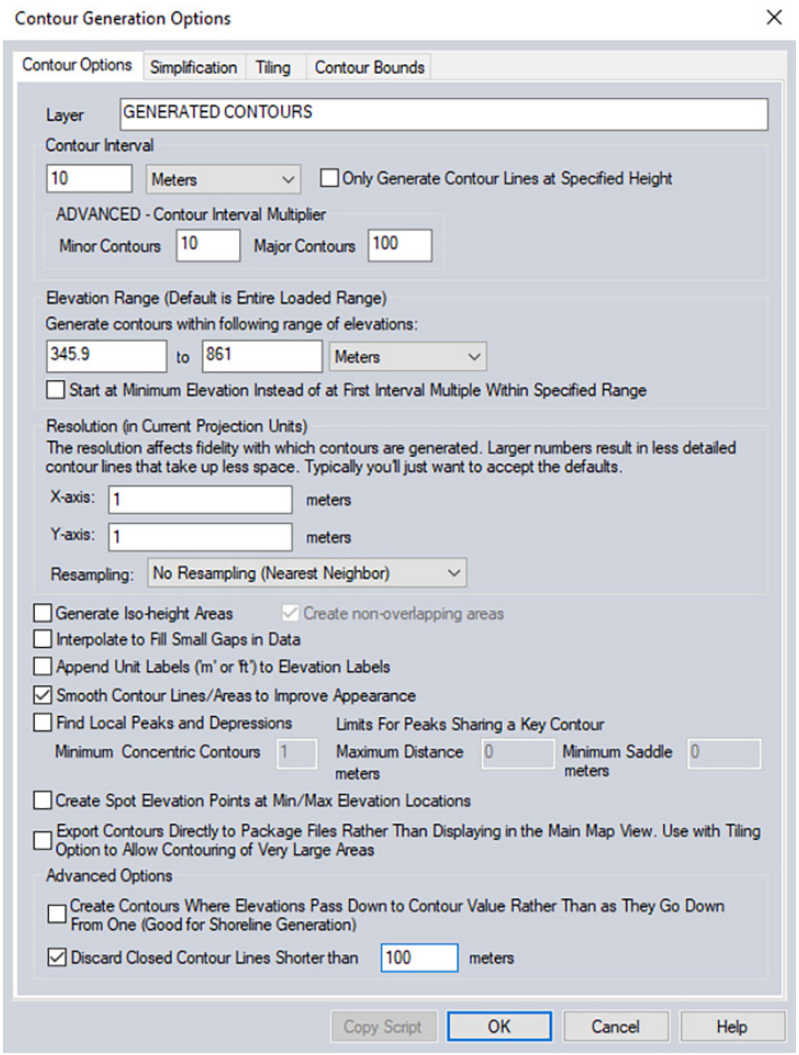

Figure 2. The Global Mapper Contour Options Tab used when generating contours.

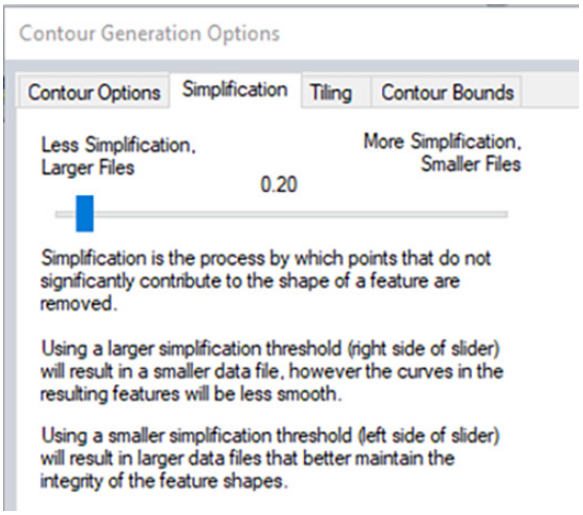

Figure 3. The Simplification Tab slider is used to control the number of nodes per contour line; this also influences the file.

TIP #2

The Simplification Tab (Figure 3) provides a slider to adjust the number of non-essential points along a contour line. The more points maintained to define the contour's shape, the larger the size of the resulting file, but the better the shape of the lines. The default value is 0.10, and of course, "never accept the defaults", we recommend a 0.20 as a starting setting and increasing the value if the file size is too large or decreasing this value if the contour lines are too jagged for your use-case.

Zooming in to a smaller area in this DEM shows the 100-meter Major and 10-meter Minor contours symbolized in different line weights (Figure 4.)

TIP #3

The Pisgah National Forest DEM used in this example was 356 MB in size (10,000 x 10,000 cells) and processed the 10-meter contours in a little over one minute and four seconds. When processing very large DEM mosaics, try resampling the DEM with one of the optional methods (See Figure 2) to decrease processing time.

Step 4A — Save your Global Mapper™ Workspace to make the GENERAGED CONTOURS permanent for Global Mapper™, and/or

Step 4B — Export the contours to another GIS Format for use in ArcGIS, GRASS, and/or other mapping packages.

Here are the steps to Export the GENERATED CONTOURS to an Esri shapefile.

Step 5 — Right-click on the GENERATED CONTOUR layer in the Control Center, scroll to the Layer bar and slide to the right to open the options, and select EXPORT – Export Layer(s) to New File (Figure 5)

Step 6 — Select the Layers to Export from the Dialog Box (Figure 6)

Step 7 — Use the Dropdown selections (Figure 7) and scroll down the list to find the file format to export. In this case "Shapefile" is far down the alphabetical listing.

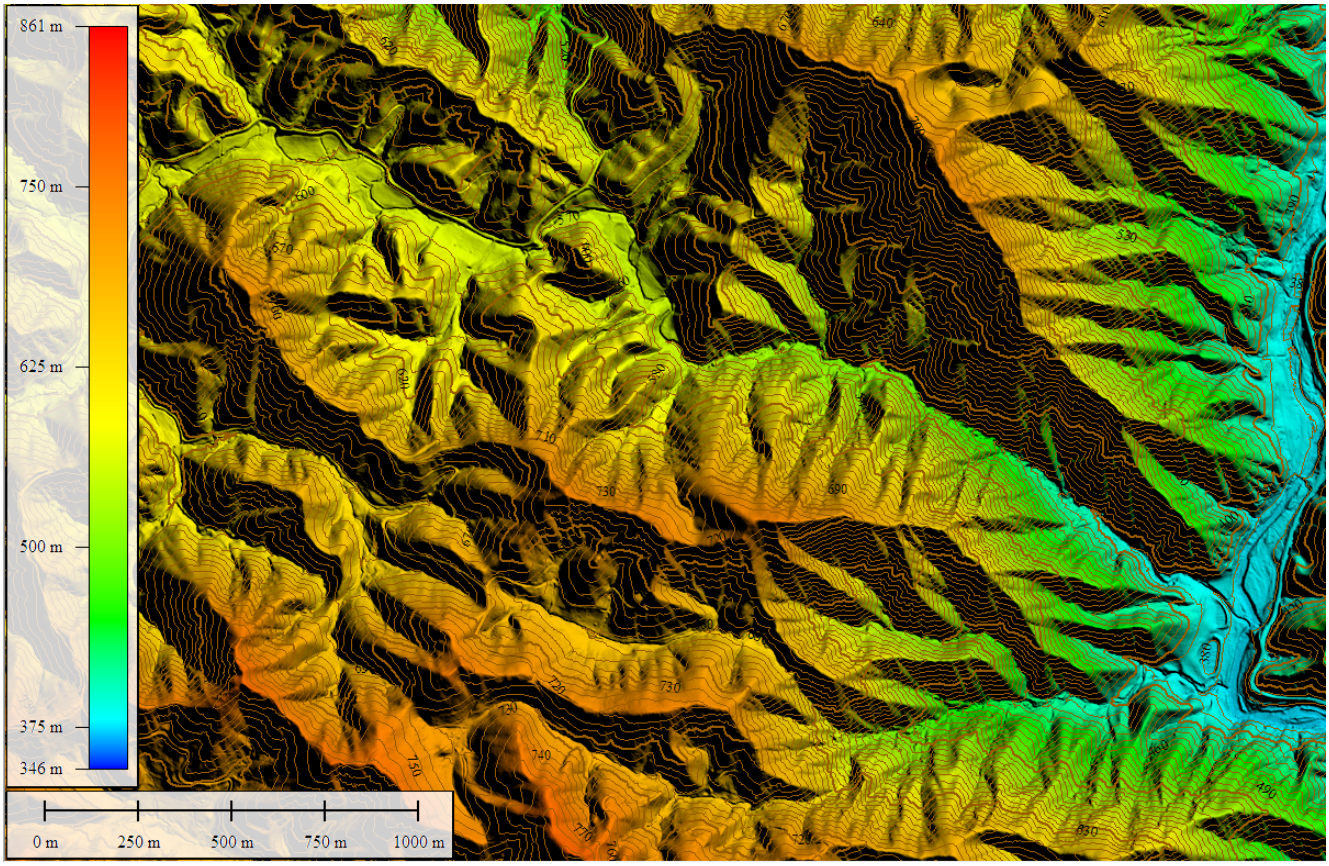

Figure 4. 10-meter Minor and 100-meter Major contours Global Mapper™ generated from the DEM.

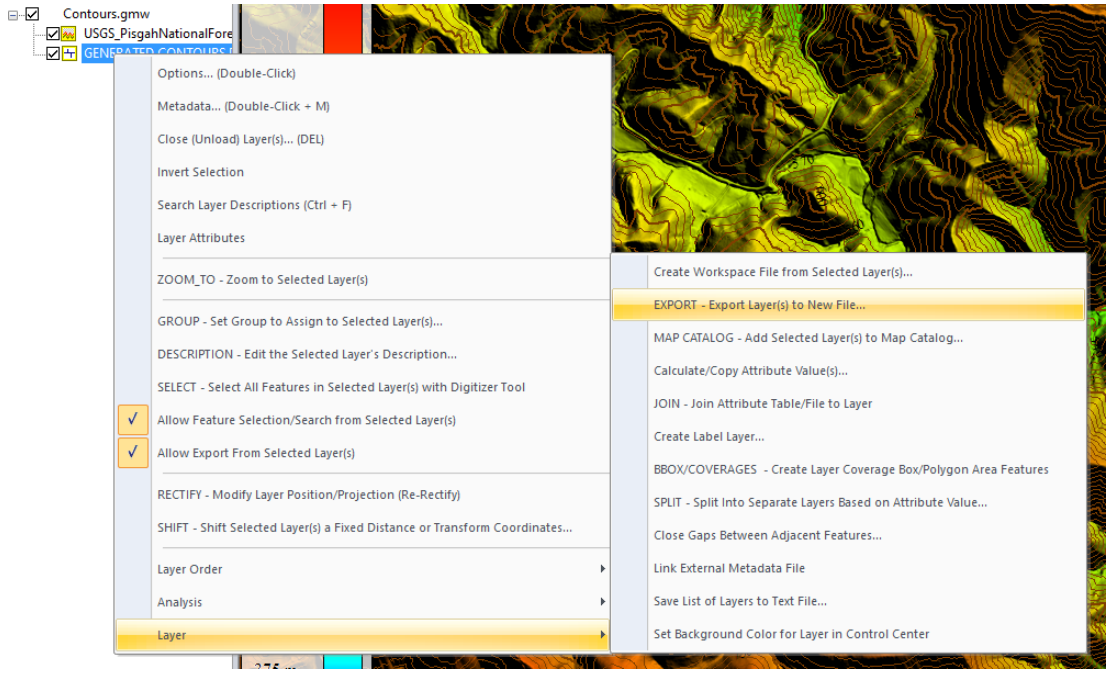

Figure 5. Starting the Global Mapper™ EXPORT dialog to export the GENERATED CONTOURS line file

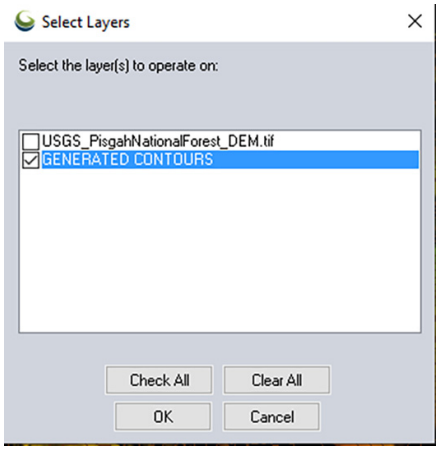

Figure 6. The Global Mapper™ "Select Layers" dialog box used to select the layer to export.

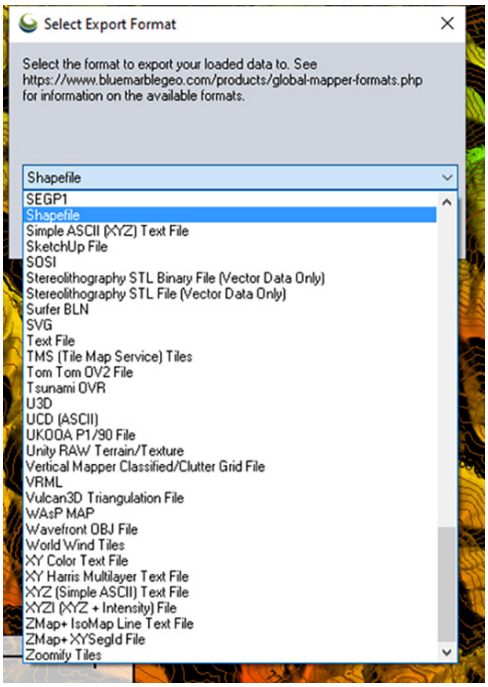

Figure 7. The Global Mapper™ export file format selection menu; the available formats are alphabetical.

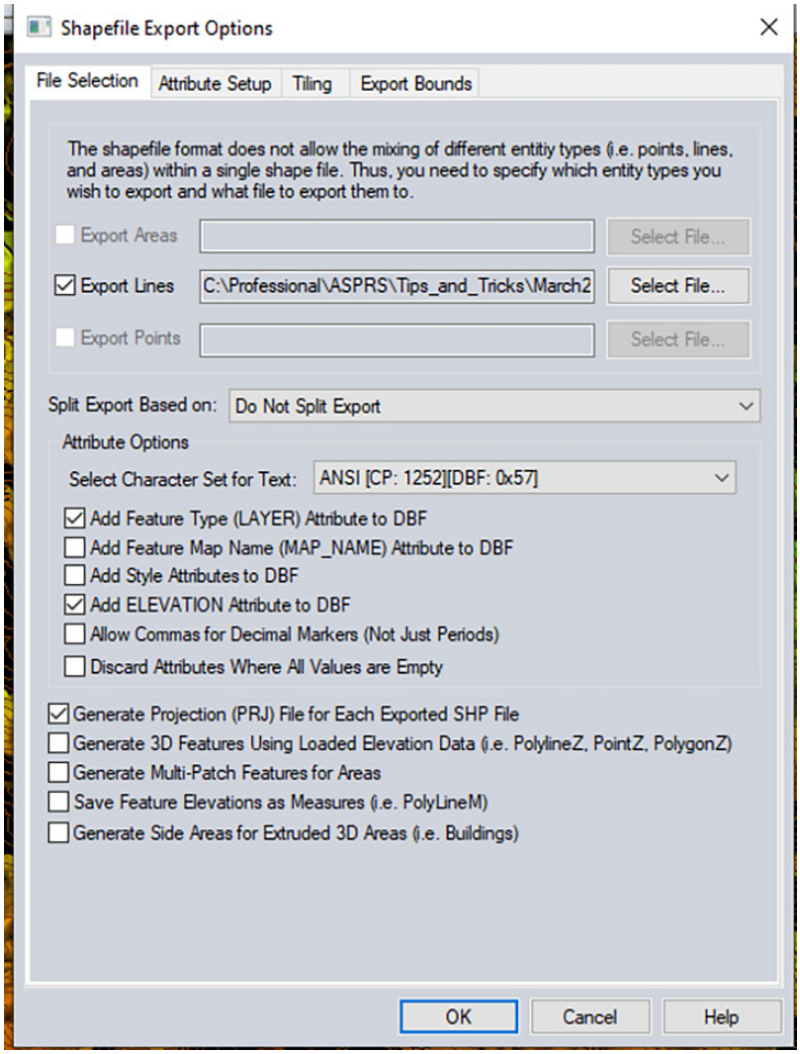

Figure 8. The Global Mapper™ Export Shapefile Options dialog box showing four tabs (across the top) and multiple options screens.

Tip #4

Key-in the letter "S" on the keyboard by selecting the Drop-down list for quick navigation.

Step 8 — On the Shapefile Export Options dialog box (Figure 8), when you check the "Export Lines" box, a Windows file browser will appear; navigate to a writable directory and specify a file name (Global Mapper™ will append .shp to your filename. Be careful to check the "Generate Projection (PRJ) for each Exported SHP File". There are several more options and additional Tabs with other parameters and press "OK" to export/write the file.

Global Mapper™ provides an efficient, extremely flexible option for constructing contours from a DEM. It really is that easy.

Send your questions, comments, and tips to GISTT@ASPRS.org.

Srinu Ratnala *is a project manager with D*ewberry's Geo*spatial and Technology Services group in Fairfax, VA. Sri's areas of expertise include analytics and visualization solutions. He has been working with lidar and other 3D-related projects.*

Andrew Peters, GISP *is a senior associate and assistant department manager with Dewberry's Geospatial and Technologies Services group in Fairfax, VA. Andrew specializes in assessing the accuracy of lidar information by comparing raw lidar data with ground survey data, generating bare-earth models, and using models for contour line creation.*

Al Karlin, Ph.D., CMS-L, GISP *is a senior geospatial scientist with Dewberry's Geospatial and Technology Services group in Tampa, FL. Al works with all aspects of lidar, remote sensing, photogrammetry, and GIS-related projects. Al also teaches Mapmaking for the Social Sciences at the University of Tampa.*

GEORGE E. BROWN, JR. CONGRESSIONAL HONOR AWARD

The 2021 award was presented to Congresswoman Betty McCollum on March 16th, 2023 during the "State of Our River - Mississippi River Dialogue" Meeting.

This award was established in honor of Congressman George E. Brown, Jr. and the contributions he made to advance the benefits of remote sensing imagery and geospatial information to the profession and society. The award is given periodically to recognize members of the U.S. Congress whose leadership and personal efforts have advanced the science, engineering, application, education, and commerce of remote sensing imaging and geospatial information systems.

On the left, Congresswoman Betty McCollum listens to Brian Huberty, ASPRS Western Great Lakes Region give a short history about the ASPRS Brown Award. (Photo Credit: Emmet Rice)

Thanks to COVID, it took additional time for ASPRS to award, in person, the 2021 George E. Brown, Jr. Congressional Honor Award to Congresswoman Betty McCollum (MN 4th District) for her support as a member of the House Appropriations Committee. She currently serves as the Chair of the Defense Subcommittee, the Vice Chair of the Interior-Environment Subcommittee, and as a member of the Agriculture and Rural Development Subcommittee. As one can imagine, she is quite busy with her roles in Congress. In these roles, she has continued to ensure funding for civil and defense remote sensing and geospatial information systems and programs.

Her 'behind the scenes' work includes multiple civil, defense and international collaborations to push global and regional remote sensing science mapping applications. The largest global example is an on-going collaboration between the National Science Foundation (NSF), National Geospatial-Intelligence Agency (NGA), NASA, and the Universities of Minnesota, Illinois, Texas,

STAND OUT FROM THE REST

EARN ASPRS CERTIFICATION

ASPRS congratulates these recently Certified and Re-certified individuals:

RECERTIFIED PHOTOGRAMMETRIST

Wallace Scott Dunham, Certification #R1400CP
Effective April 19, 2024, expires April 19, 2029

Douglas Timothy, Certification #R1502CP
Effective July 8, 2021, expires July 8, 2026

Brian Stefancik, Certification #R1545CP
Effective March 7, 2023, expires March 7, 2028

Sally Gehr, Certification #R1547CP
Effective April 7, 2023, expires April 7, 2028

John Lesko, Certification #R1014CP
Effective January 13, 2023, expires January 13, 2028

RECERTIFIED MAPPING SCIENTIST LIDAR

Wallace Scott Dunham, Certification #R030L
Effective August 15, 2023, expires August 15, 2028

ASPRS Certification validates your professional practice and experience. It differentiates you from others in the profession. For more information on the ASPRS Certification program: contact **certification@asprs.org,** visit **https://www.asprs.org/general/asprs-certification-program.html.**

asprs THE IMAGING & GEOSPATIAL INFORMATION SOCIETY

NEW ASPRS MEMBERS

ASPRS would like to welcome the following new members!

Surendran Amerendran, Ph.D.
Logan Richard Burdwood
Elizabeth Josephine Bushnell
Temitope Hauwa Dauda
Sanduni Disanayaka Mudiyanselage
Elizabeth Elkins, Student
Yuemeng Gao
Christopher Guagliardo
Kim Hansen
Brooklyn Heron
Luke Hull
Brianna Lee Larkin
Breann Larson
Afolarin Lawal
Julia Lenhardt
Priscilla Mawuena Loh
Benjamin Long
Timothy McEwan
Lalitha Muthu Subramanian
Riley O'Donnell
Alicia Peduzzi
Anand Raju
Liz Richardson
Carol Samuelson
Danielle Marie Schaffeld
Ethan Schreuder
Kevin Simans
Brian Sumner
David Troiani
Mike Venegas
Miles H. Wagner
Steven Joseph Weber
Mohamad Yassin
Sean G. Young, Ph.D.
Feng Yu, Ph.D.

FOR MORE INFORMATION ON ASPRS MEMBERSHIP, VISIT
HTTP://WWW.ASPRS.ORG/JOIN-NOW

ASPRS WORKSHOP SERIES

It's not too late to earn Professional Development Hours

Miss an ASPRS Workshop or GeoByte? Don't worry! Many ASPRS events are available through our online learning catalog.

https://asprs.prolearn.io/catalog

Image Priscilla Du Preez on Unsplash.

(L_R) Congresswoman Betty McCollum and Brian Huberty, ASPRS Western Great Lakes Region. (Photo Credit: Emmet Rice)

Washington, and the Ohio State University. This group, led by the University of Minnesota, Polar Geospatial Center (PGC), has developed techniques for producing EarthDEM[1] - a global scale, two-meter, surface topographic dataset using high resolution, time-dependent, MAXAR satellite optical imagery with open-source software and U.S. Government-funded, high-performance computing (Blue Waters) to produce a large volume of high-quality, publicly distributed, geospatial data.

Another regional example spun out of a U.S. Fish & Wildlife Service-Great Lake Restoration Initiative project mapping the Great Lakes Basin surface vegetation canopies. This project produced wetland maps with Canada by dovetailing the EarthDEM work by PGC. Again, thanks to NGA, and monthly Radarsat 2 images, over a dozen sites across the Great Lakes were able to produce wetland inundation maps for a five-year period. This work was done by the University of Minnesota, PGC and the Remote Sensing and Geospatial Analysis Laboratory; Michigan Tech University, Michigan Tech Research Institute; SharedGeo, the Minnesota Department of Natural Resources, Resource Assessment; Natural Resources Canada, Canada Centre for Remote Sensing; Environment & Climate Change Canada, Geomatics Research. This project led to the creation of the binational Great Lakes Alliance for Remote Sensing.[2]

The award was presented on March 16th, 2023 during the "State of Our River - Mississippi River Dialogue" meeting Congresswoman McCollum led at the Science Museum of Minnesota in St. Paul, Minnesota. On the award, a digital surface model of her district was created from a 2011 Fugro-Horizons lidar project under contract by the Minnesota Department of Natural Resources. The map was created by Jim Klassen, Sharedgeo who happens to be one of her constituents.

Author

Brian Huberty, Remote Sensing Advisor, Sharedgeo.org.

[1] https://www.pgc.umn.edu/data/earthdem/

[2] https://glars.org

Landsat's Enduring Legacy

Pioneering Global Land Observations from Space

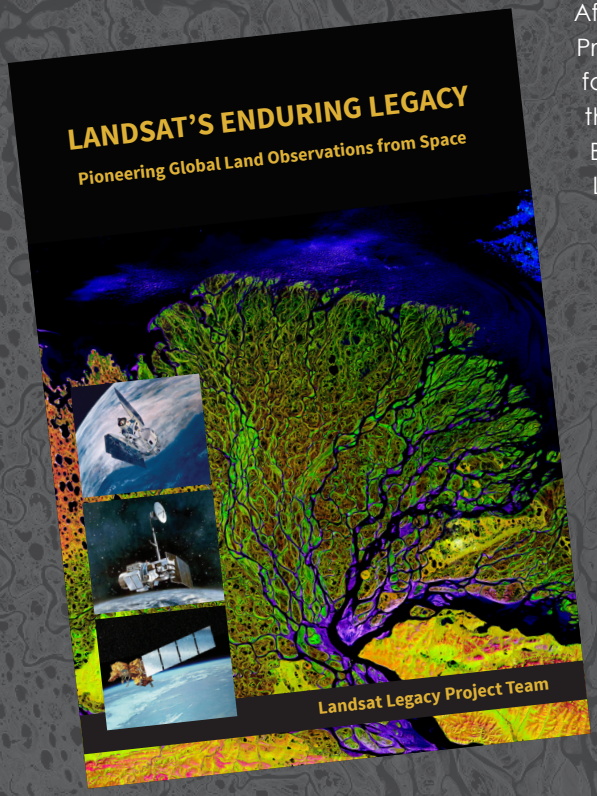

After more than 15 years of research and writing, the Landsat Legacy Project Team published, in collaboration with the American Society for Photogrammetry and Remote Sensing (ASPRS), a seminal work on the nearly half-century of monitoring the Earth's lands with Landsat. Born of technologies that evolved from the Second World War, Landsat not only pioneered global land monitoring but in the process drove innovation in digital imaging technologies and encouraged development of global imagery archives. Access to this imagery led to early breakthroughs in natural resources assessments, particularly for agriculture, forestry, and geology. The technical Landsat remote sensing revolution was not simple or straightforward. Early conflicts between civilian and defense satellite remote sensing users gave way to disagreements over whether the Landsat system should be a public service or a private enterprise. The failed attempts to privatize Landsat nearly led to its demise. Only the combined engagement of civilian and defense organizations ultimately saved this pioneer satellite land monitoring program. With the emergence of 21st century Earth system science research, the full value of the Landsat concept and its continuous 45-year global archive has been recognized and embraced. Discussion of Landsat's future continues but its heritage will not be forgotten.

The pioneering satellite system's vital history is captured in this notable volume on Landsat's Enduring Legacy.

Landsat Legacy Project Team
Samuel N. Goward
Darrel L. Williams
Terry Arvidson
Laura E. P. Rocchio
James R. Irons
Carol A. Russell
Shaida S. Johnston

Landsat's Enduring Legacy

Hardback. 2017, ISBN 1-57083-101-7

Member/Non-member	$48*
Student Member	$36*

* Plus shipping

Order online at

www.asprs.org/landsat

asprs THE IMAGING & GEOSPATIAL INFORMATION SOCIETY

Call for *PE&RS* Special Issue Submissions

Ushering a New Era of Hyperspectral Remote Sensing to Advance Remote Sensing Science in the Twenty-first Century

Great advances are taking place in remote sensing with the advent of new generation of hyperspectral sensors. These include data from, already in orbit sensors such as: 1. Germany's Deutsches Zentrum fur Luftund Raumfahrt (DLR's) Earth Sensing Imaging Spectrometer (DESIS) sensor onboard the International Space Station (ISS), 2. Italian Space Agency's (ASI's) PRISMA (Hyperspectral Precursor of the Application Mission), and 3. Germany's DLR's Environmental Mapping and Analysis Program (EnMAP). Further, Planet Labs PBC recently announced the launch of two hyperspectral sensors called Tanager in 2023. NASA is planning for the hyperspectral sensor Surface Biology and Geology (SBG) to be launched in the coming years. Further, we already have over 70,000 hyperspectral images of the world acquired from NASA's Earth Observing-1 (EO-1) Hyperion that are freely available to anyone from the U.S. Geological Survey's data archives.

These suites of sensors acquire data in 200 plus hyperspectral narrowbands (HNBs) in 2.55 to 12 nm bandwidth, either in 400-1000 or 400-2500 nm spectral range with SBG also acquiring data in the thermal range. In addition, Landsat-NEXT is planning a constellation of 3 satellites each carrying 26 bands in the 400-12,000 nm wavelength range. HNBs provide data as "spectral signatures" in stark contrast to "a few data points along the spectrum" provided by multispectral broadbands (MBBs) such as the Landsat satellite series.

The goal of this special issue is to seek scientific papers that perform research utilizing data from these new generation hyperspectral narrowband (HNB) sensors for a wide array of science applications and compare them with the performance of the multispectral broadband (MBB) sensors such as Landsat, Sentinels, MODIS, IRS, SPOT, and a host of others.

Papers on the following topics are of particular interest:

1. Methods and techniques of understanding, processing, and computing hyperspectral data with specific emphasis on machine learning, deep learning, artificial intelligence (ML/DL/AI), and cloud computing.
2. Issues of hyperspectral data volumes, data redundancy, and overcoming Hughes' phenomenon.
3. Building hyperspectral libraries for purposes of creating reference training, testing, and validation data.
4. Utilizing time-series multispectral data and hyperspectral data over many years to build data cubes and apply advanced computational methods of ML/DL/AI methods and approaches on the cloud.
5. Discussions of hyperspectral data analysis techniques like full spectral analysis versus optimal band analysis.
6. Developing hyperspectral vegetation indices (HVIs) for targeted applications to model and map plant biophysical (e.g., Yield, biomass, leaf area index), biochemical (e.g., Nitrogen, anthocyanins, carotenoids), plant health/stress, and plant structural quantities.
7. Classification of complex vegetation and crop types/species using HNBs and HVIs and comparing them with the performance of multispectral broadband data.

All submissions will be peer-reviewed in line with *PE&RS* policy. Because of page limits, not all submissions recommended for acceptance by the review panel may be included in the special issue. Under this circumstance, the guest editors will select the most relevant papers for inclusion in the special issue. Authors must prepare manuscripts according to the *PE&RS* Instructions to Authors, published in each issue of *PE&RS* and also available on the ASPRS website, https://www.asprs.org/asprs-publications/pers/manuscript-submission.

Special Issue Editors

Dr. Prasad S. Thenkabail, pthenkabail@usgs.gov, thenkabail@gmail.com
Senior Scientist (ST), USGS, Flagstaff, Arizona

Dr. Itiya Aneece, ianeece@usgs.gov
USGS, Flagstaff, Arizona

Dr. Pardhasaradhi Teluguntla, pteluguntla@usgs.gov
USGS, Flagstaff, Arizona

Important Dates

Manuscripts Due — December 15, 2023

Final Papers Due — May 1, 2024

Tentative Publication Date — 2024

Please submit your manuscript — www.editorialmanager.com/asprs-pers/ select "Hyperspectral Remote Sensing"

Call for *PE&RS* Special Issue Submissions

Special Issue on the Scholarship and Impacts of Professor Nina S. N. Lam

Expected Date for Publication: 2024

Special Issue Editors
Michael Leitner (mleitne@lsu.edu)
Jane Read (jaread@syr.edu)

This special issue recognizes Professor Nina S. N. Lam's ~45 years of contribution to Geographic Information and Environmental Sciences. From her first publications on spatial/areal interpolation methods in the early 1980s, she evolved into an internationally recognized scholar known for her leadership in diverse research areas, from scale, resolution, and fractals to environmental health, disaster resilience, and sustainability. Professor Lam, who currently holds the E. L. Abraham Distinguished Professor of Louisiana Environmental Studies title, has been the recipient of many honors and awards, including the inaugural Carolyn Merry Mentoring Award from the UCGIS (2016), being named a Fellow of both the AAG (2020) and the UCGIS (2016), as well as being named a LSU Rainmaker, recognizing one of the top 100 research and creative faculty (2008), and the LSU Distinguished Faculty Award (2006). Her legacy in research, teaching, and service continues through her many students, who are actively contributing to Geographic Information Science (GISc) in academia, government, and the private sector, including the second co-guest editor of this special issue.

This special issue celebrates the outstanding scholarly work of Professor Lam. We invite original contributions from her students, collaborators, and anyone impacted and influenced by her work. Topics covered should be broadly situated within remote sensing, disaster/environmental sciences, sustainability, environmental health, and GISc, including but not limited to subjects related to her research and impact. Please contact special issue editors for questions and suggestions.

Interested authors should send a manuscript title and short abstract (about 250 words, including the authors' names and affiliations) to the special issue editors (mleitne@lsu.edu; jaread@syr.edu) by July 15, 2023 (see complete publication timeline below).

Manuscript length should be around 5,000-6,000 words. All submissions will be subject to standard *PE&RS* peer review processes. See Instructions for authors (https://www.asprs.org/asprs-publications/pers/pers-instructions-for-authors-submitting-a-manuscript-for-peer-review). All submissions should be made online at the Photogrammetric Engineering and Remote Sensing Manuscript Central site (https://www.editorialmanager.com/asprs-pers/). Authors must select "Special Issue" when they reach the "Article Type" step in the submission process and identify the "Scholarship and Impacts of Professor Nina S. N. Lam Special Issue" in their cover letter. New users should first create an account. Once logged on to the site, submissions should be made via the Author Dashboard. Online user guides and access to a help desk are available on this website.

Timeline for publication of *PE&RS* Special Issue

Manuscript Proposal Deadline (Title and Abstract)	July 15, 2023
Submission Deadline	January 31, 2024
Information about Acceptance	On a rolling basis
Submission of Revised Manuscript Deadline	June 30, 2024
Publication in *PE&RS*	2024

3D Scene Modeling Method and Feasibility Analysis of River Water-Land Integration

Xiaoguang Ruan, Fanghao Yang, Meijing Guo, and Chao Zou

Abstract

Aiming at the problem of rapid construction of a river three-dimensional 3D scene, this article integrates remote sensing, 3D modeling, and CityEngine technology to construct a 3D scene model reconstruction method of river water-land integration. The method includes intelligent extraction of underwater topography, refined modeling of hydraulic structures, and construction of a water-land integrated real scene model. Based on this method, the high-fidelity land-underwater seamless digital terrain and the water-land 3D real scene models can be formed. Through experiments, the feasibility and limitations of this method are verified. It can effectively extract the shallow underwater terrain of inland rivers, and the overall accuracy of the study area is less than 2 m. The performance of the seamless fusion 3D terrain is better than the public digital elevation model data set. In the inland basin of Class I to II water quality, it can meet the needs of intelligent perception of a river- and lake-integrated 3D scene model.

Introduction

The progress of surveying and mapping, remote sensing, and GIS technology makes the digital twin of water conservancy possible. On the whole, the lack of intelligent perception ability of river, lake, and reservoir management is still a problem. There are insufficient emergency and normalized monitoring methods for the whole life cycle of water conservancy project planning and construction and operation and a lack of point, line, and surface collaborative perception ability. It cannot effectively support the modernization and development needs of water governance. The integrated production method of high-fidelity land-underwater seamless digital terrain and the water-land 3D real scene models is one of the most critical technical bottlenecks.

Underwater Terrain Extraction Method

Shipborne sounder and Global Navigation Satellite System (GNSS) RTK are widely used to obtain underwater depth and position information. A single measurement has more or fewer limitations, such as limited measurement area and low efficiency (Collin *et al.* 2018a). Fortunately, medium- and high-resolution multispectral satellite images are increasingly used to to observe underwater topography, geomorphology, and sediment types (Tang *et al.* 2003; Duan *et al.* 2016). Theoretical, semi-empirical, and empirical models are often used in satellite-derived bathymetry (SDB) (Duan *et al.* 2016; Collin *et al.* 2018b, 2018b; Ma *et al.* 2020). The theoretical model is based on many radiative transfer parameters, which is difficult to obtain in the field and is susceptible to environmental conditions, resulting in low terrain accuracy (Collin *et al.* 2018a; Ma *et al.* 2020). Semi-empirical models use single or multiple bands to fit water depth by combining radiation attenuation and analytical regression (Gholamalifard *et al.* 2013). Among them, the accuracy of Lyzenga polynomial model is obviously better than that other models (Lyzenga 1981). The empirical model uses prior knowledge to fit the statistical relationship between water depth and radiation intensity (Collin *et al.* 2017). *Sentinel-2* has the advantages of both spatial resolution and revisit period, which is suitable as a data source for SDB (Hedley *et al.* 2018; Taganos *et al.* 2018). However, the lack of measured data in river basins is still a problem. NASA launched *ICESat-2* single-photon lidar satellites in 2018. After data processing, the *ICESat-2* Advanced Topographic Laser Altimeter System (ATLAS) can be used as reference data for shallow underwater water depth extraction based on active and passive remote sensing fusion (Parrish *et al.* 2019). Thanks to a more sensitive photon counting detector and green light beams capable of penetrating water columns, *ICESat-2* ATLAS is capable of detecting the seabed up to 40 m deep in areas with excellent water quality (Parrish *et al.* 2019; Albright and Glennie 2020). The single-photon lidar satellite signal is seriously attenuated after being affected by sunlight, clouds, and water bodies (Leigh *et al.* 2014). Therefore, *ICESat-2* spaceborne photon point cloud denoising and extraction are necessary.

3D Terrain Fusion Method of Land-Water Integration

The problem of data void filling in the land-water transition zone is the key to digital terrain model fusion. In addition to commonly used spatial interpolation methods such as kriging, spline, and inverse distance weighting, which can be used for void filling, the delta surface fill method can obtain better results (Grohman *et al.* 2006; Robinson *et al.* 2014). Before void filling, the difference between digital elevation models (DEM) and auxiliary data needs to be solved. These differences can occur in horizontal and vertical data, spatial resolution, production errors, first-order or second-order trends, and spatial distribution of errors (Okolie and Smit 2022). After data fusion, terrain smoothing is also performed, such as adaptive smoothing (Yue *et al.* 2017; Ruan *et al.* 2020), low-pass filtering, or high-pass filtering, to remove terrain artifacts (Robinson *et al.* 2014; Pham *et al.* 2018). The global open DEM data sets (such as SRTM, ASTER, and AW3D) have been growing steadily, with a resolution better than 30 m, which can be used as supplementary data for terrain data fusion (Okolie and Smit 2022).

In the aspect of 3D scene modeling, using remote sensing images, CAD drawings, field photos, and other data, based on 3D Max, Revit, Blender, and other technologies for manual modeling, is a structured modeling method. Its disadvantage is low efficiency; the advantage is the detailed expression of complex models, and the model and its accessories are independent of each other (Du *et al.* 2019). The 3D scene modeling method based on lidar and oblique photogrammetry can collect multi-view image data at a low cost, which is highly automated and realistic, but the model is not fine enough (Zhou *et al.* 2016; Zhang *et al.* 2018). Therefore, it is necessary to integrate a variety of 3D modeling methods and integrate multi-source heterogeneous 3D models to realize the complementary advantages of 3D real terrain and individual models (Badwi *et al.* 2022), which is a technical problem faced by the construction of land and water 3D real scene (Ruan *et*

Ruan Xiaoguang*, Yang Fanghao, Guo Meijing, and Zou Chao are with Zhejiang University of Water Resources and Electric Power, Hangzhou 310018, China.

Xiaoguang RUAN: ruanxg@zjweu.edu.cn; Fanghao YANG: 2609195732@qq.com; Meijing GUO: gmjing1109@outlook.com; Chao ZOU: zc885370303@outlook.com

**Corresponding author*

Contributed by Prasad S. Thenkabail, November 14, 2022 (sent for review December 28, 2022; reviewed by Murali Krishna Gumma, Pardhasaradhi Teluguntla).

Photogrammetric Engineering & Remote Sensing
Vol. 89, No. 6, June 2023, pp. 353–359.
0099-1112/22/353–359

doi: 10.14358/PERS.22-00127R2

al. 2022). The computer-generated architecture (CGA) grammar is a shape grammar rule, which contains a series of rules that determine how the model is generated (Kim and Wilson 2015; Badwi *et al.* 2022) and is also known as a parametric modeling method. It can generate building models with high visual quality and geometric details, which are suitable for the construction of multiple shapes. Through the 3D model library composed of CGA rules, the geometric attributes and texture attributes of the building can be set according to the actual needs of the later stage so as to realize fast, automatic, and batch 3D modeling. Based on the CGA rule modeling method of CityEngine and supplemented by the third-party building information modeling (BIM) technology (3D Max, Revit, and Blender), it is feasible to realize the complementary advantages of 3D real scene terrain and individual models.

In this article, the 3D scene modeling method of river water-land integration was proposed. The inland basin high-fidelity land-underwater seamless digital terrain and the water-land integration 3D real scene models were formed, and the feasibility analysis was made. The details are as follows.

Data and Methodology

This article integrates remote sensing, 3D modeling, and CityEngine technology to construct a 3D scene model reconstruction method of river water-land integration. The method includes intelligent extraction of underwater topography, refined modeling of hydraulic structures, and construction of a water-land integrated real scene model.

The overall technical process is shown in Figure 1.

Land 3D Terrain Modeling

UAV Data Acquisition

Land lidar point cloud and high-resolution images were obtained by UAV. The flight route was planned, including altitude, heading coverage, heading overlap, lateral overlap, image tilt angle, maximum flight tilt angle, and adjacent image height difference. In this study, DJI Matrice 300 RTK was used as a UAV platform, which was equipped with Zenmuse L1 system. The Zenmuse L1 integrates a Livox lidar module, a high inertial measurement unit, and a camera with a one-inch CMOS on a three-axis stabilized gimbal. The nominal horizontal accuracy of the system is 10 cm at 50 m, and the vertical accuracy is 5 cm at 50 m. The system can achieve all-weather, high-efficiency real-time 3D data acquisition and high-precision post-processing reconstruction in complex scenes.

Lidar Point Cloud and Imagery Data Processing

The data collected in the previous step were processed, including UAV overlapping route cutting, projection and coordinate transformation, point cloud data filtering and classification (including ground, low vegetation, medium vegetation, high vegetation, and building), spatial resampling, and accuracy analysis.

Land Digital Terrain Modeling

First, the airborne lidar point cloud data were used to interpolate the filtered ground point cloud data, and the high-fidelity DEM was constructed. Then DEM and aerial images were combined to generate a digital orthophoto map (DOM). Finally, with the help of point cloud data and feature points in images (such as road inflection points, and riverbanks), the registration and fusion of DOM and DEM were completed.

ICESat-2 Photon Point Cloud Denoising and Extraction

The *ICESat-2* ATLAS photon point cloud was used as active reference remote sensing data to extract shallow underwater terrain (Figure 3a). An underwater terrain signal denoising and extraction method based on density clustering and distance statistics was adopted to reduce the environmental noise (Xie *et al.* 2021). Subsequently, the extracted point cloud was subjected to a water refraction correction to obtain the final water depth. The flowchart is shown in Figure 2.

Bathymetric Inversion Adaptability Verification

Through the previous step, the underwater effective depth point was obtained. In the typical river area, through the river terrain stereo observation experiment, with the single-beam sonar sounding data as the true value, *ICESat-2* bathymetric inversion adaptability verification was carried out (Figure 2). Taking single-beam sonar data as the true value, the two sets of data were spatially superimposed, and root mean square error (RMSE) and average relative error (MRE)) were used as evaluation indexes to do correlation analysis.

In this study, the survey ship was equipped with a single-beam sonar system as an observation platform for collecting measured water depth, supplemented by shallow stratum profile instrument, Acoustic Doppler Current Profiler, GNSS, Inertial Positioning and Navigation System, and other equipment. The single-beam sonar equipment model is an Odom Hydrotrac II from Teledyne RD Instruments. The sounding accuracy and horizontal accuracy meet the International Hydrographic Organization (IHO) Order I standard. The sounding accuracy is better than $(0.25 + (0.013 \times \text{depth})^2)^{1/2}$ m, and the horizontal accuracy is better than $(5 + 0.05 \times \text{depth})$ m. The data acquisition scenario is shown in Figure 3b.

Bathymetric Inversion by Active and Passive Fusion

Sentinel-2 multi-spectral imagery data were used as passive reference remote sensing data to extract shallow underwater terrain. Some *ICESat-2* underwater points were randomly selected as the training set, and the rest were used as the test set. A classical empirical model (multi-band linear regression model) was established to invert the underwater terrain and generate a 10-m-resolution underwater 3D terrain (Taganos *et al.* 2018). The multi-band linear regression model assumes that the ratio of reflectivity of two bands of any water pixel on the same scene image is constant (Taganos *et al.* 2018):

$$z = a_0 + \sum_{i=1}^{N} a_i \ln[(R(\lambda_i) - R_\infty(\lambda_i)] \quad (1)$$

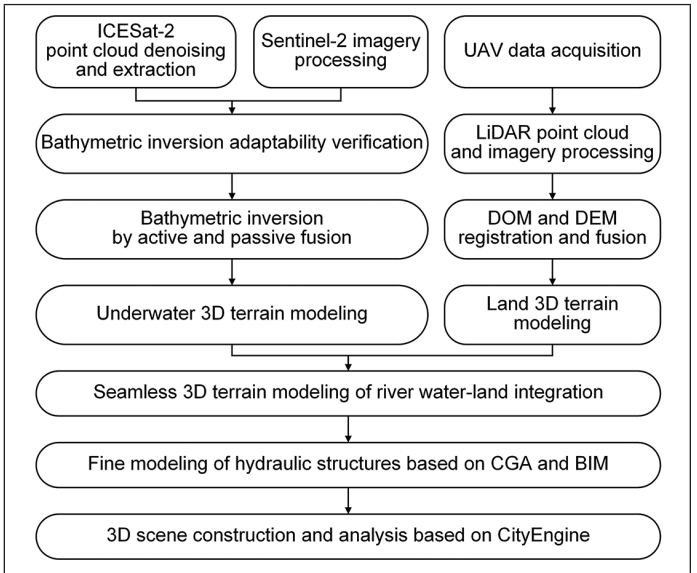

Figure 1. Flowchart of 3D scene model reconstruction method of river water-land integration.

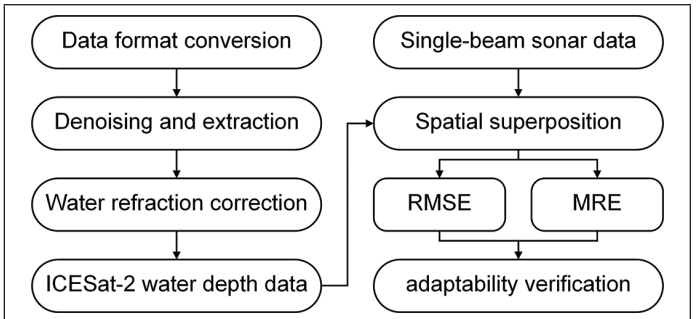

Figure 2. Underwater signal extraction and bathymetric inversion adaptability verification of *ICESat-2* ATLAS photon point cloud.

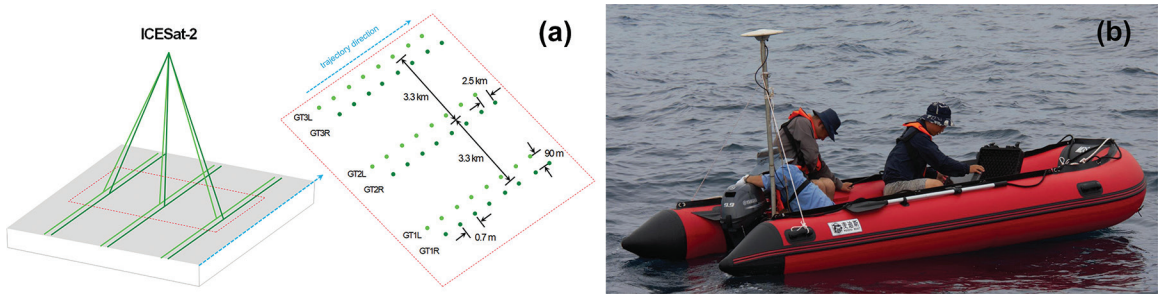

Figure 3. Source of bathymetric data for *ICESat-2*. (a) *ICESat-2* ATLAS photon point ground footprint distribution. (b) Single-beam sonar sounding data by survey ship.

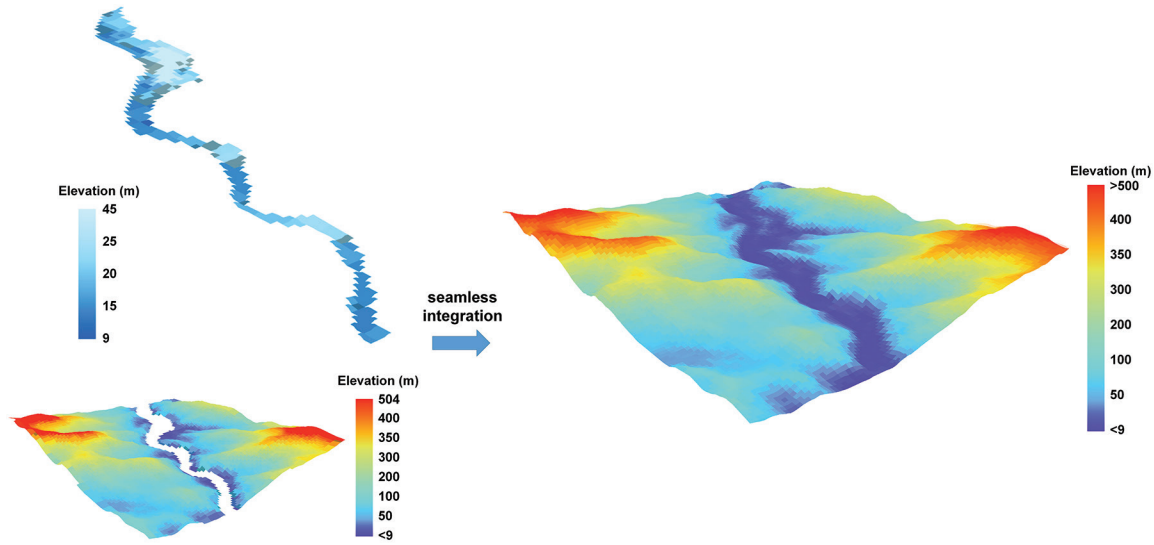

Figure 4. Seamless 3D terrain of river water-land integration steps.

Here, z represents water depth, N represents the number of bands, a_0 and a_i are coefficients of the linear regression model, $R(\lambda_i)$ is the radiance of shallow water in the ith band of multi-spectral imagery, and $R_\infty(\lambda_i)$refers to the radiation of deep water bodies in adjacent areas of the ith band.

Through the correlation analysis between the reflectivity of each band and the measured water depth, the band with the largest correlation coefficient is selected (Taganos *et al.* 2018). Therefore, in multi-band linear regression model, the blue band (458–522 nm), green band (543–577 nm), and red band (650–680 nm) were selected.

3D Scene Construction of Water-Land Integrated Model

Seamless Fusion 3D Terrain Modeling of River Water-Land Integration

First, the spatial reference of land and underwater 3D terrain data was unified. The elevation value of the smallest of all the pixel elevation values along the river shoreline was used as the water surface elevation reference, and the water depth was reduced to the elevation. The river shoreline was extracted by remote sensing imaging.

Then the global public DEM data sets Advanced Spaceborne Thermal Emission and Reflection Radiometer Global Digital Elevation Model (ASTER GDEM) were introduced as the filling data, and the terrain filling algorithm based on the triangulated irregular network (TIN) difference surface was used to fill the possible voids at the junction of underwater and underwater terrain (Grohman *et al.* 2006; Robinson *et al.* 2014) so as to realize the seamless integration of the 3D water-land terrain.

Finally, an adaptive filtering method based on neighborhood statistics was adopted to smooth the fusion model and further filter out possible outliers (Ruan *et al.* 2020). Figure 4 shows the detailed integration process of seamless fusion 3D terrain results of river water-land integration.

Fine Modeling of Hydraulic Structures Based on CGA Rules and BIM Technology

In this article, CityEngine was used as the basic platform for 3D scene construction of water-land integrated model and realized the complementary advantages of 3D real scene terrain and individual models (such as building models). The collaborative modeling was based mainly on CGA rule modeling method, supplemented by the third-party BIM technology (Revit, 3DMax, and Blender) and the Motion Structure Recovery (SFM) photogrammetry method.

3D Scene Construction and Analysis Based on CityEngine

The 3D scene data included map, image, texture, and single structured model data. For some complex hydraulic structure models, they can be imported into the 3D scene in FileGDB format after structural modeling. After the rule definition and model import, the 3D scene can be modeled. Based on the generated WebScene reality model, the CityEngine analysis module can be used for 3D visibility, including the Viewshed Tool, ViewDome Tool, and ViewCorridor Tool.

Results and Discussion

Result of 3D Terrain Modeling of River Land

Taking the Xin'an River Basin in Zhejiang Province of the People's Republic of China as the research area, its remote sensing image and land 3D point cloud are shown in Figure 5.

The DEM was generated from the airborne lidar point cloud data, and then the 3D model of the land part of the river was obtained by registration and fusion with DOM, shown in Figure 6. The average elevation of the area is about 237 m.

Result of Underwater Photon Point Cloud Extraction

Figure 7 shows the extraction results of some underwater points along the trajectory direction of an *ICESat-2* trajectory in the study area. In the figure, the x-axis is along the trajectory direction, and the y-axis is the instantaneous water depth. According to the above denoising method, a large number of noise points in ATL03 raw photons were filtered out,

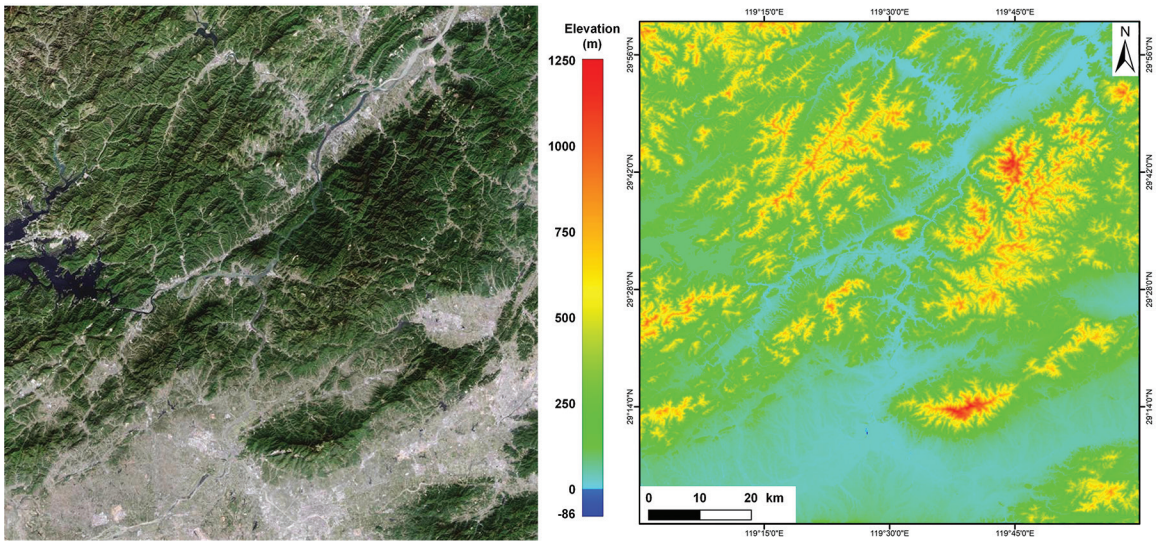

Figure 5. Remote sensing imagery and land 3D point cloud in the study area (Xin'an River Hydropower Station and its upstream image).

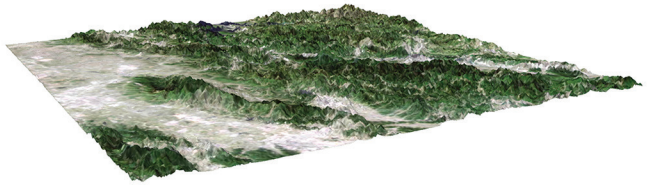

Figure 6. River-land digital terrain model.

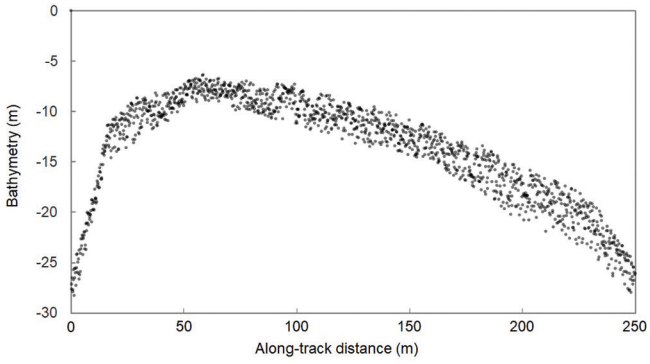

Figure 7. Extraction result of underwater photon point cloud along-track distance. The x-axis represents the direction along the trajectory, and the y-axis represents the instant water depth in meters.

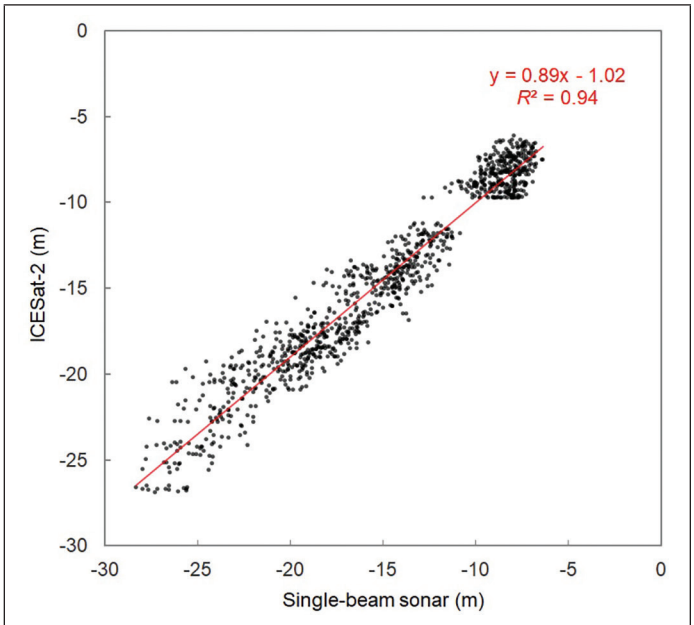

Figure 8. Comparison of *ICESat-2* data and single-beam sonar data.

which was the key to further calculation of local water depth. Figure 9 shows the remote sensing image of this area. From Figures 7 and 9, it can be seen that along the *ICESat-2* trajectory direction, from southeast to northwest, the water depth changes from deep to shallow and then slowly to deep, with an average depth of about 13.8 m. The shallowest point appears on a river highland, with a minimum depth of about 6.4 m.

In the above area, the sounding adaptability of *ICESat-2* data was verified by sonar measured data. The effective sounding range of single-beam sonar was 0 to 40 m, and the sampling interval of water depth point was 5 m. First, in the sonar coverage area, sonar data interpolation was used to establish a water depth grid with a resolution of 5 m. Then the *ICESat-2* data in the overlapping area of the two were diluted at 5-m intervals to obtain a total of 1033 effective water depth points. Finally, the grid depth value was extracted by superposition analysis, and the correlation analysis was carried out. The results are shown in Figure 8. In the overlapping area, the correlation between the two is high, and the correlation coefficient (R2) is close to 0.9.

RMSE and MRE were used as evaluation indexes to further verify the error distribution of *ICESat-2* effective water depth:

$$RMSE = \sqrt{\frac{1}{n}\sum_{i=1}^{n}\Delta_i^2}$$

$$MRE = \frac{1}{n}\sum_{i=1}^{n}\frac{|\Delta_i|}{h_i}$$

Here, Δi is the error between the *ICESat-2* water depth value and the corresponding sonar water depth value, h_i represents the sonar water depth value, and $_n$ is the number of water depth points.

Quantitative analysis was carried out according to the water depth range, and the results are shown in Table 1. The overall accuracy of *ICESat-2* sounding in the study area has an RMSE of less than 1.5 m, and MRE is about 8%. The overall sounding accuracy is basically in line with the IHO-S44 standard, which has certain reliability, and the accuracy is the best in the shallow waters of 10 m. It is proved that the

prior data set for shallow-water depth inversion can be obtained from the processed *ICESat-2* point cloud.

Table 1. Comparison of *ICESat-2* data and single-beam sonar data

	Water Depth Range (m)	RMSE (m)	MRE (%)
Range 1	0–10	1.08	9.72
Range 2	10–20	1.50	7.14
Range 3	20–30	1.95	6.88
Overall	0–30	1.46	8.31

Inversion Results and Discussion of Underwater Terrain

The bathymetric inversion experiment was designed as follows. The *ICESat-2* water depth was processed by point cloud denoising and extraction. Some water depth points were randomly selected as the training set, and the remaining water depth points were used as the test set to establish the inversion model data set. In the above study area, 750 water depth points were randomly selected as the training set and 750 water depth points as the test set. The underwater terrain extraction result is shown in Figure 9.

Through the correlation analysis, as shown in Figure 10, the correlation between the inversion water depth data and the *ICESat-2* sounding data is high (R^2 = 0.86). Quantitative analysis was performed according to the water depth range, and the results are shown in Table 2. The overall accuracy (RMSE) of the above regions is less than 2 m, the MRE is about 9%, and the accuracy is best in shallow waters of 10 m. It is proved that this method can effectively extract the shallow underwater terrain of the river.

Table 2. Accuracy statistics of bathymetric inversion

	Water Depth Range (m)	RMSE (m)	MRE (%)
Range 1	0–10	1.26	13.00
Range 2	10–20	1.59	8.45
Range 3	20–30	2.42	9.63
Overall	0–30	1.87	9.09

Results and Discussion of Seamless 3D Scene

Using the above modeling method, the seamless fusion 3D terrain result of river water-land integration is shown in Figure 11.

The reliability of the results was verified by ASTER GDEM with a resolution of 30 m. Terrain fusion results were evaluated by constructing water depth profiles. In the above research, a representative section line in the southeast-northwest direction was constructed, and the topographic relief of the seamless fusion terrain and the public data set was compared, as shown in Figure 12. The profile line passes through the river, and the elevation range is between 16 and 259 m. The results show that the terrain undulation of the two is roughly close and that the resolution of the fused terrain is higher. The underwater terrain undulation of the fused terrain model is closer to the reality, which is due to the fusion of remote sensing inversion results. In addition, due to the resolution, ASTER GDEM terrain expression is not fine enough, especially at the land-water transition zone.

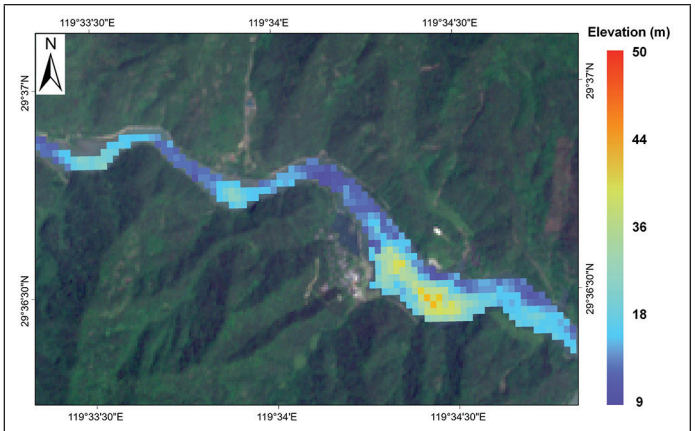

Figure 9. Underwater terrain based on active and passive fusion.

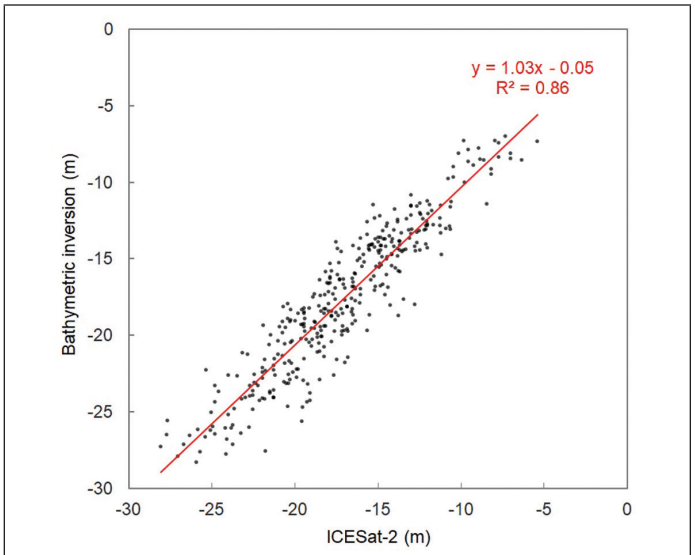

Figure 10. Comparison of bathymetric inversion and *ICESat-2* data.

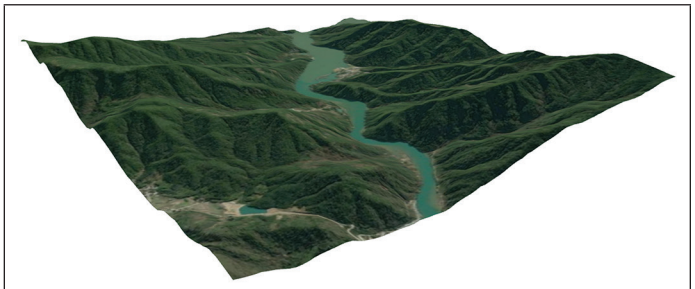

Figure 11. Land-underwater high-fidelity seamless digital terrain fusion result.

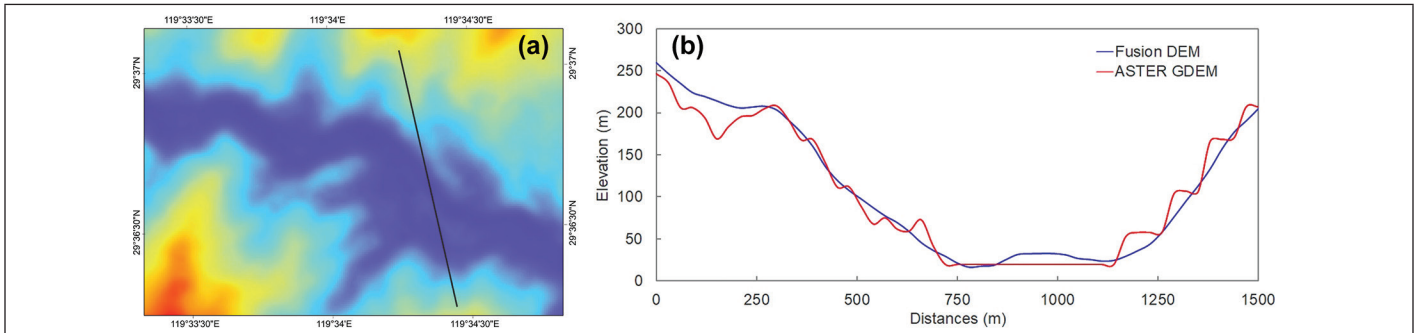

Figure 12. Comparative analysis of elevation profile. The y-axis represents elevation, and the x-axis represents profile distance. Units are meters. The blue line represents fusion terrain, and red line represents ASTER GDEM results.

Based on CGA rules and BIM technology, the fine 3D models of hydraulic structures were quickly constructed in batches (Figure 13). By editing the CGA rule file and assigning it to different vector data for definition, regular building models, road models, and green space models can be generated in batches. For more complex hydraulic structure models, BIM software can be used for structural modeling. The SFM photogrammetry method can also be used as a complementary means for 3D modeling of extremely complex components.

The expected effect of the river 3D scene model of river water-land integration is shown in Figure 14. The visible and invisible zone of the 3D scene can be identified and analyzed.

Limitations and Prospects

The method proposed in this article has some limitations. Although some underwater photon positions of *ICESat-2* can be obtained by correction, the underwater photon transmission process is more affected by factors than terrestrial photons (Neuenschwander and Magruder 2016; Liu *et al.* 2021). This means that not all inland shallow-water bottom signals can be detected, especially in deep-water areas. In line with the experimental results in this article, when the water depth exceeds 20 m, the accuracy will deteriorate sharply, which is bound to reduce the availability of data.

In addition, the measurement depth of remote sensing inversion is affected by water clarity. Studies have shown that the maximum depth mapping performance of *ICESat-2* ATLAS is close to 1 Secchi in depth (Parrish *et al.* 2019). In Class II waters, the maximum water depth retrieved by *ICESat-2* is limited. According to the statistical data, the average water quality of the main stream in the study area is excellent, and the water quality is Class I to II. Therefore, there is a degree of uncertainty in the terrain results.

As a rare active detection method, *ICESat-2* ATLAS has the ability to obtain water depth information of rivers and lakes in small areas due to its advantages of trajectory and footprint points. With the gradual increase of *ICESat-2* trajectories, it will be possible to use active and passive fusion technology to map and monitor changes in river and lake water depths worldwide.

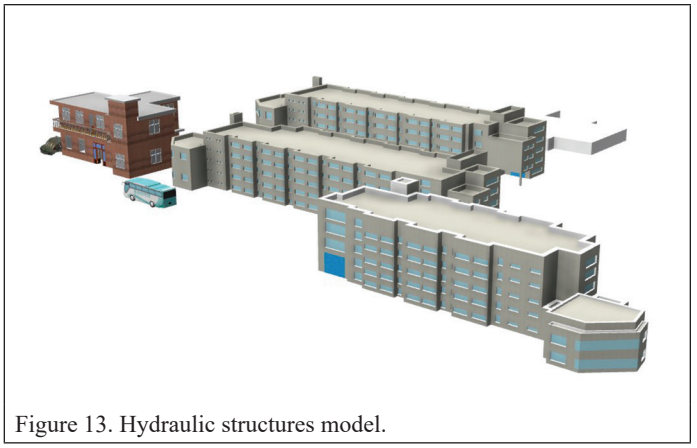

Figure 13. Hydraulic structures model.

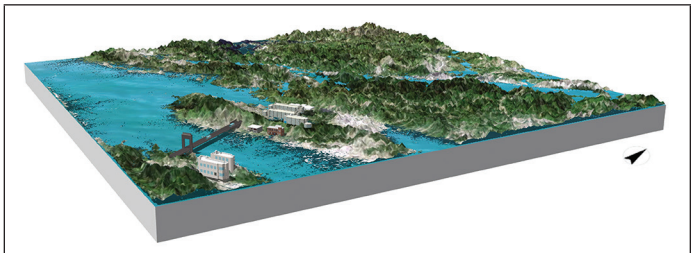

Figure 14. 3D scene model of river water-land integration.

Conclusion

This paper proposes a 3D scene modeling method of river water-land integration. The inland basin high-fidelity land-underwater seamless digital terrain and the water-land integration 3D real scene models are formed. The overall accuracy (RMSE) of the study area is less than 2 m, and the accuracy is the best in the shallow-water area of 10 m. The performance of the seamless fusion 3D terrain is better than the public DEM data set. It can meet the needs of basic geographic information data of a river- and lake-integrated 3D scene model and can be used as a reference for 3D scene modeling of inland basins in similar areas.

Acknowledgment

This work was funded by the Zhejiang Provincial Natural Science Foundation of China (LZJWY22E090002) and the Zhejiang Water Conservancy Science and Technology Plan Project (RC2141). Sincere thanks are given for the comments and contributions of anonymous reviewers and members of the editorial team.

References

Albright, A., and Glennie, C. 2020. Nearshore bathymetry from fusion of Sentinel-2 and ICESat-2 observations. *IEEE Geoscience and Remote Sensing Letters* 18:900–904.

Badwi, I. M., Ellaithy, H. M. and Youssef, H. E. 2022. 3D-GIS parametric modelling for virtual urban simulation using CityEngine. *Annals of GIS* 28(3):325–341.

Collin, A., Etienne, S. and Feunteun, E. Feunteun. 2017. VHR coastal bathymetry using WorldView-3: Colour versus learner. *Remote Sensing Letters* 8(11):1072–1081.

Collin, A., Hench, J. L., Pastol, Y., Planes, S., Thiault, L., Schmitt, R. J., Holbrook, Sally. J., Davies, N. and Troyer, M. 2018a. High resolution topobathymetry using a Pleiades-1 triplet: Moorea Island in 3D. *Remote Sensing of Environment* 208:109–119.

Collin, A., Ramambason, C., Pastol, Y., Casella, E., Rovere, A., Thiault, L., Espiau, B., Siu, G., Lerouvreur, F., Nakamura, N., Hench, J., Schmitt, R. J., Holbrook, Sally. J., Troyer, M. and Davies, N. 2018b. Very high resolution mapping of coral reef state using airborne bathymetric LiDAR surface-intensity and drone imagery. *International Journal of Remote Sensing* 39(17):5676–5688.

Du, J., CHEN, D., Zhang, Z. and Zhang, L. 2019. Research progress of building reconstruction via airborne point clouds. *Journal of Remote Sensing* 23(3):374–391.

Duan, Y., Liu, Y., Li, M., Zhou, M. and Yang, Y. 2016. Survey of reefs based on Landsat 8 operational land imager (OLI) images in the Nansha Islands, South China Sea. *Acta Oceanologica Sinica* 35(10):11–19.

Gholamalifard, M., Esmaili Sari, A., Abkar, A. and Naimi, B. 2013. Bathymetric modeling from satellite imagery via single band algorithm (SBA) and principal components analysis (PCA) in southern Caspian Sea. *International Journal of Environmental Research* 7(4):877–886.

Grohman, G., Kroenung, G. and Strebeck, J. 2006. Filling SRTM voids: The delta surface fill method. *Photogrammetric Engineering and Remote Sensing* 72(3):213–216.

Hedley, J. D., Roelfsema, C., Brando, V., Giardino, C., Kutser, T., Phinn, S., Mumby, P., Barrilero, Omar., Laporte, Jean. and Koetz, B. 2018. Coral reef applications of Sentinel-2: Coverage, characteristics, bathymetry and benthic mapping with comparison to Landsat 8. *Remote Sensing of Environment* 216:598–614.

Kim, K. and Wilson, J. P. 2015. Planning and visualising 3D routes for indoor and outdoor spaces using CityEngine. Journal of Spatial Science, 2015, 60(1), pp, 179-193.

Leigh, H. W., Magruder, L. A., Carabajal, C. C., Saba, J. L. and McGarry, J. F. 2014. Development of onboard digital elevation and relief databases for ICESat-2. *IEEE Transactions on Geoscience and Remote Sensing* 53(4):2011–2020.

Liu, C., Qi, J., Li, J., Tang, Q., Xu, W., Zhou, X. and Meng, W. 2021. Accurate refraction correction–assisted bathymetric inversion using ICESat-2 and multispectral data. *Remote Sensing* 13(21):4355.

Lyzenga, D. R. 1981. Remote sensing of bottom reflectance and water attenuation parameters in shallow water using aircraft and Landsat data. *International Journal of Remote Sensing* 2(1):71–82.

Ma, Y., Xu, N., Liu, Z., Yang, B., Yang, F., Wang, X. H. and Li, S. 2020. Satellite-derived bathymetry using the ICESat-2 lidar and Sentinel-2 imagery datasets. *Remote Sensing of Environment* 250:112047.

Neuenschwander, A. L. and Magruder, L. A. 2016. The potential impact of vertical sampling uncertainty on ICESat-2/ATLAS terrain and canopy height retrievals for multiple ecosystems. *Remote Sensing* 8(12):1039.

Okolie, C. J. and Smit, J. L. 2022. A systematic review and meta-analysis of digital elevation model (DEM) fusion: Pre-processing, methods and applications. *ISPRS Journal of Photogrammetry and Remote Sensing* 188:1–29.

Parrish, C. E., Magruder, L. A., Neuenschwander, A. L., Forfinski-Sarkozi, N., Alonzo, M. and Jasinski, M. 2019. Validation of ICESat-2 ATLAS bathymetry and analysis of ATLAS's bathymetric mapping performance. *Remote Sensing* 11(14):1634.

Pham, H. T., Marshall, L., Johnson, F. and Sharma, A. 2018. A method for combining SRTM DEM and ASTER GDEM2 to improve topography estimation in regions without reference data. *Remote Sensing of Environment* 210:229–241.

Robinson, N., Regetz, J. and Guralnick, R. P. 2014. EarthEnv-DEM90: A nearly-global, void-free, multi-scale smoothed, 90m digital elevation model from fused ASTER and SRTM data. *ISPRS Journal of Photogrammetry and Remote Sensing* 87:57–67.

Ruan, X., Cheng, L., Chu, S., Yan, Z., Zhou, X., Duan, Z. and Li, M. 2020. A new digital bathymetric model of the South China Sea based on the subregional fusion of seven global seafloor topography products. *Geomorphology* 370:107403.

Ruan, X., Yang, F., Guo, M. and Zou C. 2022. Three-dimensional scene modeling method of river water-land integration, Pages 463–467 in *2022 International Conference on Information Technology and Biomedical Engineering (ICITBE)*, held in Hangzhou, China, 23–25 December 2022.

Traganos, D., Poursanidis, D., Aggarwal, B., Chrysoulakis, N. and Reinartz, P. 2018. Estimating satellite-derived bathymetry (SDB) with the google earth engine and Sentinel-2. *Remote Sensing* 10(6):859.

Tang, D., Kester, D., Wang, Z., Lian, J. and Kawamura, H. 2003. AVHRR satellite remote sensing and shipboard measurements of the thermal plume from the Daya Bay, nuclear power station, China. *Remote Sensing of Environment* 84(4):506–515.

Xie, C., Chen, P., Pan, D., Zhong, C. and Zhang, Z. Improved filtering of ICESat-2 lidar data for nearshore bathymetry estimation using Sentinel-2 imagery. *Remote Sensing* 13(21):4303.

Yue, L., Shen, H., Zhang, L., Zheng, X., Zhang, F. and Yuan, Q. 2017. High-quality seamless DEM generation blending SRTM-1, ASTER GDEM v2 and ICESat/GLAS observations. *ISPRS Journal of Photogrammetry and Remote Sensing* 123:20–34.

Zhang, L., Li, Z., Li, A. and Liu, F. 2018. Large-scale urban point cloud labeling and reconstruction. *ISPRS Journal of Photogrammetry and Remote Sensing* 138:86–100.

Zhou, X., Meng, X., Zhang, X. and MI, Y. 2016. A method for urban real 3D model building based on oblique photogrammetry. *Science of Surveying and Mapping* 41(9):159–163.

In-Press Articles

Multi-level Perceptual Network for Urban Building Extraction from High-Resolution Remote Sensing Images. Jinlong Chen, Yueming Sun, Xiao Huang, Hongsheng Zhang.

Classifying Building Roof Damage Using High Resolution Imagery for Disaster Recovery. Elaina Gonsoroski, Yoonjung Ahn, Emily W. Harville, Nathaniel Countess, Maureen Y. Lichtveld, Ke Pan, Leslie Beitsch, Samendra P. Sherchan, and Christopher K. Uejio

A Lightweight Conditional Convolutional Neural Network for Hyperspectral Image Classification. Linfeng Wu, Huajun Wang, and Huiqing Wang.

Estimation of the Forest Stand Biomass and Greenhouse Gas Emissions Using Lidar Surveys. Rida Sultanova and Radik Mustafin.

Edge Detection Method for High-Resolution Remote Sensing Imagery by Combining Superpixels with Dual-Threshold Edge Tracking. Yanxiong Liu, Zhipeng Dong, Yikai Feng, Yilan Chen, and Long Yang

Expansion of Urban Impervious Surfaces in Lahore (1993–2022) Based on GEE and Remote Sensing Data. Muhammad Nasar Ahmad, Zhenfeng Shao, Akib Javed, and Fakhrul Islam.

Small Object Detection in Remote Sensing Images Based on Window Self-Attention Mechanism. Jiaxin Xu, Qiao Zhang, Yu Liu, and Mengting Zheng.

Call for *PE&RS* Special Issue Submissions

Innovative Methods for Geospatial Data using Remote Sensing and GIS

Internationally comparable data is a global need for managing resources, monitoring current trends and taking actions for sustainable living. Even though there has been a significant progress on geospatial data availability, extensive data gaps are still a major problem for general assessment and supervise the progress through the years. According to United Nations 2022 The Sustainable Development Goals Report, while health and energy sectors have the highest data available, limited data available for climate action.

The COVID-19 crisis has also shown that there are innovative data collection methods utilizing information and computer technologies. However, only 5% of the countries have benefit from remote sensing technologies to measure the impact of COVID-19. Additionally, novel approaches such as artificial intelligence should be used in conjunction with assessments to make sure they are put to use for critical situations.

The recent developments in remote sensing, geographic information systems and ICT have provided a wide accessibility to create geospatial data for various purposes. The proposed special issue focuses on *"Innovative Methods for Geospatial Data using Remote Sensing and GIS" for wide range of applications. This special issue aims to bring researchers to share knowledge and their expertise about innovative methods to contribute to fill data gaps around the world for a better future.*

The proposed special issue aims to contributes ASPRS's key mission on 'Simplify and promote the use of image-based geospatial technologies for the end-user', 'Promote collaboration between end users and geospatial experts to match data and technology to applications and solutions' and 'promote the transfer of geospatial data and information technology to developing nations' by providing innovative methods to create geospatial data using remote sensing and geographic information systems utilizing state-of-the-art developments and solutions.

Deadline for Manuscript Submission—July 1, 2023

Submit your Manuscript to http://asprs-pers.edmgr.com

Guest Editors

Dr. Tolga Bakirman, bakirman@yildiz.edu.tr , *Yildiz Technical University, Department of Geomatic Engineering*, Davutpasa Campus, 34220 Esenler-Istanbul/Turkey

Dr. George Arampatzis, garampatzis@pem.tuc.gr, *Technical University Crete, School of Production Engineering & Management*, 73100 Chania – Crete/Greece

High-Resolution Aerosol Optical Depth Retrieval in Urban Areas Based on Sentinel-2

Yunping Chen, Yue Yang, Lei Hou, Kangzhuo Yang, Jiaxiang Yu, and Yuan Sun

Abstract

In this paper, an improved aerosol optical depth (AOD) retrieval algorithm is proposed based on Sentinel-2 and AErosol RObotic NETwork (AERONET) data. The surface reflectance for AOD retrieval was estimated from the image that had minimal aerosol contamination in a temporal window determined by AERONET data. Validation of the Sentinel-2 AOD retrievals was conducted against four Aerosol Robotic Network (AERONET) sites located in Beijing. The results show that the Sentinel-2 AOD retrievals are highly consistent with the AERONET AOD measurements (R = 0.942), with 85.56% falling within the expected error. The mean absolute error and the root-mean-square error are 0.0688 and 0.0882, respectively. In addition, the AOD distribution map obtained by this algorithm well reflects the fine-spatial-resolution changes in AOD distribution. These results suggest that the improved high-resolution AOD retrieval algorithm is robust and has the potential advantage of retrieving high-resolution AOD over urban areas.

Introduction

Air pollution is a byproduct of urban and industrial development, and it not only pollutes the environment and reduces visibility but also causes respiratory and cardiovascular diseases (Shirangi *et al.* 2022). Because of its spatial and temporal variability, monitoring air quality and understanding its distribution in a timely and accurate manner can effectively improve pollution control (Islam *et al.* 2022; Zheng *et al.* 2019; Mazlan *et al.* 2023). Due to its large-scale, continuous timeliness and low-cost observations, satellite remote sensing technology has become a powerful means of regional and global air quality monitoring (Singh *et al.* 2021).

In recent decades, some aerosol optical depth (AOD) retrieval algorithms and satellite aerosol products have been developed (Hou *et al.* 2020; Kaufman *et al.* 1997; Hsu *et al.* 2004). However, most of these satellite aerosol products have coarse resolutions and cannot reflect the fine-spatial-resolution changes in aerosol distributions caused by changes in construction, traffic distribution, and population density in urban areas. Thus, it is difficult to meet the demand for fine-scale air quality monitoring in urban areas (Zhang and Cao 2015; Li *et al.* 2019). Therefore, aerosol retrieval based on high spatial-resolution remote sensing images has important research value and broad application prospects.

The most crucial challenge for high spatial resolution aerosol retrieval is estimating surface reflectance. The methods used to estimate surface reflectance in aerosol retrieval algorithms can be broadly classified into two types, namely, methods based on empirical relationships of specific bands and methods based on surface reflectance databases, represented by the dark dense vegetation (DDV) algorithm and deep blue (DB) algorithm, respectively. The widely used DDV algorithm, which is based on the reflectance relationship between the Short-Wave InfraRed (SWIR) band and red/blue band, was proposed for moderate resolution imaging spectroradiometer (MODIS) (Xiong *et al.* 2016; Chen *et al.* 2014). However, due to the difference in the spectral response of different sensors in the same band, the empirical relationship for MODIS may cause errors when applied to high-spatial-resolution sensors. Some improvements have been made in recent years. Wei *et al.* used a large number of Landsat series high-spatial-resolution images to refit the empirical relationship between the SWIR band and red/blue over dense vegetation pixels, i.e., normalized difference vegetation index (NDVI) greater than 0.55. This improved DDV algorithm was applied to Landsat series images to retrieve AOD products with a 30 m resolution (Wei *et al.* 2013). Olivier *et al.* used *Landsat 5* and *Landsat 7* data to fit the empirical relationship between the reflectance of the SWIR band and red/blue band, where NDVI was greater than 0.2 (Olivier *et al.* 2015). However, the empirical relationships between the reflectances of specific bands in the above studies still had time and space limitations, making it difficult to apply them to different locations and different times.

Inspired by the DB algorithm (Hsu *et al.* 2004), some AOD retrieval algorithms based on the surface reflectance database have also been applied to the AOD retrieval of high-spatial-resolution images. Wei *et al.* used Landsat 4-7 surface reflectance products and constructed a 30 m resolution surface reflectance database divided by month for AOD retrieval (Wei *et al.* 2013). Bilal and Qiu used Landsat 8 images to construct a surface reflectance database combined with the Simplified Aerosol Retrieval Algorithm (SARA) algorithm for AOD retrieval (Bilal and Qiu 2018). Omari *et al.* used Landsat 8 images to construct a surface database cataloged by year to retrieve AOD in the United Arab Emirates (Omari *et al.* 2019). However, due to the low temporal resolution, cloud contamination and other weather factors, Landsat 8 images are usually inadequate for establishing a surface database.

In this study, an improved method for high-spatial-resolution AOD retrieval is proposed by conducting high-spatial-resolution AOD research using *Sentinel-2* remote sensing images. *Sentinel-2*'s high spatial resolution and relatively high revisit time are taken advantage of in this algorithm, and the ground AERONET monitoring data are used to determine the "cleanest" image in a temporal window. The surface reflectance of *Sentinel-2* corresponding to the "cleanest image" then constitutes the surface reflectance database. Based on this database, the AOD of the *Sentinel-2* images, which share the same time window as the images in the database, can be retrieved. In this study, *Sentinel-2* images from 2017 to 2019 in the Beijing area are obtained from AOD retrieval experiments, and the retrieval results are validated by AERONET AOD data.

Study Area and Data

Study Area

Beijing is located in the northwestern part of the North China Plain, 39.4°–41.6° N, 115.7°–117.4° E, and has a total area of 16 410.54 square km. Beijing has a complex surface and a variety of land use types. As shown in Figure 1, to the west, north, and northeast of

Yunping Chen*, Yue Yang, Lei Hou, Kangzhuo Yang, and Jiaxiang Yu are with the School of Automation Engineering, University of Electronic Science and Technology of China (chenyp@uestc.edu.cn).

Yuan Sun* is with the Aerosphere Information Research Institute, Chinese Academy of Science, China (sunyuan@aircas.ac.cn).

**Corresponding authors*

Contributed by Dongdong Wang, October 11, 2022 (sent for review January 15, 2023; reviewed by Weizhen Hou, Ashraf Dewan).

Photogrammetric Engineering & Remote Sensing
Vol. 89, No. 6, June 2023, pp. 361–371.
0099-1112/22/361–371

doi: 10.14358/PERS.22-00122R2

Beijing are Xi Mountain and Jundu Mountain, which are covered by lush vegetation. To its south and southeast, the North China Plain exists and contains mainly farmland. The central part is the urban area of Beijing, which has scarce vegetation. Because of the high population density, congested urban traffic, and large-scale industrial emissions in the Beijing-Tianjin-Hebei region, this city has experienced severe air pollution. In addition, due to the complex surface types and high surface reflectance in the Beijing area, aerosol retrieval is more difficult. On the other hand, Beijing is also a popular area for aerosol retrieval research because of the sufficient number of ground aerosol monitoring sites (Wei *et al.* 2013; Wei and Sun 2017; Luo *et al.* 2015; Bai *et al.* 2008; Zhou *et al.* 2009). In Figure 1, the four red dots denote the four AERONET sites in Beijing's downtown area.

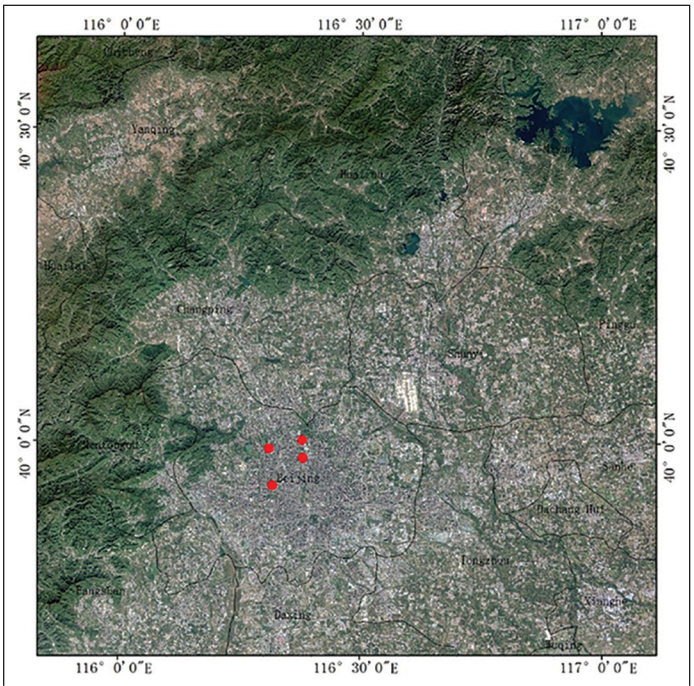

Figure 1. Beijing Sentinel-2 red-green-blue (RGB) color image (dots in the picture are the Beijing AERONET sites).

Sentinel-2 Data

Sentinel satellites are the core part of the global environment and safety monitoring plan (renamed the Copernicus Plan in 2013) formulated by the European Commission and the European Space Agency. The purpose is to cooperate with other satellites to further improve their environmental monitoring capabilities and disaster response speed to achieve dynamic monitoring of the global environment and climate change (Li and Roy 2017).

The Sentinel-2A/B satellite operates in a sun-synchronous orbit in polar orbit, with an orbit height of 786 km, an orbit inclination of 98.62°, and a swath width of 290 km (Spoto 2012). *Sentinel-2*'s revisit period near the equator is 10 days, and the constellation shortens the revisit period to five days, reaching two–three days in mid-latitudes. The observation area of *Sentinel-2* covers 56°S–84°N and can provide observation data for most parts of the world.

The *Sentinel-2* satellite carries a push-broom multispectral instrument (MSI) with 13 spectral bands ranging from the visible to shortwave infrared bands. Its blue (B2, 0.49 μm), green (B3, 0.56 μm), red (B4, 0.665 μm), and near-infrared (B8,0.842 μm) channels have a resolution of 10 m; its red edge (B5, 0.705 μm), near-infrared (NIR) (B6, 0.74 μm; B7, 0.783 μm; B8A, 0.865 μm), and shortwave infrared (SWIR) (B11, 1.61 μm; B12, 2.19 μm) have a ground sampling distance of 20 m; its coastal aerosol (B1, 0.443 μm) has a spatial resolution of 60 m (Harmel *et al.* 2018; Yang *et al.* 2021).

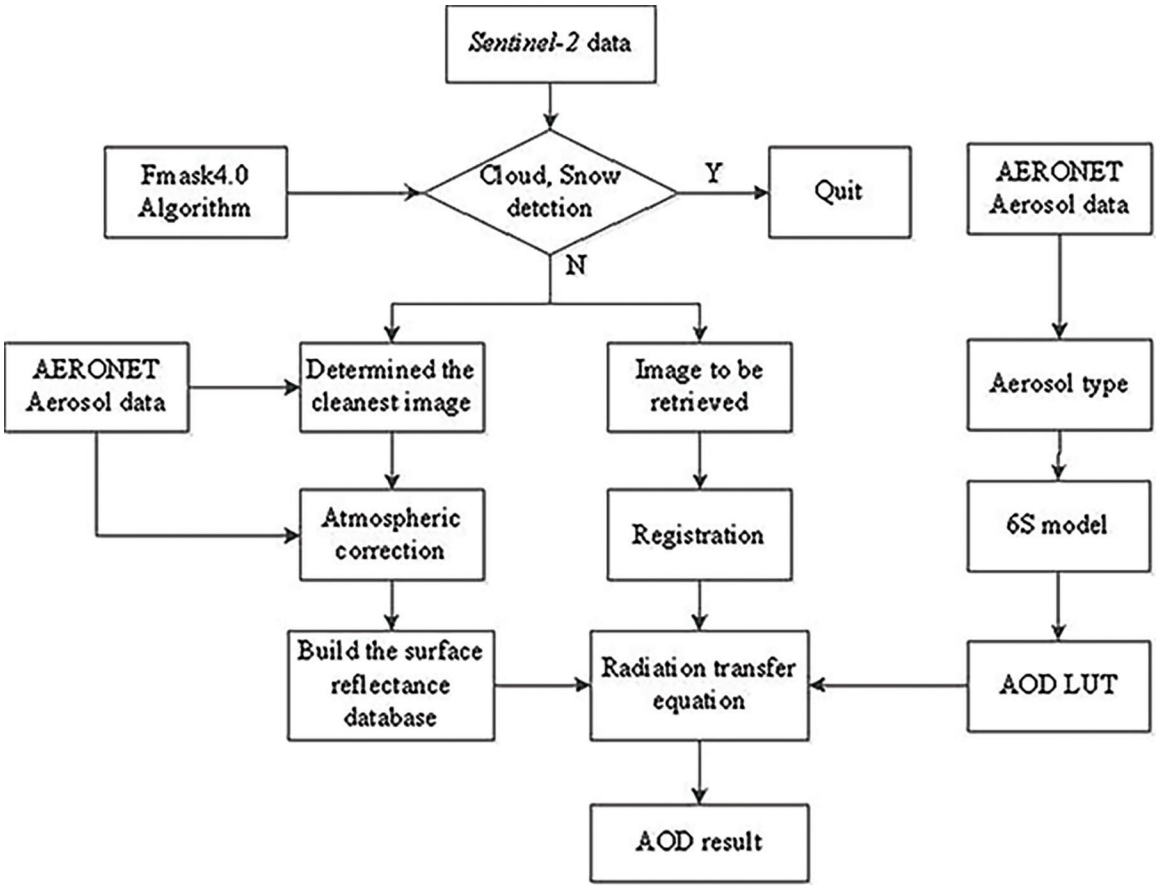

Figure 2. Flow chart of the algorithm. AERONET = Aerosol Robotic Network; AOD = aerosol optical depth; LUT = look-up table.

AERONET Data

AERONET is an aerosol ground-based observation network with more than 800 sites established worldwide, including more than 50 sites in China. The instruments used at the AERONET site are mainly CE-318 solar photometers, which provide eight band aerosol observations from 340 to 1640 nm. Aerosol optical depth, single scattering albedo, complex refractive exponent, scattering phase function, and aerosol size distribution are recorded every 15 minutes, with an accuracy of 0.01 to 0.02. Four AERONET sites, for which data were used in this study, are located in the urban area of Beijing (Beijing, Beijing_CAMS, Beijing_PKU, and Beijing_RADI). Information on the four sites is shown in Table 1.

Table 1. Beijing Aerosol Robotic Network (AERONET) site information.

Site Name	Coordinate (Latitude, Longitude)	Altitude (m)	Date	Data Level
Beijing	39.997°N, 116.381°E	92	2010–2019	Level 2.0
Beijing_CAMS	39.993°N, 116.317°E	106	2012–2019	Level 1.5
Beijing_PKU	39.992°N, 116.310°E	53	2016–2019	Level 1.5
Beijing_RADI	40.005°N, 116.379°E	59	2010–2019	Level 2.0

Methodology

Extraction of surface reflectance is a critical aspect of AOD retrieval. According to the radiation transmission model, the apparent reflectance can be denoted as a function of aerosol reflectance, Rayleigh reflectance and surface reflectance, as shown in Equation 1 (Kaufman *et al.* 1997):

$$\rho_{TOA}(\theta_s, \theta_v, \phi) = \rho_{Aer}(\theta_s, \theta_v, \phi) + \rho_{Ray}(\theta_s, \theta_v, \phi) + \frac{T(\theta_s)T(\theta_v)\rho_s}{1 - S\rho_s} \quad (1)$$

where $\rho_{TOA}(\theta_s, \theta_v, \phi)$ is the apparent reflectance, $\rho_{Aer}(\theta_s, \theta_v, \phi)$ is the aerosol reflectance, $\rho_{Ray}(\theta_s, \theta_v, \phi)$ is the Rayleigh reflectance, $T(\theta_s)$ is the atmospheric downward transmittance from the sun to the surface path, $T(\theta_v)$ is the atmospheric upward transmittance from the surface to the satellite path, ρ_S is the surface reflectance, S is the hemispherical reflectance of the atmosphere, and θ_s, θ_v, and ϕ are the solar zenith angle, view zenith angle, and relative azimuth angle, respectively.

The flow chart of our algorithm is shown in Figure 2. The fundamental concept of this algorithm is to extract the "cleanest" image from a temporal window based on AERONET ground-based measurements; after atmospheric correction, the surface reflectance database can be constructed for AOD retrieval in advance. The Fmask4.0 algorithm (Zhu *et al.* 2012) is also adopted in this paper for clouds and snow.

Surface Reflectance Database Construction

In contrast to the conventional minimum reflectance technique (Hsu *et al.* 2006), our approach does not determine the "cleanest" image obtained by remote sensing but directly extracts it from the ground-based AERONET AOD data.

Since the *Sentinel-2* constellation has a relatively high temporal resolution in the midlatitude region, the "cleanest" image is readily found with adequate *Sentinel-2* images; furthermore, as the number of images from *Sentinel-2* increases over time, the "cleanest" image will be more representative and have fewer errors (see the analysis below for details). The "cleanest" image corresponds to the smallest aerosol contamination and, therefore, the minimum uncertainty in surface reflectance from atmospheric correction on this basis (Liang *et al.* 2006). Assuming that the surface reflectance of the same date in different years is constant and the surface reflectance is constant for a short continuous period of time, the surface reflectance of the "cleanest" image after accurate atmospheric correction can be used to represent the surface reflectance of the image in the same temporal window.

In this paper, AOD data at 500 nm from two AERONET sites in Beijing were used to determine the "cleanest" image. Figures 3, 4, and 5 show the AOD changes at 500 nm at the Beijing_CAMS and Beijing_PKU AERONET sites in 2017, 2018, and 2019, respectively. Data with an AOD greater than 1 were excluded for the convenience of display and analysis. First, it is readily found from the three figures that the minimum AOD of both sites is approximately 0.05. The lowest AOD values of both

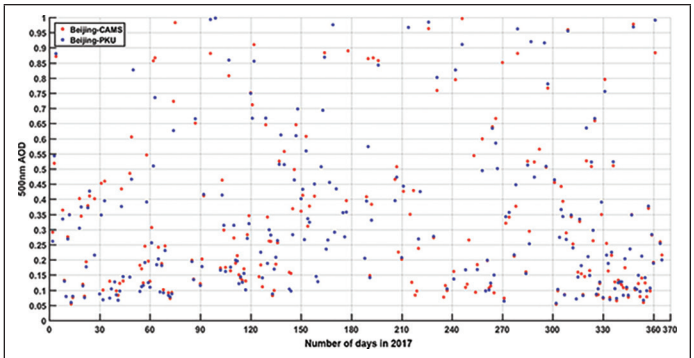

Figure 3. Changes in AOD (500 nm) at two AERONET sites in Beijing in 2017. AOD = aerosol optical depth; AERONET = Aerosol Robotic Network.

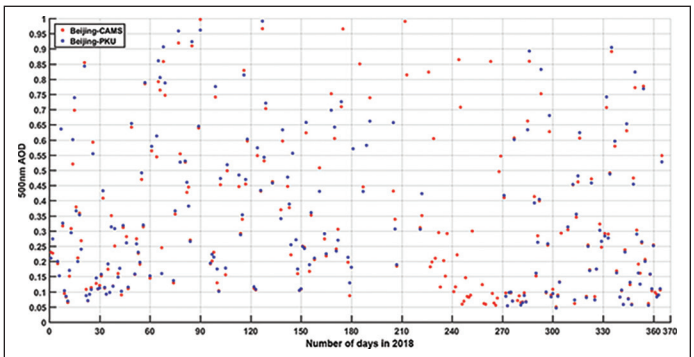

Figure 4. Changes in AOD (500 nm) at two AERONET sites in Beijing in 2018. AOD = aerosol optical depth; AERONET = Aerosol Robotic Network.

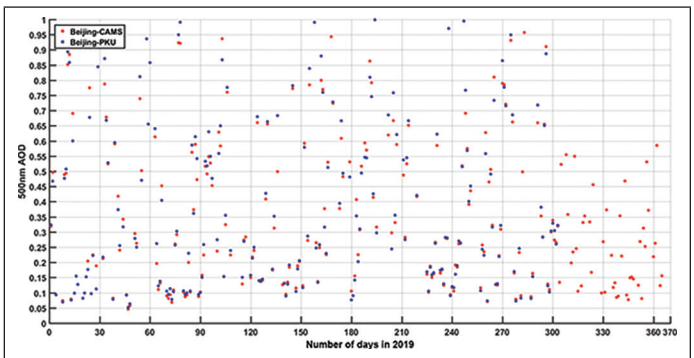

Figure 5. Changes in AOD (500 nm) at two AERONET sites in Beijing in 2019. AOD = aerosol optical depth; AERONET = Aerosol Robotic Network.

sites are concentrated in the range of 0.05–0.1, and the atmosphere is relatively clean when AOD is in this range. Both Beijing_CAMS and Beijing_PKU are located in the downtown area of the city, approximately 6.6 km away from each other. Aerosol distribution in urban areas tends to change at a fine spatial scale due to buildings, traffic distribution and population density (Zhang and Cao 2015; He *et al.* 2016; Chudnovsky *et al.* 2013). However, when the AOD is between 0.05 and 0.1, the AODs of the two sites are almost the same, as shown in Figures 3, 4, and 5. Therefore, on clean days, the AOD distribution is almost homogeneous, and it will not result in substantial errors to use the average AOD of two stations to represent the AOD of the area where it is located.

The size of the temporal window is also an important factor related to the algorithm. First, this temporal window must be short enough because the phenological phenomenon of vegetation and some other human factors will cause surface changes, changing the surface reflectance. The purpose of setting a short temporal window is to ensure that the surface reflectance does not change significantly during this period. On the other hand, the temporal window must also be long enough to ensure that clean images can be found during the window. In this

paper, considering the above factors and referring to previous studies, the temporal window is set to one month (Hsu *et al.* 2004; Wei 20187).

Next, in each one-month temporal window, we needed to identify the "cleanest" image with AOD between 0.05 and 0.1, that is, the image with the smallest AOD. In this study, all *Sentinel-2* images in Beijing in January, February, November, and December 2017 with no clouds or only a small number of clouds were counted, and the "cleanest" images in these four months were found by the above method. The specific date of the images and the corresponding AOD size are shown in Table 2.

The 6SV radiation transmission model was then used to analyze the surface reflectance of the selected images. $\rho_{TOA}acr$ AOD at 550 nm was input into the 6SV radiation transmission model for atmospheric correction. To minimize errors, AERONET AOD data within 20 minutes before and after the collection time of the "cleanest" image was adopted in this study, and the AOD at 550 nm was calculated using the relationship between AOD and wavelength proposed by Eck *et al.* (Eck *et al.* 1999).

Table 2. Cleanest *Sentinel-2* images of Beijing over four months.

Month	Image Date	AOD (500 nm)
January	20190108	0.0618
February	20190217	0.0560
November	20181109	0.0616
December	20171204	0.0652

AOD = aerosol optical depth.

$$\ln \tau(\lambda) = a_0 + a_1 \ln \lambda + a_2 (\ln \lambda)^2 \quad (2)$$

Due to its high sensitivity to aerosols and high spatial resolution, the blue band of *Sentinel-2* was selected in this study. The surface reflectance of the blue band of each month's "cleanest" image formed the surface reflectance database.

The surface reflectances of four specific *Sentinel-2* images of Beijing obtained by the above method are shown in Figure 6. These

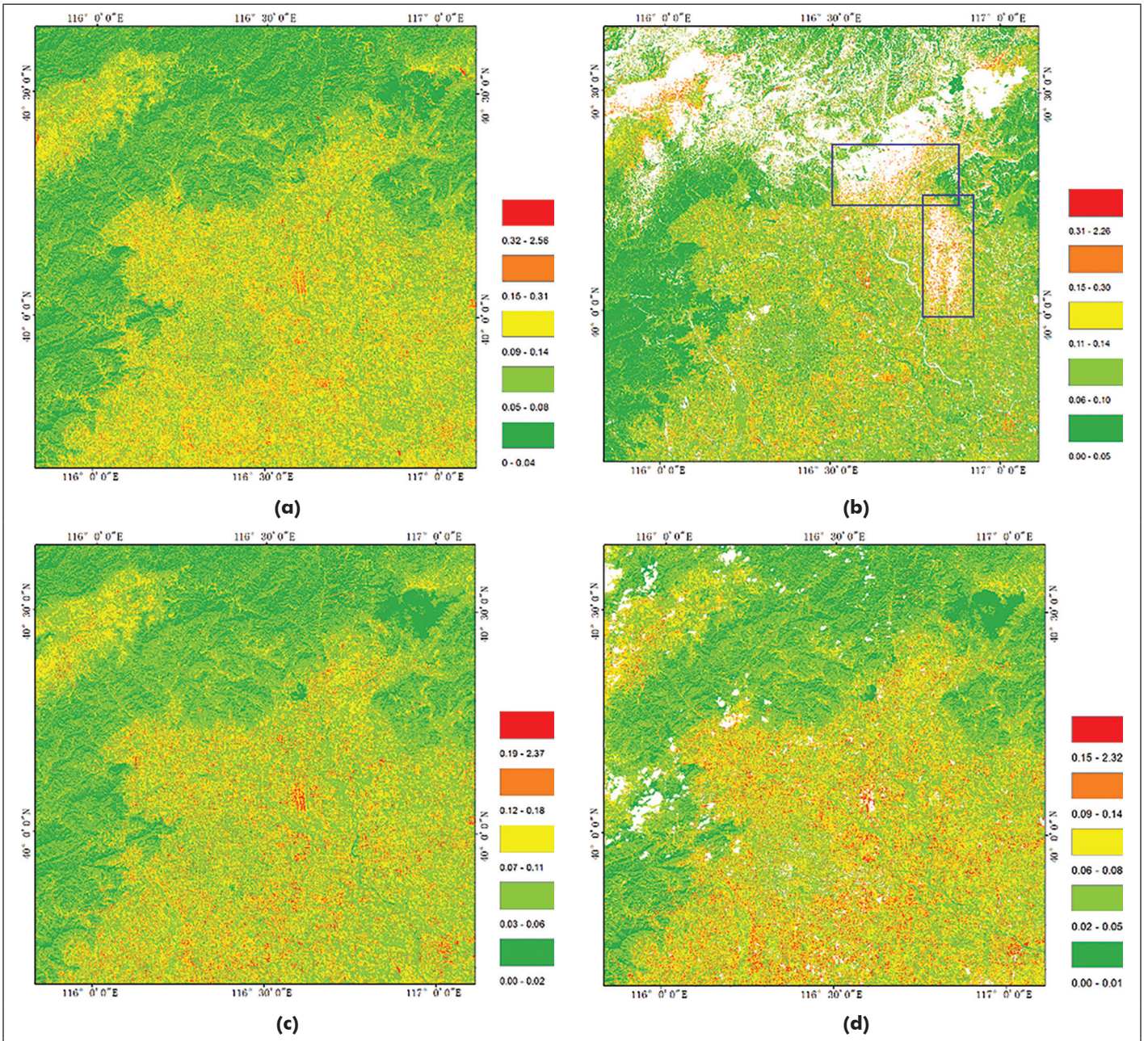

Figure 6. Surface reflectance library in Beijing. (a) 20190108 Sentinel-2 blue band surface reflectance; (b) 20190217 Sentinel-2 blue band surface reflectance; (c) 20181109 Sentinel-2 blue band surface reflectance; (d) 20171204 Sentinel-2 blue band surface reflectance.

four surface reflectance images all well reflect the spatial characteristics in the surface reflectance in the Beijing area. The surface reflectance in the northern and western mountainous areas is significantly lower than that in the urban area of Beijing and the plains around the urban area. Although the surface reflectance of the Beijing urban area and surrounding plains is relatively high, the reflectance of most pixels is less than 0.15, which is consistent with the Beijing surface reflection database constructed by Wei *et al.* using Landsat 4-7 surface reflectance data (Wei *et al.* 2013). The reflectance of a few pixels is higher than 0.15. These pixels are mainly airport runways, light-colored and especially white building surfaces, factory roofs, stadium roofs, bare soil, and the edges of unremoved clouds and snow. The unremoved clouds and snow are the main error source of aerosol retrieval in our algorithm.

Aerosol Type Determination

Different aerosol types differ significantly in origin, size, component, and composition, and thus, their optical properties are heterogeneous in space and time. The study of Li *et al.* also shows that aerosols in China are complex and vary significantly in both time and space (Li *et al.* 2018).

In some studies, aerosol types are divided by season (Wei *et al.* 2013; Levy *et al.* 2013; Wei *et al.* 2019). In this paper, the monthly mean data of the single scattering albedo and complex refractive index of two AERONET sites in Beijing from 2010 to 2019 were analyzed, and significant changes between months occur (see Figure 7 and Figure 8). Thus, to improve the retrieval accuracy, the aerosol types were divided by month in this study.

To further determine the type of aerosol in Beijing, the aerosol particle spectrum distribution data from 2017 to 2019 of two AERONET sites in Beijing were analyzed, and the results are shown in Figure 9. From Figure 9, it can be seen that although the spectral distribution of the aerosol particles differs from year to year and month to month in terms of the division radius of the coarse and fine modal particles and the peak of the spectral distribution, they are all consistent with the characteristics of a bimodal normal-type distribution. Therefore, in this study, a bimodal lognormal spectral distribution was used to characterize aerosol types in Beijing, as shown in Equation 3 (Omar *et al.* 2005).

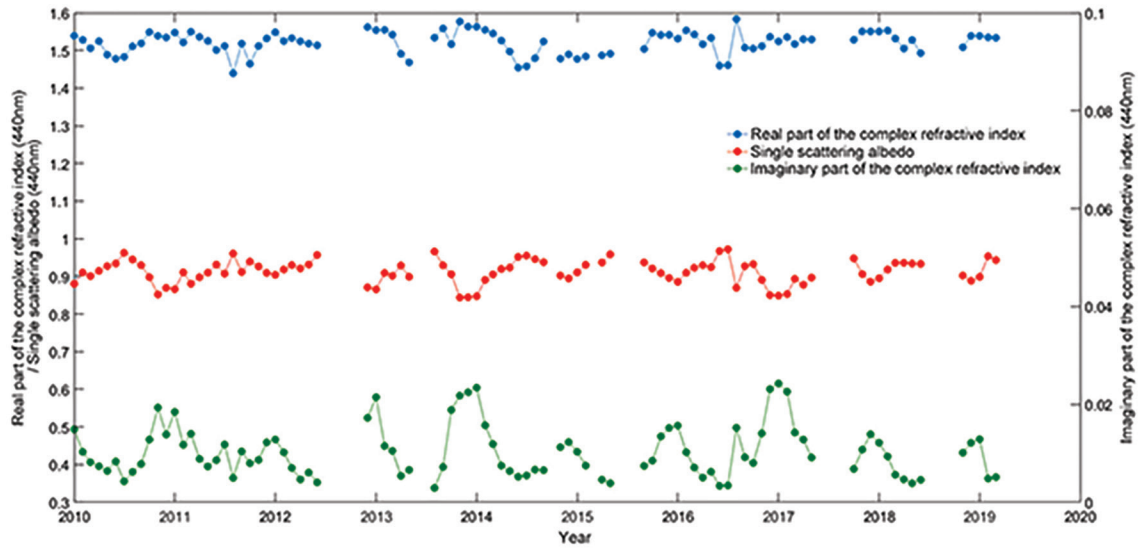

Figure 7. Variation in aerosol optical parameters at the Beijing site.

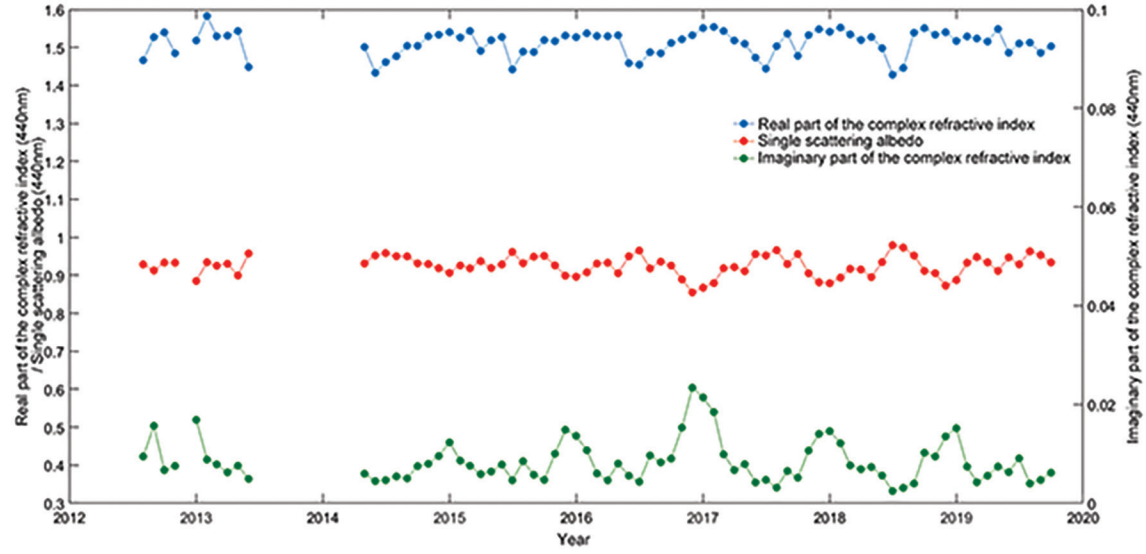

Figure 8. Variation in aerosol optical parameters at the Beijing_CAMS site.

$$\frac{dN(r)}{d\ln r} = \sum_{i=1}^{2} \frac{N_i}{\sqrt{2\pi}\ln\sigma_i} \exp\left[-\frac{(\ln r - \ln r_{m,i})^2}{2(\ln\sigma_i)^2}\right] \quad (3)$$

where N is the number of particles per unit volume, r is the particle radius, r_m is the average radius of the particles, and σ is the standard deviation of the radius.

Li *et al.* calculated the optical, physical, chemical and radiation characteristic parameters of aerosols in 16 Chinese cities by analyzing long-term observation data from SONET (Li *et al.* 2018). Given their results, the monthly average data of four AERONET sites in Beijing from 2010 to 2019 were used to calculate the monthly average of the complex refraction index to determine the aerosol type parameters. The parameters of aerosol types by month are shown in Table 3.

Results

Evaluation Method and Index

To validate the AOD retrievals, AOD data from four AERONET sites located in the urban area of Beijing (Beijing, Beijing_CAMS, Beijing_PKU, and Beijing_RADI) were acquired. The AOD value of AERONET was converted to 550 nm to ensure band consistency since the wavelength of the satellite-retrieved AOD value was 550 nm (Equation 2).

In this paper, the expected error (EE, Equation 4) (Hsu *et al.* 2013), the root-mean-square error (RMSE, Equation 5), the mean absolute error (MAE, Equation 6), and the relative mean bias (RMB, Equation 7) were used to quantitatively evaluate the accuracy and uncertainty of the AOD result. The definitions of the evaluation indicators are as follows:

$$EE = \pm (0.05 + 0.20 * AOD_{AERONET}) \quad (4)$$

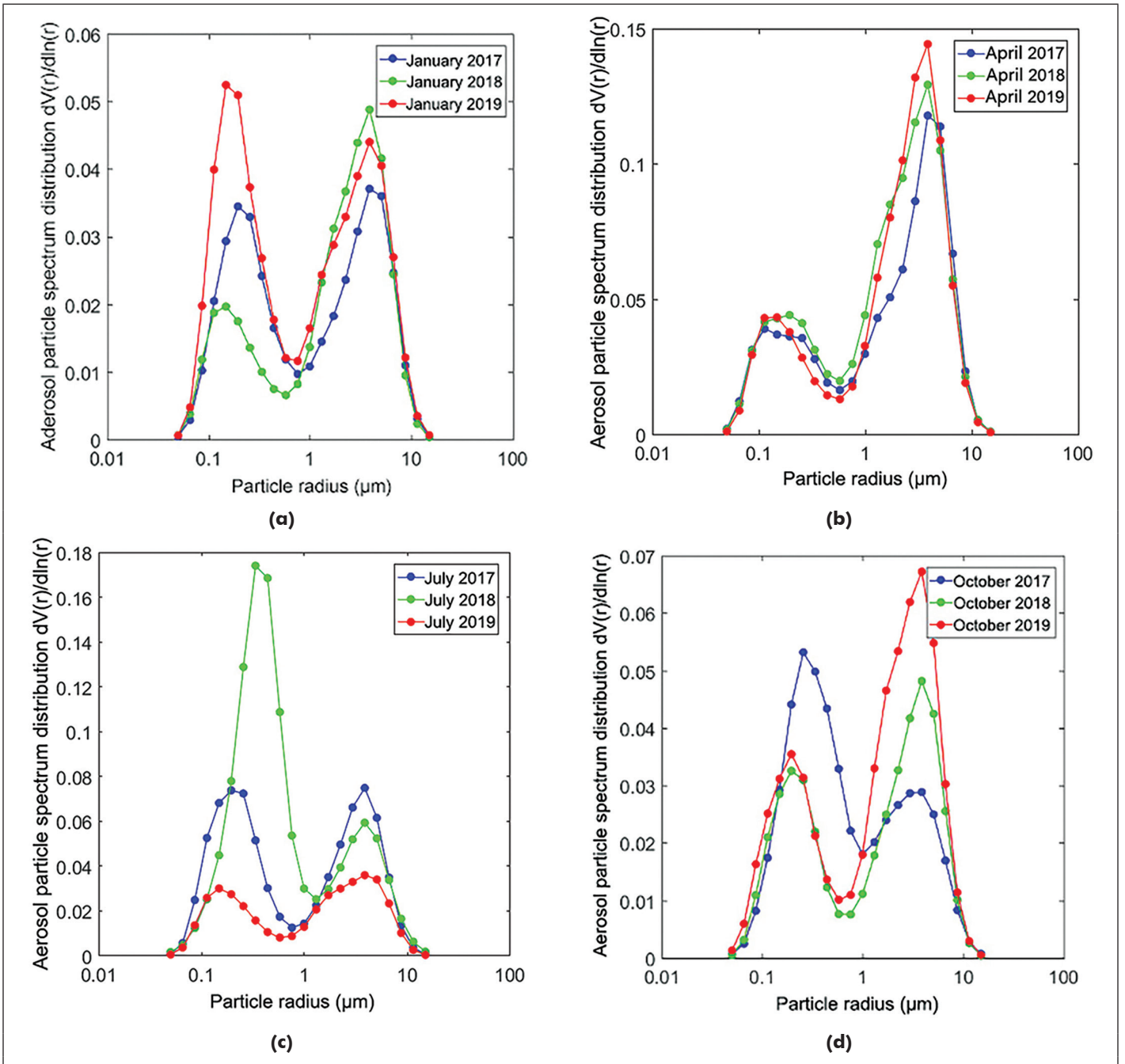

Figure 9. Beijing aerosol spectrum distribution. (a) January spectrum distribution; (b) April spectrum distribution; (c) July spectrum distribution; (d) October spectrum distribution.

Table 3. Aerosol type parameters for 12 months in Beijing.

Aerosol Models	Parameters							
	r_f	σ_f	V_f	r_c	σ_c	V_c	RP-CRI (0.44/0.675 μm)	IP-CRI (0.44/0.675 μm)
January	0.15	0.53	0.07	3.18	0.64	0.08	1.532/1.535	0.016/0.012
February	0.15	0.50	0.07	2.97	0.67	0.08	1.547/1.553	0.011/0.009
March	0.14	0.49	0.08	2.89	0.66	0.18	1.534/1.541	0.007/0.005
April	0.15	0.49	0.07	2.81	0.66	0.21	1.517/1.530	0.006/0.004
May	0.15	0.48	0.08	2.89	0.66	0.20	1.526/1.542	0.007/0.006
June	0.18	0.49	0.11	3.13	0.63	0.09	1.475/1.487	0.005/0.006
July	0.21	0.53	0.16	3.19	0.60	0.07	1.457/1.456	0.005/0.005
August	0.19	0.50	0.10	3.18	0.60	0.06	1.483/1.485	0.006/0.007
September	0.17	0.48	0.09	3.07	0.63	0.07	1.509/1.516	0.007/0.008
October	0.17	0.49	0.10	3.00	0.63	0.10	1.515/1.518	0.007/0.006
November	0.14	0.50	0.07	2.97	0.65	0.08	1.519/1.530	0.010/0.008
December	0.14	0.51	0.05	3.24	0.63	0.08	1.537/1.550	0.015/0.012

RP-CRI = real part (RP) of complex refractive index (CRI); IP-CRI = imaginary part (IP) of complex refractive index (CRI).

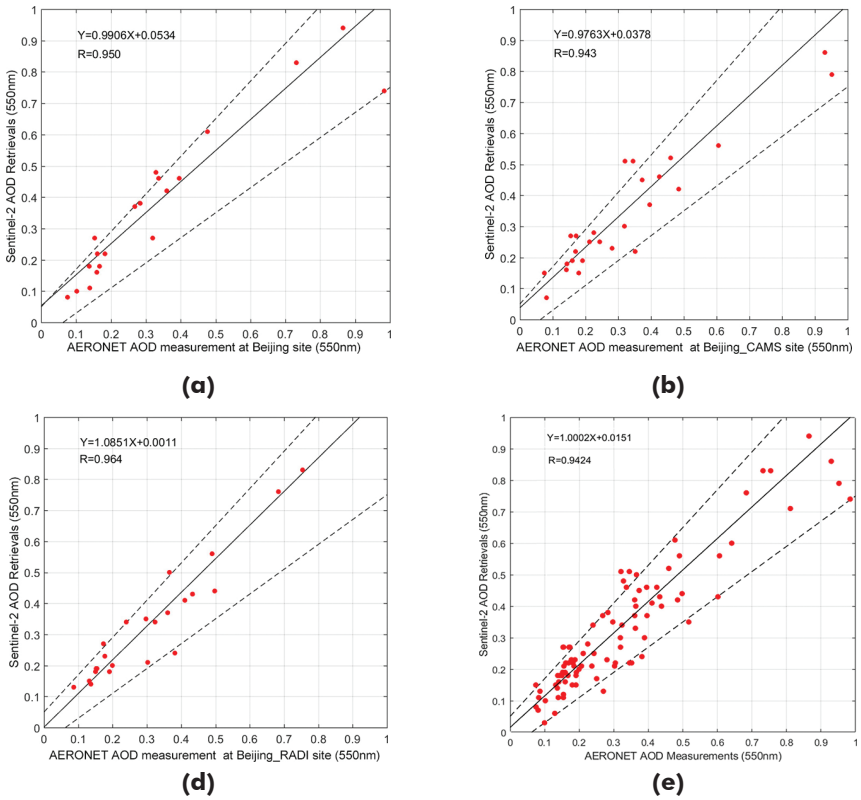

Figure 10. Validation of Sentinel-2 AOD retrievals against AERONET AOD measurements at different sites. (a) Beijing site; (b) Beijing_CAMS site; (c) Beijing_PKU site; (d) Beijing_RADI site; (e) all the sites. AERONET = Aerosol Robotic Network; AOD = aerosol optical depth.

$$\mathrm{RMSE} = \sqrt{\frac{1}{n}\sum_{i=1}^{n}\left(\mathrm{AOD}^{i}_{\mathrm{Retrieval}} - \mathrm{AOD}^{i}_{\mathrm{AERONET}}\right)^{2}} \quad (5)$$

$$\mathrm{MAE} = \frac{1}{n}\sum_{i=1}^{n}\left|\mathrm{AOD}^{i}_{\mathrm{Retrieval}} - \mathrm{AOD}^{i}_{\mathrm{AERONET}}\right| \quad (6)$$

$$\mathrm{RMB} = \frac{1}{n}\sum_{i=1}^{n}\left(\mathrm{AOD}^{i}_{\mathrm{Retrieval}} / \mathrm{AOD}^{i}_{\mathrm{AERONET}}\right) \quad (7)$$

n in the formula is the number of data sets for comparison.

Validation against AERONET AOD Measurements

There are a total of 97 sets of experimental data, including 21 sets of data from the Beijing site, 28 sets of data from the Beijing_CAMS site, 24 sets of data from the Beijing_PKU site, and 24 sets of data from the Beijing_RADI site. Figure 10 and Table 4 present the results of the comparative validation of the AOD from the *Sentinel-2* data retrieval and the AOD measurements from the four AERONET sites. The solid and dashed lines in Figure 10 represent the linear fitting regression lines and EE error lines, respectively. The correlations between the AOD retrieval results and the AOD measurement values are all the

Table 4. Validation of *Sentinel-2* AOD retrievals against AERONET AOD measurements at different sites.

Site	R	MAE	RMSE	RMB	Within EE (%)	Above EE (%)	Below EE (%)
Beijing	0.950	0.081	0.102	1.178	85.72	14.28	0.00
Beijing_CAMS	0.943	0.073	0.095	1.147	78.57	17.86	3.57
Beijing_PKU	0.955	0.067	0.081	0.852	87.50	0.00	12.50
Beijing_RADI	0.964	0.055	0.072	1.121	83.38	12.50	4.12
All sites	0.942	0.069	0.088	1.074	85.56	8.25	6.19

AERONET = Aerosol Robotic Network; AOD = aerosol optical depth; MAE = mean absolute error; RMSE = root-mean-square error; RMB = relative mean bias; EE = expected error.

most significant, with coefficients of 0.950, 0.943, 0.955, and 0.964, respectively. All the sites' MAEs and RMSEs are very small, indicating a small error. Furthermore, the retrieval results at the Beijing_PKU site are underestimated, while the others are overestimated.

In addition, 85.72%, 78.57%, 87.50%, and 83.38% of the retrieval results of the four sites fall into the EE error range, indicating that most of the retrieval results are acceptable.

Figure 10e highlights the verification results of all *Sentinel-2* AOD retrieval results and AERONET AOD measurement values. The correlation coefficient between all retrieval results and AERONET's AOD measurement value is 0.9424, which is the most significant. Approximately 85.56% of the values fall within the EE envelope with small MAE and RMSE errors of 0.0688 and 0.0882, respectively.

These results indicate that the surface reflectance estimation method and the AOD retrieval algorithm based on the surface reflectance database proposed in this paper can more accurately retrieve aerosols in urban areas and largely overcome the challenges related to AOD retrieval caused by the higher surface reflectance in urban areas.

Spatial Distribution of AOD Retrieval

Figure 11 shows the four *Sentinel-2* RGB color images of Beijing and their corresponding AOD distribution, in which the blank area is the cloud mask and snow mask. As seen from Figure 11, the AOD retrieval algorithm proposed in this paper can not only obtain a continuous distribution of AOD in mountainous areas with small surface reflectance as well as the conventional algorithm but also has almost no gaps in urban areas.

From these four AOD distribution maps, it can be seen that the AOD in the northern and western mountainous areas of Beijing is relatively small overall. Mountainous areas have more vegetation, less people, and less natural pollution. Moreover, mountains can prevent the diffusion of atmospheric pollutants. In contrast, the AOD of the urban areas in southern and eastern Beijing and the plain area around the city are large overall, mainly because the city and its surrounding areas have a large amount of industrial exhaust gas, traffic exhaust gas, and exhaust gas generated by humans. The above conclusions are consistent with those of other studies (Wei *et al.* 2013; Luo *et al.* 2015; Tian *et al.* 2018).

In addition, the results obtained during the four different time periods also show the air pollution patterns in Beijing. As seen in Figure 11b, on January 13, 2018, the air pollution in the Beijing downtown area was low, and the pollution was mainly concentrated in the southeastern corner. In Xianghe County, Hebei Province; as seen in Figure 11d, on February 27, 2019, the overall pollution of Beijing was more severe than that in other areas. Not only was the main urban area heavily polluted, but the Changping District to its north also showed higher air pollution levels. In addition, a south-to-north pollution corridor was clearly visible. On 24 November 2018, Beijing's air pollution was mainly concentrated in Daxing District to its south, with the downtown area also heavily affected, but the northern districts of Changping and Shunyi were unaffected and had good air quality (see Figure 11f). On 19 December 2017, Beijing's overall air quality was good (see Figure 11h).

From the above analysis, it can be seen that the AOD retrieval algorithm based on the surface reflectance database proposed in this paper can perform aerosol retrieval from *Sentinel-2* data with good results; moreover, due to the relatively high resolution (100 m), the results reflect the aerosol distribution changes with clear details, which will be helpful for future studies on the traceability of air pollution sources.

However, it should be noted that due to the defects of the cloud and snow detection algorithm, there are missed detections of thin clouds, thin snow, and water edges in the images, resulting in anomalously large or small areas in the retrieval results, such as the anomalously large area caused by thin clouds and thin ice at the edges of water bodies in Figure 11b (blue box part of the figure) and the anomalously large area caused by thin ice at the edges of water bodies in Figure 11h (blue box part of the figure). The blue box in Figure 11h shows the region of a small AOD anomaly, which is caused by large surface reflectance in this region, which was affected by thin snow during the construction of the surface reflectance database, thus indicating the importance of the accuracy of the surface reflectance database to the later retrieval. These issues will be analyzed and addressed in subsequent research.

Discussion

Beijing is a hot spot for aerosol inversion, and there are many aerosol remote sensing inversion and validation studies in the Beijing area. He *et al.* retrieved the AOD in the Beijing area by simulating the relationship between apparent reflectance and AOD in MODIS bands, and the average correlation coefficient with AERONET was 0.746 (He *et al.* 2014). Tian *et al.* validated the MODIS C6.1 and C6 aerosol products in Beijing from 2002-2016 using AERONET site data, with an average correlation of 0.92 and an average RMSE of 0.24 (Tian *et al.* 2018). Wei *et al.* used MODIS surface reflectance and aerosol products to construct an 8-day surface reflectance database on land and a seasonal aerosol type database and proposed an improved aerosol inversion algorithm for MODIS data, and the validation results showed that its correlation with AERONET was 0.943 and its RMSE was 0.138 (Wei *et al.* 2018). Wang *et al.*, based on the assumption that the reflection ratio between the red and 2.12 μm bands is invariant, retrieved the AOD of the Beijing-Tianjin-Hebei region based on MODIS data, which had a high correlation with AERONET ($R > 0.9$) and an RMSE of 0.15, with approximately 77% of the points within the expected error (Wang *et al.* 2019). In the aforementioned AOD results based on MODIS data in the Beijing area, compared with the algorithm in this paper, the correlation with AERONET is usually less or similar, and the RMSE is usually greater than the results in this paper, which may be related to the large scale of MODIS, leading to a large-scale effect when compared with that from ground stations. Based on the concept of cleanest image pixels, Liang *et al.* proposed an algorithm to determine the cleanest observation of each MODIS image pixel within a time window (Liang *et al.* 2006). The results of the comparison and validation with AERONET show that the correlation coefficient is 0.96, which is much higher than 0.44 for the MOD04 product. The correlation between this algorithm and AERONET is slightly higher than ours. However, under the condition of small AOD (AOD ϵ [0,1]), the algorithm inversion results show a larger decrease in the correlation with AERONET.

Several studies have also conducted remote sensing retrieval studies of aerosols in the Beijing area using relatively higher resolution data such as Landsat, *Sentinel-2*, and HJ-1. Li *et al.* obtained a 100 m resolution aerosol distribution in the Beijing area by synergetic use of HJ-1 CCD and MODIS data. The validation results show that the correlation with AERONET is 0.89 and the RMSE is 0.24 (Li *et al.* 2011). Based on the assumptions of a constant blue–red surface reflectance ratio and constant bright target surface reflectance in the short term, Yang *et al.* obtained the 60-m resolution aerosol distribution in the Beijing area based on *Sentinel-2* data. The cross-validation results show that its correlation with the AERONET site is 0.927 on average, the RMSE is 0.104, and the value falling within the EE is 77.31% (Yang *et al.* 2022). Chen *et al.* proposed the multispectrum hierarchical segmentation (MSHS) algorithm and carried out an aerosol inversion study in Beijing based on this algorithm, and the results show that its correlation with AERONET ground observations is 0.871 and the RMSE is 0.148 (Chen *et al.* 2022). It can be seen that compared with those of the previous study, the results of this paper are very similar in terms of accuracy and have an improved RMSE. Tian *et al.* proposed using MODIS Bidirectional Reflectance Distribution Function (BRDF) data to assist Landsat-8 aerosol inversion, and their inversion results correlated with AERONET at 0.987 with an RMSE of 0.07, showing high accuracy and low error (Tian *et al.* 2018). The present algorithm assumes that the surface is a Lambertian body, and BRDF is not considered. Whether the text algorithm can be applied to *Sentinel-2* data and further improve the accuracy of this algorithm is subject to further study in the future.

Conclusion

In this study, taking advantage of the short revisit cycle of *Sentinel-2*, a surface reflectance estimation method based on the "cleanest period"

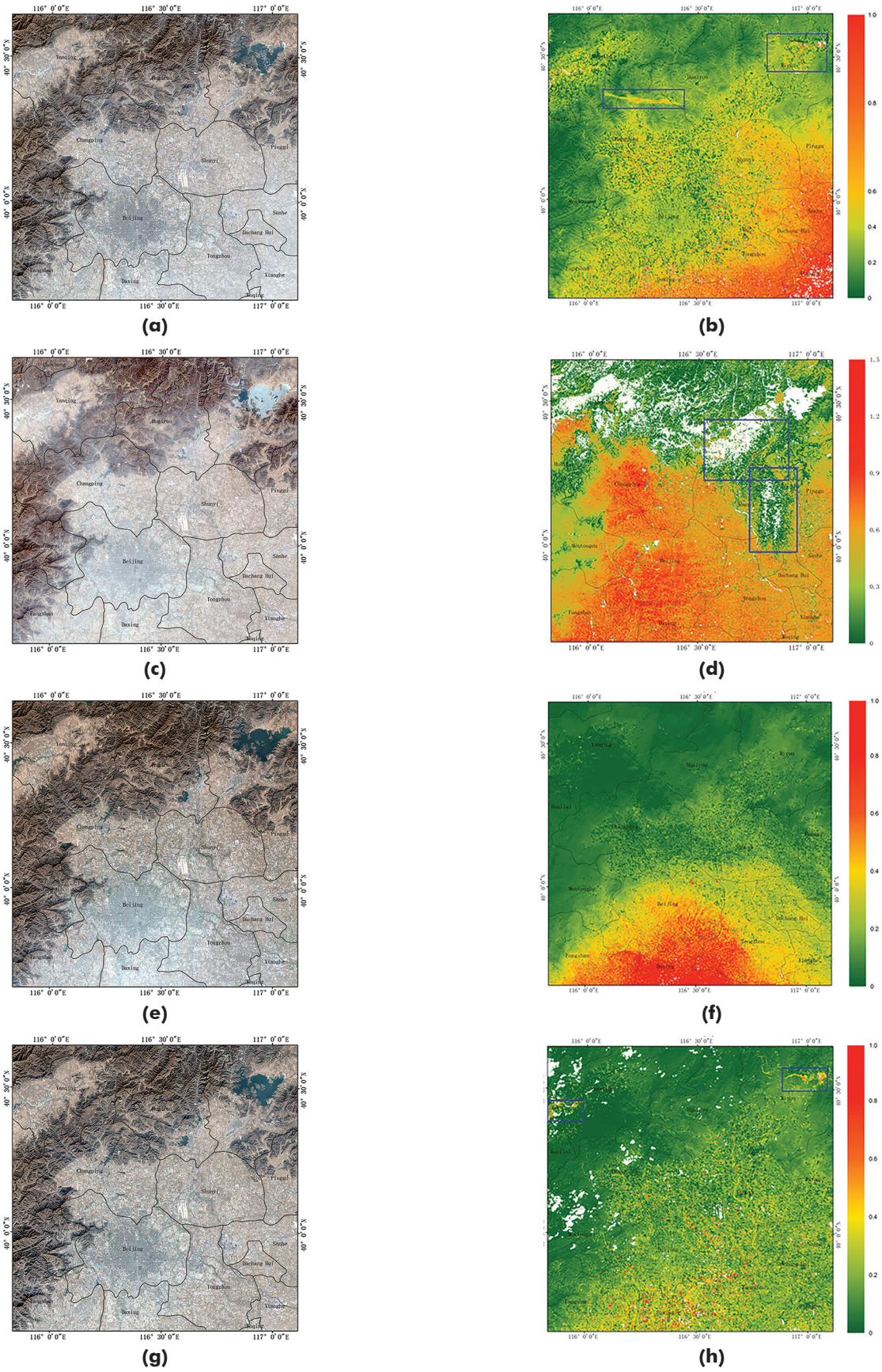

Figure 11. True-color (red-green-blue (RGB)) image and corresponding spatial distribution of Sentinel-2 AOD retrieval in Beijing. (a) 20180113 Sentinel-2 RGB color image; (b) 20180113 AOD distribution map; (c) 20190227 Sentinel-2 RGB color image; (d) 20190227 AOD distribution map; (e) 20181124 Sentinel-2 RGB color image; (f) 20181124 AOD distribution map; (g) 20171219 Sentinel-2 RGB color image; (h) 20171219 AOD distribution. AOD = aerosol optical depth.

is proposed. This method determines the "cleanest" image in the temporal window of one month through the AERONET AOD data from a long time series and then obtains the surface reflectance by accurate atmospheric correction. The surface reflectance image corresponding to the "cleanest" image constitutes the surface reflectance database. In the aerosol retrieval, the image to be retrieved and the surface reflectance image from the same month in the surface reflectance database are used for retrieval. This method can minimize the uncertainty of surface reflectance estimation and is applicable to both dark surfaces with low reflectance and bright surfaces with high reflectance. AOD products with 100 m resolutions were obtained using *Sentinel-2* data to perform AOD retrieval in the Beijing area. The AODNET measurement results were used to verify the AOD retrieval results in this study. The results show that the AOD retrieval results in this study are highly correlated with the AOD measurements at four AERONET sites in Beijing. The correlation coefficients are 0.950, 0.943, 0.955, and 0.964, and 85.72%, 78.57%, 87.50%, and 83.38% of the retrieval results of the four sites fall within the expected error range. The results of the MAE and RMSE also indicate that the AOD retrieval results of this study have a small error in terms of the AOD measurement value of the AERONET site. Thus, the AOD retrieval algorithm based on the surface reflectance library proposed in this study has high retrieval accuracy. In addition, the algorithm proposed in this study can well characterize the fine spatial-resolution changes in aerosol distribution, and the details of the urban areas are very clear, which will be helpful for air pollution source identification. These results indicate that the AOD retrieval algorithm proposed in this study can retrieve high-spatial-resolution AOD in urban areas, which is meaningful for aerosol research and refined air quality monitoring. However, in large cities, surface inhomogeneity is a problem, and seasonal changes in vegetation growth and death phases can also have an impact on the surface BRDF. Not considering this issue has introduced some errors in our results in this paper. In the future, more studies should be conducted in this area.

Acknowledgments

This work is supported by the National Civil Space Infrastructure Land Observation Satellite Common Application Support Platform (No. Y930280A2F) and the Sichuan Science and Technology Plan Project (No. 2019YJ0201).

References

Bai, L., Y. Xue, J. Guang, Y. Wang, Y. Li and W. Wan. 2008. Regional quantitative retrieval of aerosol optical depth using terra and aqua MODIS data. Pages III-939–III-942 in *Proceedings IEEE International Geoscience & Remote Sensing Symposium*, held in Boston, MA. https://doi.org/10.1109/IGARSS.2008.4779505.

Bilal, M. and Z. Qiu. 2018. Aerosol retrievals over bright urban surfaces using Landsat 8 images. Pages 7560–7563 in *Proceedings 2018 IEEE International Geoscience and Remote Sensing Symposium*, held in Valencia, Spain. https://doi.org/10.1109/IGARSS.2018.8517427.

Chen, Y., W. Han, S. Chen, and L. Tong. 2014. Estimating ground-level PM2. 5 concentration using Landsat 8 in Chengdu, China. *Remote Sensing of the Atmosphere, Clouds, and Precipitation V. International Society for Optics and Photonics*. https://doi.org/10.1117/12.2068886.

Chen, Y., Y. Yang, Y. Xiong, and Y. Sun. 2022. Multi-spectrum hierarchical segmentation algorithm: A new aerosol optical thickness retrieval algorithm for urban areas. *IEEE Geoscience and Remote Sensing Letters* 19:1–5.

Chudnovsky, A. A., A. Kostinski, A. Lyapustin, and P. Koutrakis. 2013. Spatial scales of pollution from variable resolution satellite imaging. *Environmental Pollution* 172:131–138.

Eck, T. F., B. N. Holben, J. S. Reid, O. Dubovik, A. Smirnov, N. T. O'Neill, I. Slutsker, and S. Harmel, T., M. Chami, T. Tormos, N. Reynaud, and P.-A. Danis. 2018. Sunglint correction of the Multi-Spectral Instrument (MSI)-SENTINEL-2 imagery over inland and sea waters from SWIR bands. *Remote Sensing of Environment* 204:308–321.

He, J., L. Wu, H. Mao, H. Liu, B. Jing, Y. Yu, P. Ren, C. Feng, and X. Liu. 2016. Development of a vehicle emission inventory with high temporal-spatial resolution based on NRT traffic data and its impact on air pollution in Beijing—Part 2: Impact of vehicle emission on urban air quality. *Atmospheric Chemistry and Physics* 15(13):19239–19273.

He, J., Y. Zha, J. Zhang, and J. Gao. 2014. Aerosol indices derived from MODIS data for indicating aerosol-induced air pollution. *Remote Sensing* 6:1587–1604.

Hou, W., J. Wang, X. Xu, J. S. Reid, S. J. Janz, and J. W. Leitch. 2020. An algorithm for hyperspectral remote sensing of aerosols: 3. Application to the GEO-TASO data in KORUS-AQ field campaign. *Journal of Quantitative Spectroscopy & Radiative Transfer* 253:107161.

Hsu, N. C., J. Lee, A. M. Sayer, N. Carletta, S.-H. Chen, C. J. Tucker, B. N. Holben, and S.-C. Tsay. 2013. Enhanced Deep Blue aerosol retrieval algorithm: The second generation. *Journal of Geophysical Research: Atmospheres* 118(16). https://doi.org/10.1002/jgrd.50712.

Hsu, N. C., S.-C. Tsay, M. D. King, and J. R. Herman. 2004. Aerosol properties over bright-reflecting source regions. *IEEE Transactions on Geoscience and Remote Sensing* 42:557–569.

Hsu, N. C., S.-C. Tsay, M. D. King, and J. R. Herman. 2006. Deep blue retrievals of Asian aerosol properties during ACE-Asia. *IEEE Transactions on Geoscience and Remote Sensing* 44(11):3180–3195.

Islam, K. M. A., M. S. G. Adnan, K. E. Zannat, and A. Dewan. 2022. Spatiotemporal dynamics of NO2 concentration with linear mixed models: A Bangladesh case study. *Physics and Chemistry of the Earth, Parts A/B/C*. https://doi.org/10.1016/j.pce.2022.103119.

Kaufman, Y. J., A. E. Wald, L. A. Remer, Bo-Cai Gao, Rong-Rong Li, and L. Flynn. 1997. The MODIS 2.1-μm channel-correlation with visible reflectance for use in remote sensing of aerosol. *IEEE Transactions on Geoscience and Remote Sensing* 35:1286–1298.

Kaufman, Y. J., D. Tanré, L. A. Remer, E. F. Vermote, A. Chu, and B. N. Holben. 1997. Operational remote sensing of tropospheric aerosol over land from EOS moderate resolution imaging spectroradiometer. *Journal of Geophysical Research* 102:17051–17067.

Kinne. 1999. Wavelength dependence of the optical depth of biomass burning, urban, and desert dust aerosols. *Journal of Geophysical Research: Atmospheres* 104(D24):31333–31349.

Levy, R. C., S. Mattoo, L. A. Munchak, L. A. Remer, A. M. Sayer, F. Patadia, and N. C. Hsu. 2013. The Collection 6 MODIS aerosol products over land and ocean. *Atmospheric Measurement Techniques* 6(11):2989–3034.

Li, J. and D.P. Roy. 2017. A global analysis of Sentinel-2A, Sentinel-2B and Landsat-8 data revisit intervals and implications for terrestrial monitoring. *Remote Sensing* 9(9):902.

Li, Y., Y. Xue, X. He, and J. Guang. 2011. High-resolution aerosol remote sensing retrieval over urban areas by synergetic use of HJ-1 CCD and MODIS data. *Atmospheric Environment* 46:173–180.

Li, Z., D. P. Roy, H. K. Zhang, E. F. Vermote, and H. Huang. 2019. Evaluation of Landsat-8 and Sentinel-2A aerosol optical depth retrievals across Chinese cities and implications for medium spatial resolution urban aerosol monitoring. *Remote Sensing* 11(2):122.

Li, Z., H. Xu, K. T. Li, D. H. Li, Y. S. Xie, L. Li, Y. Zhang, X. F. Gu, W. Zhao, Q. J. Tian, R. R. Deng, X. L. Su, B. Huang, Y. L. Qiao, W. Y. Cui, Y. Hu, C. L. Gong, Y. Q. Wang, X. F. Wang, J. P. Wang, W. B. Du, Z. Q. Pan, Z. Z. Li, and D. Bu. 2018. Comprehensive study of optical, physical, chemical, and radiative properties of total columnar atmospheric aerosols over China: An overview of sun–sky radiometer observation network (SONET) measurements, B. *Bulletin of the American Meteorological Society* 99(4):739–756.

Liang, S., B. Zhong, and H. Fang. 2006. Improved estimation of aerosol optical depth from MODIS imagery over land surfaces. *Remote Sensing of Environment* 104(4):416–425.

Luo, N., M. S. Wong, W. Zhao, X. Yan, and F. Xiao. 2015. Improved aerosol retrieval algorithm using Landsat images and its application for PM10 monitoring over urban areas. *Atmospheric Research* 153:264–275. https://doi.org/10.1016/j.atmosres.2014.08.012.

Mazlan, N. A., N. A. M. Zaki, R. H. Narashid, N. Talib, J. Manokaran, F. C. Arshad, S. S. M. Fauzi, N. C. Dom, M. Valipour, R. Dambul, and S. Blenkinsop. 2023. COVID-19 restriction movement control order (MCO) impacted emissions of peninsular Malaysia using Sentinel-2a and Sentinel-5p satellite. *Earth Systems and Environment* 7(1):347–358.

Olivier, H., M. Huc, D. V. Pascual, and G. Dedieu. 2015. A multi-temporal and multi-spectral method to estimate aerosol optical thickness over land, for the atmospheric correction of FormoSat-2, LandSat, VENS and Sentinel-2 images. *Remote Sensing* 7(3):2668–2691. https://doi.org/10.3390/rs70302668.

Omar, A. H., J.-G. Won, D. M. Winker, S.-C. Yoon, O. Dubovik, and M. P. McCormick. 2005. Development of global aerosol models using cluster analysis of Aerosol Robotic Network (AERONET) measurements. *Journal of Geophysical Research*, *Atmospheres* 110(10). https://doi.org/10.1029/2004JD004874.

Omari, K., A. Abuelgasim, and K.J.A.P.R. Alhebsi. 2019. Aerosol optical depth retrieval over the city of Abu Dhabi, United Arab Emirates (UAE) using Landsat-8 OLI images. *Atmospheric Pollution Research* 10(4):1075–1083. https://doi.org/10.1016/j.apr.2019.01.015.

Shirangi, A., T. Lin, I. Iva′nova′, G. Yun, G. J. Williamson, P. Franklin, L. Jian, R. Burch, A. Dewan, B. Santos, N. Eaton, and J. Xiao. 2022. Exposure to fine particulate matter (PM2.5) during landscape fire events and the risk of cardiorespiratory emergency department attendances: a time-series study in Perth, Western Australia. *Journal of Epidemiology & Community Health* 76:809–818.

Singh, D., N. Kundu, and S. Ghosh. 2021. Mapping rice residues burning and generated pollutants using Sentinel-2 data over northern part of India. *Remote Sensing Applications: Society and Environment* 22:100486.

Spoto, F., O. Sy, P. Laberinti, P. Martimort, V. Fernandez, O. Colin, B. Hoersch, and A. Meygret. 2012. Overview of Sentinel-2. Pages 1707–1710 in *IEEE International Geoscience and Remote Sensing Symposium*, held in Munich, Germany. https://doi.org/10.1109/IGARSS.2012.6351195.

Tian, X., Q. Liu, X. Li, and J. Wei. 2018. Validation and comparison of MODIS C6.1 and C6 aerosol products over Beijing, China. *Remote Sensing* 10:2021.

Tian, X., Q. Liu, Z. Song, B. Dou, and X. Li. 2018. Aerosol optical depth retrieval from Landsat 8 OLI images over urban areas supported by MODIS BRDF/Albedo data. *IEEE Geoscience and Remote Sensing Letters* 15:976–980.

Wang, Z., P. Ma, H. Chen, Y. Zhang, L. Zhang, S. Li, Q. Li, and L. Chen. 2019. Aerosol retrieval in the autumn and winter from the red and 2.12~μm bands of MODIS. *IEEE Transactions on Geoscience and Remote Sensing* 57:2372–2380.

Wei, J., B. Huang, L. Sun, Z. Zhang, L. Wang, and M. Bilal. 2017. A simple and universal aerosol retrieval algorithm for Landsat series images over complex surfaces. *Journal of Geophysical Research (Atmospheres)* 122(24):13, 338–13, 355. https://doi.org/10.1002/2017JD026922.

Wei, J., B. Huang, L. Sun, Z. Zhang, L. Wang, and M. Bilal. 2018. An improved high-spatial-resolution aerosol retrieval algorithm for MODIS images over land. *Journal of Geophysical Research: Atmospheres* 123:12291–12307.

Wei, J. and L. Sun. 2017. Comparison and evaluation of different MODIS aerosol optical depth products over the Beijing-Tianjin-Hebei Region in China. *IEEE Journal of Selected Topics in Applied Earth Observations and Remote Sensing* 10(3):835–844.

Wei, J., Z. Li, Y. Peng, L. Sun, and X. Yan. 2019. A regionally robust high-spatial-resolution aerosol retrieval algorithm for MODIS images over Eastern China. *IEEE Transactions on Geoscience and Remote Sensing* 57(7):4748–4757.

Xiong, Y., Y. Chen, W. Han, and L. Tong. 2016. A new aerosol retrieval algorithm based on statistical segmentation using Landsat-8 OLI data. Pages 4059–4062 in *Proceedings Geoscience & Remote Sensing Symposium*, held in Beijing, China. https://doi.org/10.1109/IGARSS.2016.7730056.

Yang, Y., K. Yang, and Y. Chen. 2022. Aerosol retrieval algorithm for Sentinel-2 images over complex urban areas. *IEEE Transactions on Geoscience and Remote Sensing* PP:1–1.

Yang, Y., Y. Chen, K. Yang, J. Cermak, and Y. Chen. 2021. High-resolution aerosol retrieval over urban areas using sentinel-2 data. *Atmospheric Research* 264:105829.

Zhang, Y.-L. and F.J.S.r. Cao. 2015. Fine particulate matter (PM 2.5) in China at a city level. *Scientific Reports* 5:14884. https://doi.org/10.1038/srep14884.

Zheng, Z., Z. Yang, Z. Wu, and F. Marinello. 2019. Spatial variation of NO2 and its impact factors in China: An application of Sentinel-5P products. *Remote Sensing* 11(16):1939.

Zhou, C., Q. Liu, Y. Tang, and X. Xin. 2009. Validation and understanding of moderate resolution imaging spectroradiometer (MODIS) C005 aerosol product using Aerosol Robotic Network (AERONET) ground-based data in the north of China. Pages III-973–III-976 in *Proceedings IEEE International Geoscience & Remote Sensing Symposium*, held in Boston, MA. https://doi.org/10.1109/IGARSS.2008.4779514.

Zhu, Z. and C. E. Woodcock. 2012. Object-based cloud and cloud shadow detection in Landsat imagery. *Remote Sensing of Environment* 118:83–94.

WHO'S WHO IN ASPRS

Founded in 1934, the American Society for Photogrammetry and Remote Sensing (ASPRS) is a scientific association serving thousands of professional members around the world. Our mission is to advance knowledge and improve understanding of mapping sciences to promote the responsible applications of photogrammetry, remote sensing, geographic information systems (GIS) and supporting technologies.

BOARD OF DIRECTORS

BOARD OFFICERS

President
Lorraine B. Amenda, PLS, CP
Towill, Inc

Vice President
Amr Abd-Elrahman
University of Florida

Treasurer
John McCombs
NOAA

President-Elect
Bandana Kar
Oak Ridge National Lab

Past President
Christopher Parrish, Ph.D
Oregon State University

Secretary
Harold Rempel
ESP Associates, Inc.

COUNCIL OFFICERS

ASPRS has six councils. To learn more, visit https://www.asprs.org/Councils.html.

Sustaining Members Council
Chair: Ryan Bowe
Deputy Chair: Melissa Martin

Standing Committee Chairs Council
Chair:
Deputy Chair:

Region Officers Council
Chair: Demetrio Zourarakis
Deputy Chair: Jason Krueger

Technical Division Directors Council
Chair: Hope Morgan
Deputy Chair:

Early-Career Professionals Council
Chair: Youssef Kaddoura
Deputy Chair:

Student Advisory Council
Chair: Oscar Duran
Deputy Chair:

TECHNICAL DIVISION OFFICERS

ASPRS has seven professional divisions. To learn more, visit https://www.asprs.org/Divisions.html.

Geographic Information Systems Division
Director: Denise Theunissen
Assistant Director: Jin Lee

Lidar Division
Director: Ajit Sampath
Assistant Director: Mat Bethel

Photogrammetric Applications Division
Director: Ben Wilkinson
Assistant Director: Hank Theiss

Primary Data Acquisition Division
Director: Srini Dharmapuri
Assistant Director: Ravi Soneja

Professional Practice Division
Director: Hope Morgan
Assistant Director: Matt Elious

Remote Sensing Applications Division
Director: Tao Liu
Assistant Director: Indu Jeyachandran

Unmanned Autonomous Systems (UAS)
Director: Jacob Lopez
Assistant Director: Bahram Salehi

REGION PRESIDENTS

ASPRS has 13 regions to serve the United States. To learn more, visit https://www.asprs.org/regions.html.

Alaska Region

Cascadia Region
Jimmy Schulz

Eastern Great Lakes Region
Craig Fry

Florida Region
Matt LaLuzerne

Gulf South
Cody Condron

Heartland Region
Whit Lynn

Mid-South Region
David Hughes

North Atlantic Region
Kurt Lutz

Northeast Region

Pacific Southwest Region
Omar Mora

Potomac Region
Jason Brown

Rocky Mountain Region
Trent Casi

Western Great Lakes Region
Adam Smith

Change Detection in SAR Images through Clustering Fusion Algorithm and Deep Neural Networks

Zhikang Lin, Wei Liu, Yulong Wang, Yan Xu, and Chaoyang Niu

Abstract

The detection of changes in synthetic aperture radar (SAR) images based on deep learning has been widely used in landslides detection, flood disaster monitoring, and other fields of change detection due to its high classification accuracy. However, the inherent speckle noise in SAR images restricts the performance of existing SAR image change detection algorithms by clustering analysis. Therefore, this paper proposes a novel method for SAR image change detection based on clustering fusion and deep neural networks. We first used hierarchical fuzzy c-means clustering (HFCM) to process two different images to obtain HFCM classification results. Then a fusion strategy is designed to obtain the fused image from the two HFCM classified images as the pre-classification result. Furthermore, a lightweight deep neural network composed of a decomposition convolution module and an auxiliary classification module was proposed; the former module could reduce network parameters by 28%, and the latter could reduce network parameters by 33.3%. To improve the recognition performance of the network, the classification layer was replaced by the regression layer at the outcome of the network. By comparing the experiments of different methods on five data sets, the performance of our proposed method is superior.

Introduction

Synthetic aperture radar (SAR) can penetrate clouds, in contrast to optical radar, is unaffected by the weather and can obtain detailed geographic information, which is crucial in certain circumstances (Zhang et al. 2016). For example, emergency events such as landslides, floods, and earthquakes occur with rain and dark clouds. In these cases, real-time optical images will not be available, but change detection based on SAR images will be a feasible method. Therefore, SAR images are widely used in change detection and have been applied in flood detection (Lu et al. 2014; Schlaffer et al. 2015), urban analysis (Yousif and Ban 2013; Hu and Ban 2014), forest monitoring (Pantze et al. 2014), and other fields, and in-depth research has been carried out in the past few years. The purpose of change detection is to analyze two remote sensing images taken at different times in the same geographical region (Bazi et al. 2005; Bazi et al. 2010; Blaschke 2010). There are many multi-temporal SAR data available for monitoring and application with the progress of SAR imaging technology. However, the inherent speckle noise in SAR images makes relevant studies difficult (Hussain et al. 2013; Oliver and Quegan 2004).

Traditional research on SAR image change detection generally involves two fundamental processes (Schubert et al. 2013): difference image (DI) generation and DI analysis. One approach to generating DI is through the application of a single operator operation (Villasensor et al. 1993; Longbotham et al. 2012). For example, the subtraction operator or ratio operator can be applied pixel by pixel to the intensity of two multi-temporal images to produce a DI (Celik 2010). Ratio operators are widely used because they are more suitable for SAR image statistics and are robust to radiation errors (Rignot and Van Zyl 1993). Log-ratio (LR) (Hou et al. 2014; Gao et al. 2014; Dekker 1998) is the most widely used technique to obtain DI, and log-ratio operators are considered robust to calibration and radiation errors. Therefore, the effect of speckle noise can be reduced. However, the noisy region remains in the DI generated by the log-ratio operator. Improved LR can effectively suppress unwanted speckle noise (Gao et al. 2014). The other is the combined operation of several DIs (Zheng et al. 2013), such as joint difference image and neighborhood-based ratio (NR) (Gong et al. 2011). However, the degree of difference between pixel classes cannot be improved entirely by a single operator. Joint operators can enhance the difference between two types of pixels. Using artificial methods to design the fusion mode of each operator, such as the weighted sum of two detectors, work well for parts but not for the whole image (Li et al. 2016).

For DI analysis methods, collaborative representation technology (Zhang et al. 2011) has attracted extensive attention from researchers in remote sensing applications. Li and Du (2014) developed a collaborative representation method based on the spatial and spectral features for hyperspectral image classification. Jiang et al. (2017) proposed a hyperspectral image classification method to integrate spatial information, adding spatial regularization terms into the representation objective function of collaborative representation. Inspired by these works, Gao et al. (2018) uses the neighborhood ratio cooperative representation change detection method (NR_CR), which can classify by using the spatial information of neighborhood pixels, suppressing multiplicative speckle noise and improving the performance of change detection. Additionally, neighborhood ratio and extreme learning machine (NR-ELM) (Gao et al. 2016) were used to find the changed areas in the image, which is a traditional method of rapid change detection. Su et al. (2017) used a binary mathematical morphological filtering algorithm for change detection maps, Wuhan University (2006) applied a Markov random field (MRF) model to describe environment-related information, and Chen et al. (2014) developed a variational model for change detection in multi-temporal SAR images. All these traditional change detection methods can improve the accuracy and reliability of change detection.

In recent years, due to the powerful capability of deep learning in high-dimensional feature extraction and autonomous learning, some breakthrough SAR image change detection methods have been proposed one after another. Deep neural networks have good detection ability due to their excellent ability to extract deep features, and the accuracy of deep learning change detection methods is widely better than traditional change detection methods. In 2017, Liu et al. (2017) recommended a two-channel convolutional neural network (CNN) change detection method. In this method, two original images were processed by CNN and the obtained results were wholly connected to generate segmentation results. Simultaneously, a monitoring frame for polarimetric SAR change detection through deep learning was proposed to detect urban change (De et al. 2017). In 2018, Liu et al. (2018) suggested a SAR

Information Engineering University, Zhengzhou 450000, China (greatliuliu@163.com).

Contributed by Ribana Roscher, August 12, 2022 (sent for review October 11, 2022; reviewed by Fatih Nar, Ilyas Nurmemet, Gang Hong)..

Photogrammetric Engineering & Remote Sensing
Vol. 89, No. 6, June 2023, pp. 373–384.
0099-1112/22/373–384

doi: 10.14358/PERS.22-00108R2

image change detection method based on locally constrained CNN, which imposed spatial constraints on the output layer of CNN. To extract robust features of change detection from superpixels, a cascade shrinkage autoencoder based on shrinkage penalty was proposed to improve the robustness and local continuity of SAR images (Lv et al. 2018). In 2019, Gao et al. used a method based on log-ratio and convolutional wavelet neural network (CWNN) (Gao et al. 2019) to find change regions. In 2021, an unsupervised small area change detection method through multi-scale superpixel reconstruction and convolutional wavelet neural network is proposed (Zhang et al. 2021).

Although the above SAR image deep learning method performs well in SAR image change detection, it still has some deficiencies. Due to strong speckle noise, some pixels in the binary classification described above will be misallocated, resulting in false positives. Therefore, obvious speckle noise will bring great false positives to change detection. A certain number of high-quality training samples is still a problem in deep learning networks. Although deep learning makes full use of original images and samples with high confidence, pixels can be divided into the most likely classes. In addition, training samples of rectangular blocks centered on the pixels of interest tend to introduce artifacts at the boundaries of these rectangular patches, resulting in the uncertainty of classified images. For instance, unchanged pixels and variational pixels may appear in the image patch simultaneously, which increases the difficulty of distinguishing the changed and unchanged classes. Furthermore, if a manual method is used to select training samples, the manual workload will increase, and the target of automatic change detection cannot be completed. Moreover, in the case of artificial selection, it is difficult to show all types of change with limited sample size. To solve the above issues, this paper proposes an unsupervised change detection method through clustering fusion and deep neural networks. In this method, unsupervised sample selection is carried out from the clustering fusion image through pre-classification to obtain reliable invariant samples, intermediate samples, and variable samples. Then, the deep neural network is established and trained. Lastly, the middle classes in the clustering fusion image are reclassified using the predicted results of the regression layer.

Our research objectives are as follows:

1. To obtain high confidence training samples, a clustering fusion algorithm based on the HFCM algorithm is proposed to get a better clustering fusion image as the pre-classification result.
2. To improve the detection accuracy, a deep neural network with a regression layer instead of a classification layer was designed to classify the intermediate classes in the pre-classification results.

Methodology

The implementation of the overall approach is shown in Figure 1. In the part of pre-classification and sample selection, the principal DI is established by the LR operator and NR operator. Then, hierarchical FCM (HFCM) (Gao et al. 2018; Gao et al. 2016; Gao et al. 2019) is used to process the two DI and obtain HFCM image results. Then, the clustering fusion algorithm is used to fuse the results of two HFCM images. Thus, we could get the label diagrams of changed class, unchanged class, and an intermediate class. Then, the corresponding training samples are extracted from the two original SAR images according to the label map. Because the changed sample is typically much smaller than the invariant sample, the virtual sample is used to enrich the changed class. In the stage of the deep neural network, the designed network is used to train the network, and the pixels of the middle class are assigned to the classes that change or remain unchanged to obtain the change label map of only the change class and the middle class

Generation of Difference Image

The first step is to generate initial DI from two original SAR images. Log-ratio and neighborhood-based ratio are two commonly used operators in many change-detection studies. The DI is defined as follows:

$$I_{LR}(m,n)=\left|\log_{10}\left(\frac{I_1(m,n)+1}{I_2(m,n)+1}\right)\right| \tag{1}$$

$$I_{NR}(m,n)=\theta\times\frac{\min\left\{I_1(m,n),I_2(m,n)\right\}}{\max\left\{I_1(m,n),I_2(m,n)\right\}}+(1-\theta)\times\frac{\sum_{i\in\Omega\wedge i\neq m,n}\min\left\{I_1(m,n),I_2(m,n)\right\}}{\sum_{i\in\Omega\wedge i\neq m,n}\max\left\{I_1(m,n),I_2(m,n)\right\}} \tag{2}$$

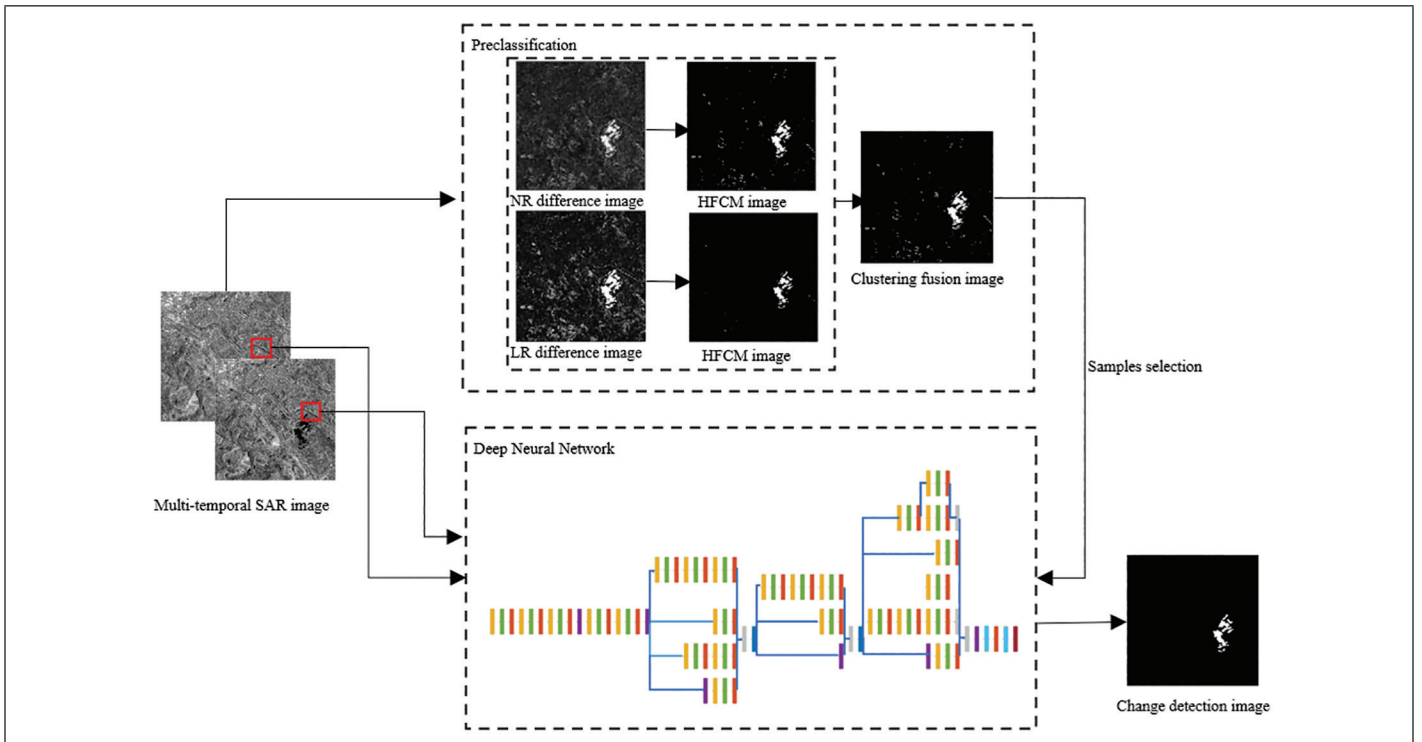

Figure 1. Flowchart of the proposed change detection method. SAR = synthetic aperture radar; NR = neighborhood-based ratio; LR = log-ratio; HFCM = hierarchical fuzzy c-means clustering.

$$\theta = \frac{\sigma(m,n)}{\mu(m,n)} \tag{3}$$

where $\sigma(m, n)$ denotes the variance of the gray level in the neighborhood NR_{mn}. The size of NR_{mn} is r × r. $\mu(m, n)$ represents the mean of the gray level in the neighborhood NR_{mn}. The coefficient θ is a measure of the local heterogeneity: a low value of θ indicates that the local area is homogeneous. In contrast, a high value of θ suggests that the local area is heterogeneous. Therefore, if θ obtains a low weight, the local area is homogeneous, and the second part of Equation 2 plays a leading role in I_{NR} generation. If θ receives a high value, the local area is heterogeneous, and the first part of Equation 2 plays a leading role in I_{NR} generation. $I_{LR}(m, n)$ is a log-ratio operator.

NR DI shows different features in edge regions, uniform regions, and non-uniform regions, blurring the noise, but at the same time making the change regions inconspicuous and easily leading to missed alarms. And LR DI can convert multiplicative speckle noise into additive noise by logarithmic operation, which removes the noise and highlights the change region at the same time. However, some noise is highlighted at the same time, which is likely to cause higher false alarms. With the help of HFCM algorithm, a clustering and fusion strategy is used to complement the advantages and disadvantages of NR and LR to generate initial pre-processed images and provide reliable training samples.

HFCM Clustering Algorithm

After obtaining DI by using the NR operator, a deep learning change detection method is used. Training samples and labels need to be provided to the network. Therefore, a hierarchical FCM clustering algorithm is used to divide the pixels in DI into three categories: changed class Ω_c, unchanged class Ω_u, and middle class Ω_i. A diagram of the HFCM clustering algorithm is shown in Figure 2 and the hierarchical FCM clustering algorithm is described in detail as follows:

Step 1: Input LR difference image and NR difference image by Equations 1 and 2, respectively.

Step 2: FCM algorithm was adopted to process DI, and the pixels were divided into two clusters: Ω_c^1 and Ω_u^1. The pixel number of Ω_c^1 is represented by T^1. Then, the upper bound of the actual variation class was defined as $TT = \sigma \cdot T^1$. Here, σ was set to 1.15 in our experiment.

Step 3: FCM algorithm was used to process DI again, and DI was divided into six classes, arranged in descending order according to the average pixel value, Ω_1^2, Ω_2^2, …, Ω_6^2. Clustering with a higher mean meant a higher probability of change. The average value of Ω_1^2 was the largest and was defined as a changed class; the average value of Ω_6^2 was the smallest and was defined as the unchanged class. The number of pixels in the six clusters was defined as T_1^2, T_2^2, …, T_6^2, respectively. The parameters were set as t =1, $c = T_1^2$. The pixel in Ω_1^2 was specified to the class Ω_c.

Step 4: $t = t + 1$, $c := c + T_t^2$ was set.

Step 5: If $c<TT$, pixels in Ω_t^2 were assigned to the class Ω_i. Otherwise, the pixels in Ω_t^2 were set to the class Ω_u. Go to Step 4, and continue until t =6.

Step 6: As a result, the pre-classification change image could be denoted as an image with labels (Ω_c, Ω_i, Ω_u).

Generation of Clustering Fusion Image

When the HFCM algorithm obtains the label image, some pixels are misclassified, so we design a clustering fusion algorithm based on HFCM. The misclassified pixels by HFCM are allocated to the middle class and then classified by the deep neural network to reduce the misclassification caused by the HFCM algorithm and ultimately improve the detection accuracy. The clustering fusion algorithm we designed is as follows:

Step 1: Use the number of connected pixels of NR and LR to calculate their respective weight matrices W_{P_1}, W_{P_2}. As shown in Figure 3, obtain W_{P_1}, W_{P_2} from the HFCM image result.

Step 2: Obtain the connected region with varying pixel value 1 and intermediate pixel value 0.5 from the HFCM clustering result in Figure 3a, and calculate the weight according to the number of pixels in each connected region. As shown in Figure 3b, the more prominent area indicates a more connected area in Figure 3b, which suggests greater weight.

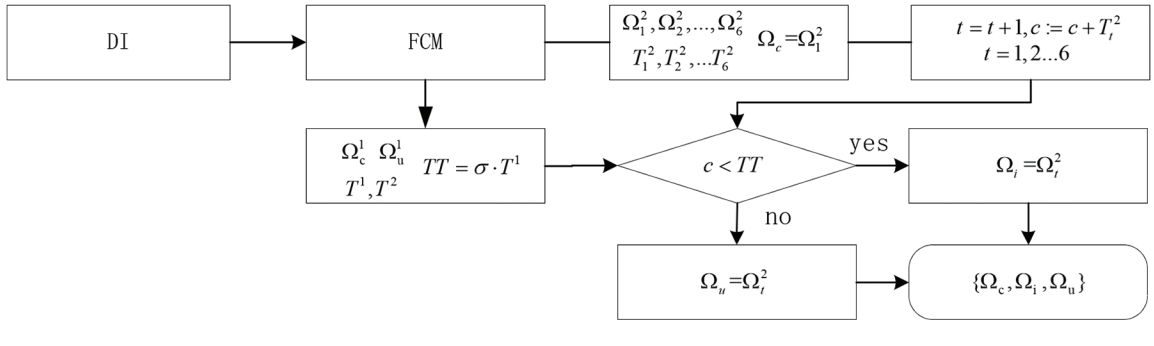

Figure 2. Diagram of hierarchical fuzzy c-means clustering (HFCM) clustering algorithm. DI = difference image; FCM = fuzzy c-means clustering.

(a) (b)

Figure 3. Generation of weight matrix image: (a) Clustering fusion image; (b) Weight matrix image.

Step 3: The pixels in NR DI and LR DI are traversed to compare the pixel values and calculate the fusion strategy image. The specific process is shown in Figure 4.

Sample Selection

After obtaining the result of the fusion clustering image, we get image fragments from the original image according to the changed and unchanged labels. Let $S_k^{I_1}$ represent the block of interest centered on pixel k in the image I_1 and $S_k^{I_2}$ represent the block of interest centered on pixel k in the image I_2. Set the size of each patch to $w \times w$. The two blocks of interest are connected into a new image block to obtain a training sample block $\{S_k\}$, $k = 1, 2, \ldots, N$ with a size of $2w \times w$. Here N is set to the total number of pixels for the changed and unchanged classes. Feature extraction and training of samples are carried out through the network.

In practical experiments, many weights in our proposed network needed to be adjusted. If these weights were not appropriate, the training process would fall into the local minimum of the loss function, and the performance of change detection would be poor. To solve this problem, many samples must be used in the training process. However, in SAR image change detection, the number of available change samples is usually much smaller than the number of invariant samples. To solve the difficulty of imbalance between classes, we used virtual samples to enrich the training samples.

Virtual samples S_k' can be generated by the linear addition of two given samples of the same kind in appropriate proportions.

$$S_k' = \alpha S_i (1 - \alpha) S_j + \beta \tag{4}$$

S_i and S_j are the two training samples in the class with a small number, which are the samples in the change class. They will be proportionally combined. The samples produced by combining two samples in the same class are given the same label in the same class. Here, α is a random value uniformly distributed in the range [0, 1]. β represents random Gaussian noise with a mean of 0 and a variance of 0.001. Next, N samples are randomly generated from the actual samples $\{S_k\}$, $k = 1, 2, \ldots, N$. Then real samples, as well as virtual samples, are adopted as network training samples to obtain appropriate weights.

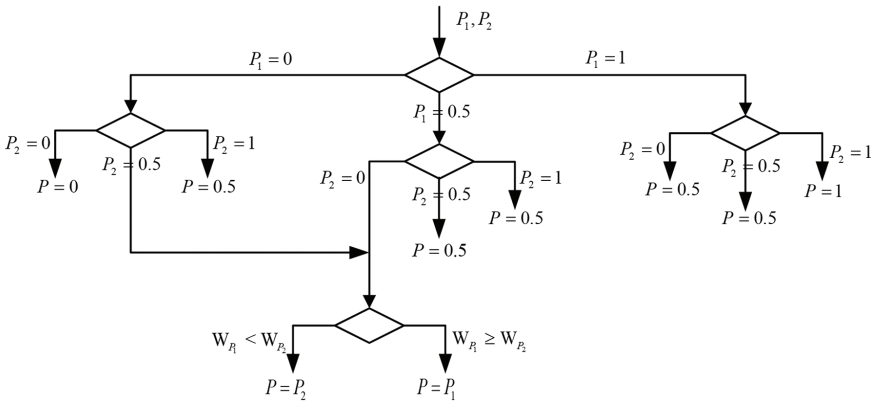

Figure 4. Flowchart of the proposed clustering fusion image generation. P_1 represents the neighborhood-based ratio (NR) difference image processed by the hierarchical fuzzy c-means clustering (HFCM) algorithm, and P_2 represents the log-ratio (LR) difference image processed by the HFCM algorithm. $P = 0,0.5,1$ represent pixel values of 0, 0.5, and 1, respectively in the generated clustering fusion image P, while W_{P_1} and W_{P_2} represent weight matrices corresponding to P_1 and P_2, respectively.

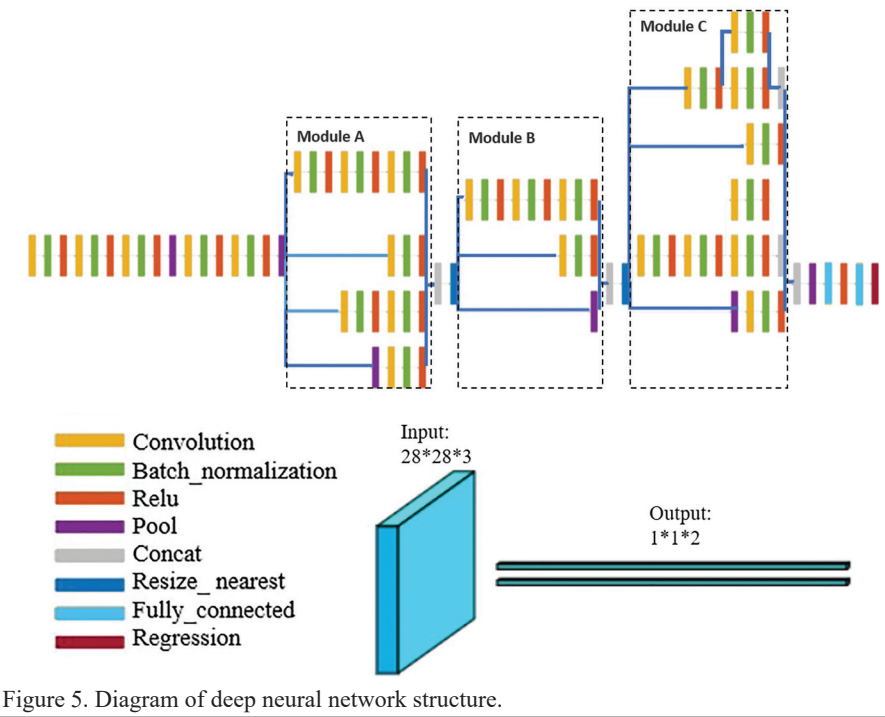

Figure 5. Diagram of deep neural network structure.

Training Network

The results of the deep neural networks were much better than traditional algorithms. With the increase of the structural complexity and parameter number of a neural network, the detection effect will be improved, but at the same time, its computational complexity and computational resource cost will also rise. At present, the change detection model with good performance has the characteristics of significant computation and many parameters, which to a large extent restricts its application in a resource-constrained environment and real-time inline system. If the model can be improved, such as removing redundant parameters or optimizing the network structure, its powerful detection ability can be transplanted to equipment with weak computing ability, reducing the calculation amount of the change detection model and decreasing the volume of the model will significantly promote the detection efficiency and incorporate the acceleration mode into the role.

The network is derived from the Inception network (Szegedy et al. 2016), a well-known lightweight network that has been successfully applied in the field of image processing. Our network diagram is shown in Figure 5. It is mainly composed of three modules. In Module A, by replacing one 5×5 convolution with two 3×3 convolutions, the number of parameters can be decreased by 28% ($1 - 3 \times 3 \times 2/(5 \times 5)$). After the decomposition, one convolution layer is followed by an activation function, where formerly there was only one 5×5 convolution and one activation function, now there are two 3×3 convolutions. Thus, there are two activation functions, which increase the power of nonlinear expressions. Module B can effectively reduce the amount of calculation and parameter transmission. In general, convolutional networks use pooling operations to shrink the grid size of feature images. To avoid presentation bottlenecks, the dimensions of network filter activation are increased before maximum or average pooling. Module C involves decomposition to asymmetric convolution, which replaces 3×3 convolution with one 1×3 convolution and one 3×1 convolution, thus reducing the number of parameters by

33%. At the end of the network, to find the optimal fitting result, the regression layer is used to replace the previous classification layer as the network output, and two prediction vectors P_1 and P_2 are output, both of which represent the corresponding predicted value of the intermediate class Ω_i. The threshold T^* is set based on the average value of the difference between P_1 and P_2. Then, the intermediate class Ω_i is divided into changed class Ω_c and unchanged class Ω_u by threshold T^* (see Equations 5 and 6), where mean denotes the mean value of regression output. After the classification of intermediate classes is completed, the detection results obtained here are combined with the changed and unchanged classes in the preprocessing process to form the final binary change detection results, thus improving the detection accuracy to a certain extent. The specific network parameters are shown in Table 1:

$$T^* = mean(|P_1 - P_2|) \tag{5}$$

$$\begin{cases} \Omega_i \in \Omega_u, \ \Omega_i > T^* \\ \Omega_i \in \Omega_c, \ \Omega_i \le T^* \end{cases} \tag{6}$$

Experiments

Description of Data Sets

Six actual SAR image data sets are used to prove the performance of the proposed approach. Table 2 lists a detailed description of each data set, including sensor type, band, polarization, location, imaging date, image size, and reason for the variation. The data set and its ground reference images are shown in Figure 6 and Figure 7 (see next page). All data are derived from publicly available data used for dual-temporal SAR image change detection, and the ground reference images are manually labeled.

Evaluation Criteria

The evaluation results are obtained by comparing the experiments with the actual ground reference image. The evaluation criteria are as follows: true positive (TP) is the number of changed pixels that are correctly detected; true negative (TN) is the number of correctly detected unchanged pixels; false positive (FP) is the number of incorrectly detected changed pixels; false negative (FN) is the number of changed pixels that are falsely indicated as absent; and the three overall criteria, the total error (OE) is the ratio of the sum of FP and FN to the total number of pixels, PCC is the ratio between correctly detected pixel number and total pixel number, and Kappa coefficient (KC). PCC is defined as:

$$\mathrm{PCC} = \frac{\mathrm{TP} + \mathrm{TN}}{\mathrm{TP} + \mathrm{FP} + \mathrm{TN} + \mathrm{FN}} \tag{7}$$

However, reflecting the detection precision of PCC is not convincing and fair, and in our experiments, the value of the PCC is very small, indicating a small difference. Still, the KC usually involves more detailed information, heterogeneity is separable, and the result is credible. It is also a precision evaluation metric, with a value range of 0–1. Its size reflects the detection accuracy. The closer the KC value is to 1, the better the performance is. It can be calculated as:

Table 1. Network parameters.

Type	Patch Size/Stride	Input Size
conv	3 × 3/2	28 × 28 × 1
conv	3 × 3/1	13 × 13 × 32
conv padded	3 × 3/1	11 × 11 × 32
pool	3 × 3/2	11 × 11 × 64
conv	1 × 1/1	5 × 5 × 64
conv	3 × 3/1	5 × 5 × 80
inception	Module A	3 × 3 × 192
inception	Module B	1 × 1 × 256
inception	Module C	17 × 17 × 768
pool	3 × 3/2	17 × 17 × 2048
linear	logits	1 × 1 × 2048
fully	regression	1 × 1 × 1000

$$\mathrm{KC} = \frac{(\mathrm{PCC} - \mathrm{PRE})}{(1 - \mathrm{PRE})} \tag{8}$$

$$\mathrm{PRE} = \frac{\mathrm{Nc} \times (\mathrm{TP} + \mathrm{FP}) + \mathrm{Nu} \times (\mathrm{FN} + \mathrm{TN})}{(\mathrm{TP} + \mathrm{FP} + \mathrm{FN} + \mathrm{TN})^2} \tag{9}$$

Nu and Nc are unchanged pixels and variable pixels, respectively, in the assumed ground reference. In comparison with KC and PCC, PCC often has little difference in experimental results and lacks credibility. KC considers more information and is more convincing in the final detection accuracy.

Results

In this section, different experimental images, and numerical results of different data sets are analyzed. Through comparison, the effectiveness and performance of this method were proven. Three advanced methods, namely neighborhood-based ratio and cooperative representation (NR_CR) (Gao et al. 2018), neighborhood-based ratio and extreme learning machine (NR-ELM) (Gao et al. 2016), and convolutional wavelet neural network (CWNN) (Gao et al. 2019), were used as comparison methods, and the setting of all parameters in each process was the same as those in the references. First of all, to evaluate the performance of our proposed method, the proposed clustering fusion (CF) algorithm was used to replace the pre-processing method among the three methods, and the CF_ELM, CF_CWNN, and CF_CR results were obtained, which proved the effectiveness of our clustering fusion algorithm. Then, the clustering fusion algorithm was added into our designed network to demonstrate the performance of our proposed change detection method based on clustering fusion and deep neural networks.

It can be seen from Bern's data set that they all have loss of change information. the smallest value of FP(55) for CF_CR but the largest false alarm for FN(261), and the smallest area of FN(79) false alarm for CF_CWNN but the largest false alarm for FP(349). Our deep

Table 2. Detail of real SAR data set.

Data Set	Bern	Farmland	San Francisco	River	Coastline	Zhengzhou
Sensor	ERS-2	Radarsat-2	ERS-2	Radarsat-2	Radarsat-2	Gaofen-3
Band	C	C	C	C	C	C
Polarization	VV	VV	VV	VV	VV	VV
Location	Bern, Switzerland	Dongying, China	San Francisco, America	Dongying, China	Dongying, China	Zhengzhou, China
Date	1999.04	2008.06	2003.08	2008.05	2008.06	2021.07.20
	1999.05	2009.06	2004.05	2009.05	2009.06	2021.07.24
Size	301 × 301	291 × 291	256 × 256	233 × 356	296 × 184	1000 × 1000
Changes	Flood	Farming	Flood	Flood	Flood	Flood

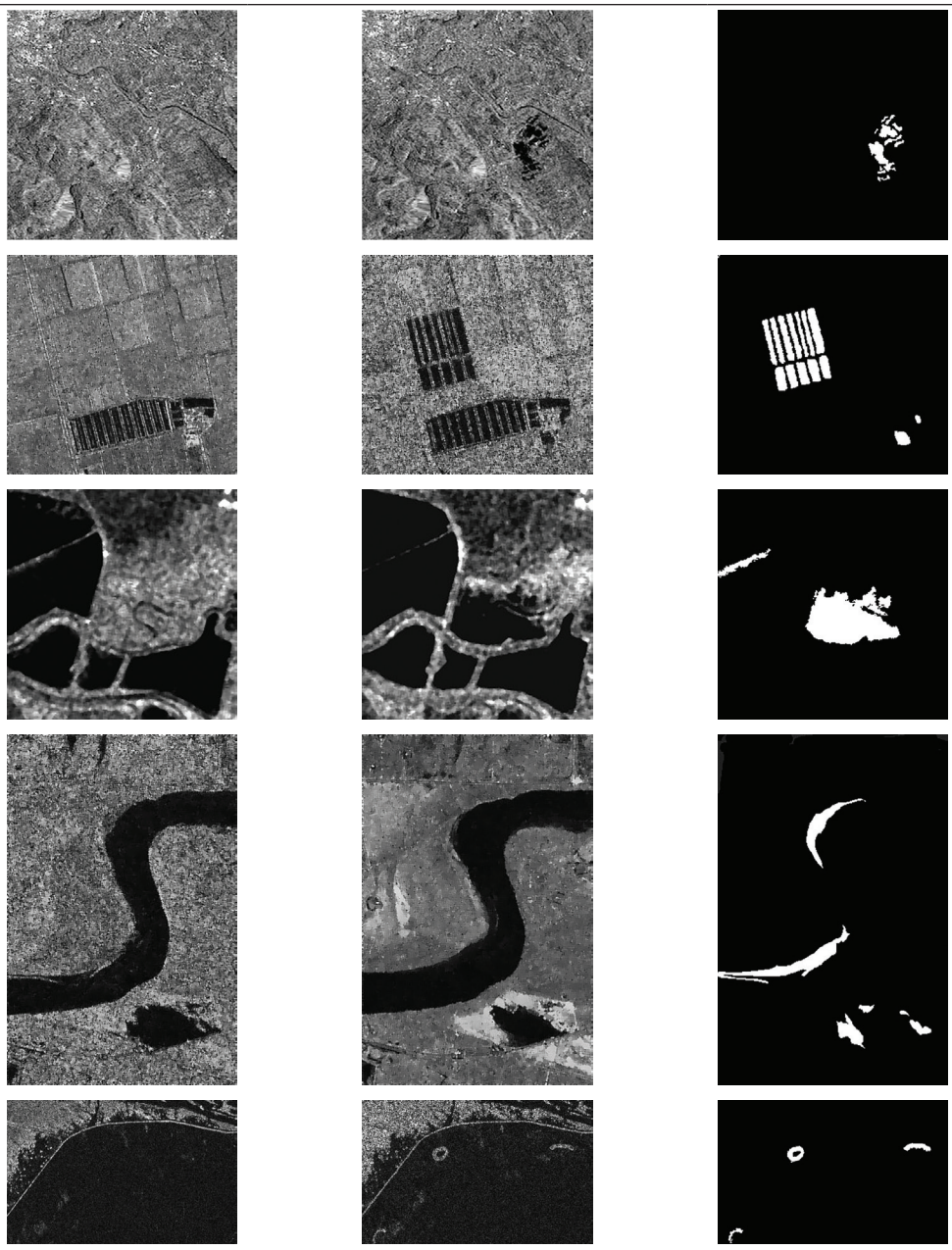

(a) (b) (c)

Figure 6. Multi-temporal real SAR image and its ground reference. The first row is the Bern data sets. The second is the farmland data sets of the Yellow River Estuary. The third row is the San Francisco data sets. The fourth row is the inland data set of the Yellow River estuary. The fifth row is the Coastline data sets of the Yellow River Estuary. (a) Images acquired at time 1. (b) Images acquired at time 2. (c) Ground reference images.

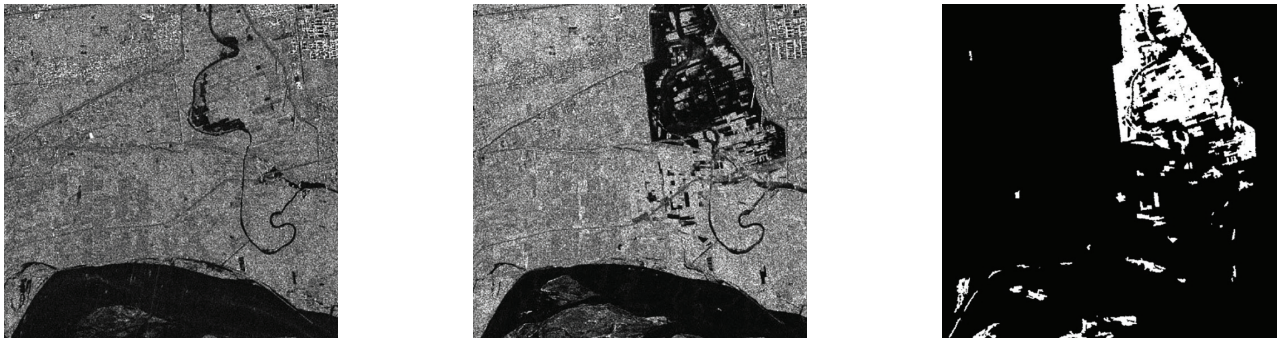

(a) (b) (c)

Figure 7. Zhengzhou data sets. (a) Images acquired at time 1. (b) Images acquired at time 2. (c) Ground reference images.

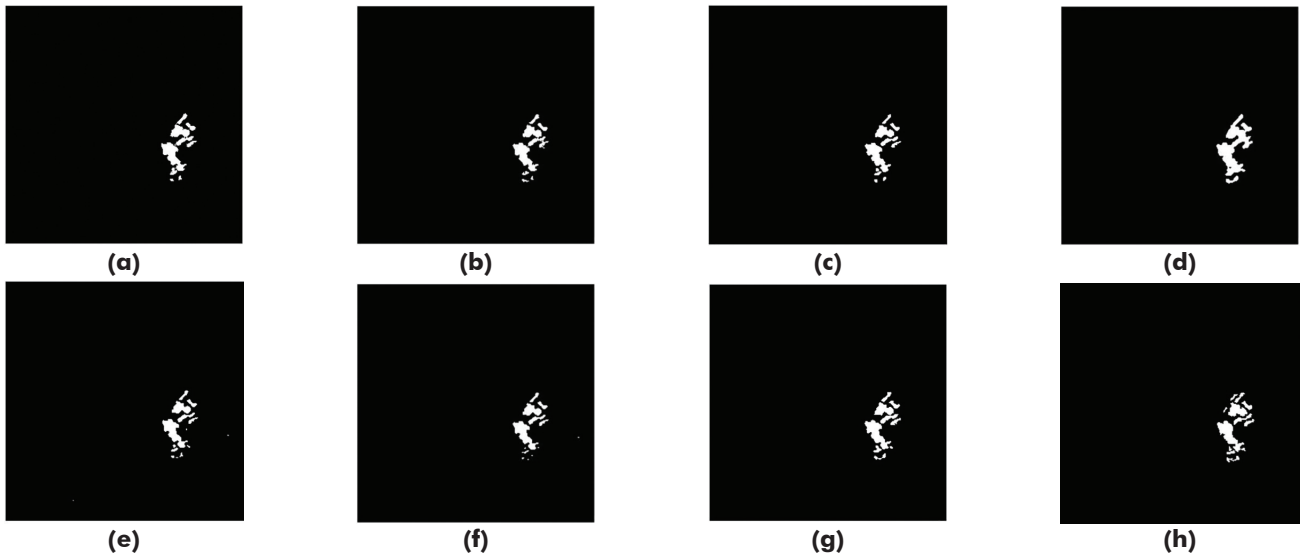

Figure 8. Final change detection images of the Bern data set obtained by different methods. (a) Acquired by neighborhood-based ratio and extreme learning machine (NR_ELM). (b) Acquired by clustering fusion and extreme learning machine (CF_ELM). (c) Acquired by convolutional wavelet neural network (CWNN). (d) Acquired by CF_CWNN. (e) Acquired by namely neighborhood-based ratio and cooperative representation (NR_CR). (f) Acquired by CF_CR. (g) Acquired by using our proposed approach. (h) Ground truth.

Table 3. Change detection results of the Bern data set obtained by different methods. The excellent value for each metric is shown in bold.

Method	FP	FN	OE (%)	PCC (%)	KC (%)
NR_ELM	141	200	0.38	99.62	84.66
CF_ELM	102	219	0.35	99.65	85.18
CWNN	89	203	0.32	99.68	86.54
CF_CWNN	349	**79**	0.47	99.53	83.14
NR_CR	72	227	0.33	99.67	85.96
CF_CR	**55**	261	0.35	99.65	84.81
Proposed method	135	146	**0.31**	**99.69**	**87.58**

FP = false positive; FN = false negative; OE = total error; PCC = the ratio between correctly detected pixel number and total pixel number; KC = Kappa coefficient; NR_ELM = neighborhood-based ratio and extreme learning machine; CF_ELM = clustering fusion and extreme learning machine; CWNN = convolutional wavelet neural network; CF_CWNN = clustering fusion and convolutional wavelet neural network; NR_CR = neighborhood-based ratio and cooperative representation; CF_CR = clustering fusion and cooperative representation.

Table 4. Change detection results of the farmland area of the Yellow River Estuary data set obtained by different methods. The excellent value for each metric is shown in bold.

Method	FP	FN	OE	PCC	KC
NR_ELM	76	1788	2.20	97.91	77.83
CF_ELM	121	1254	1.62	98.46	84.58
CWNN	291	672	1.14	98.92	89.98
CF_CWNN	382	524	1.07	98.98	90.95
NR_CR	**63**	2300	2.79	97.35	70.25
CF_CR	86	1435	1.80	98.29	82.57
Proposed method	293	**464**	**0.89**	**99.15**	**92.25**

FP = false positive; FN = false negative; OE = total error; PCC = the ratio between correctly detected pixel number and total pixel number; KC = Kappa coefficient; NR_ELM = neighborhood-based ratio and extreme learning machine; CF_ELM = clustering fusion and extreme learning machine; CWNN = convolutional wavelet neural network; CF_CWNN = clustering fusion and convolutional wavelet neural network; NR_CR = neighborhood-based ratio and cooperative representation; CF_CR = clustering fusion and cooperative representation.

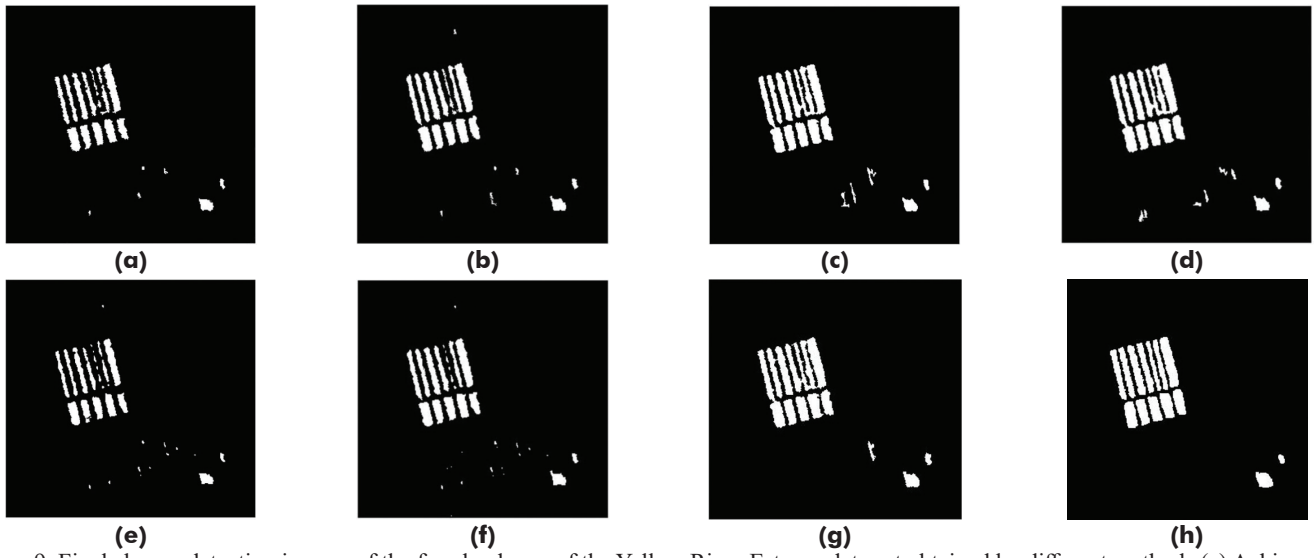

Figure 9. Final change detection images of the farmland area of the Yellow River Estuary data set obtained by different methods (a) Achieved by neighborhood-based ratio and extreme learning machine (NR_ELM). (b) Achieved by clustering fusion and extreme learning machine (CF_ELM). (c) Achieved by convolutional wavelet neural network (CWNN). (d) Achieved by clustering fusion and convolutional wavelet neural network (CF_CWNN). (e) Achieved by neighborhood-based ratio and cooperative representation (NR_CR). (f) Achieved by clustering fusion and cooperative representation (CF_CR). (g) Achieved by using our proposed approach. (h) Ground truth.

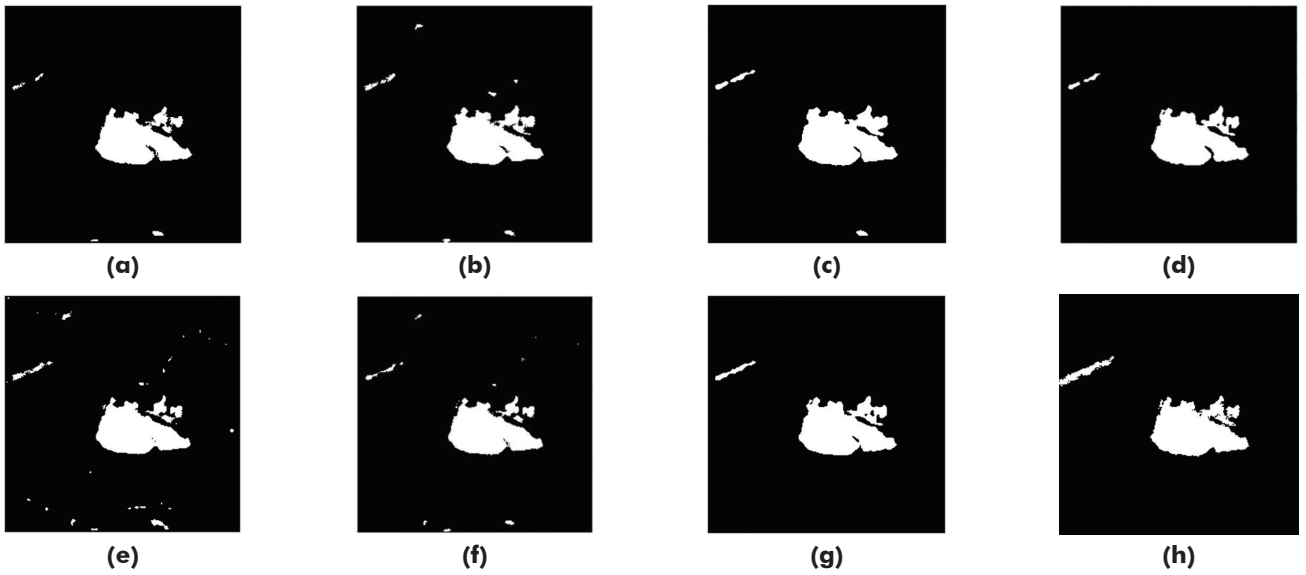

Figure 10. Final change detection images of the San Francisco data set obtained by different methods. (a) Achieved by neighborhood-based ratio and extreme learning machine (NR_ELM). (b) Achieved by clustering fusion and extreme learning machine (CF_ELM). (c) Achieved by convolutional wavelet neural network (CWNN). (d) Achieved by clustering fusion and convolutional wavelet neural network (CF_CWNN). (e) Achieved by neighborhood-based ratio and cooperative representation (NR_CR). (f) Achieved by clustering fusion and cooperative representation (CF_CR). (g) Achieved by using our proposed approach. (h) Ground truth.

Table 5. Change detection results of the San Francisco data set obtained by different methods. The excellent value for each metric is shown in bold.

Method	FP	FN	OE	PCC	KC
NR_ELM	533	311	1.29	98.71	90.51
CF_ELM	241	487	1.11	98.89	91.42
CWNN	359	**295**	1.00	99.00	92.53
CF_CWNN	148	429	0.88	99.12	93.18
NR_CR	298	606	1.38	98.62	89.28
CF_CR	**118**	682	1.22	98.78	90.26
Proposed method	184	308	**0.75**	**99.25**	**94.28**

FP = false positive; FN = false negative; OE = total error; PCC = the ratio between correctly detected pixel number and total pixel number; KC = Kappa coefficient; NR_ELM = neighborhood-based ratio and extreme learning machine; CF_ELM = clustering fusion and extreme learning machine; CWNN = convolutional wavelet neural network; CF_CWNN = clustering fusion and convolutional wavelet neural network; NR_CR = neighborhood-based ratio and cooperative representation; CF_CR = clustering fusion and cooperative representation.

neural network based on cluster fusion performs well in PCC (99.69) and KC (87.58). In this data set, our CF_CWNN method and CF_CR method do not improve the KC value, but the improvement of the cluster fusion algorithm is still present. The FN value (79) of the CF_CWNN method is significantly better than the FN (203) of the CWNN because the cluster fusion method gives many pixels the opportunity to be reclassified, which performs significantly in this data set. Because the cluster fusion method reduces misclassified pixel points in producing fused HFCM results, the FP(55) of the CF_CR method is less than that of NR_CR(72).

For farmland data sets, we illustrate the role of deep neural networks. In comparison with CWNN, the FP value of our method has little difference from that of CWNN, because the number of pixels corrected by CF is smaller, while the FN value reduces by 208 because our neural network has more layers and more detailed extraction features. The neural network uses a comparison between predicted extreme values, which gives the results of the last part a chance to be reclassified compared with the direct network classification method. Due to the last regression output integrating the output of the two feature vectors, some leakage alarms were correctly classified, and the result of KC (92.25) is 2.27 higher than CWNN.

For the San Francisco data set, there are obvious false positives in all methods. Our CF method significantly reduces FP in all original methods, among which CF_CR FP (118) has the lowest false positive. The results of the clustering fusion algorithms CF_ELM, CF_CWNN, and CF_NR obtained in this paper improved the three methods of NR_ELM, CWNN, and NR_CR. By comparing CWNN and our method, the FN values of the two methods have little difference, but the FP value of the latter (184) is better than the former (359). Here, our CF method plays a major role, and many intensive speckle-noise samples are suppressed during pre-classification. Lastly, the deep neural network based on clustering fusion proposed by us has an excellent performance in PCC (99.25) and KC (94.28).

In the Inland data sets, CWNN was severely affected by scattered noise, with a high FP value (3238) and a poor effect. On the contrary, NR_ELM and NR_CR show low FP, which indicates that deep learning methods have high requirements on reliable samples. Our method improves all three methods and has the highest detection accuracy among all the changed area edge detection methods. Comparing the FP of CWNN (3238) and FP of our method (697), it was obvious that our method had a better effect, mainly because many samples were improved by our CF method during pre-classification.

For the Coastline data set, aside from our method, most methods are greatly influenced by scattering noise and fail to detect the changed region. In our method, the clustering fusion graph avoids the influence of inaccurate training samples. Therefore, our method enhances the detection accuracy, and the time consumption is acceptable. The river data set is less effective. Because the river area in the SAR image looks very dark, the backward scattering of the electromagnetic wave to the river is relatively weak. Therefore, the signal noise of the SAR image is relatively shallow under soft speckle noise. Ergo, in this case, there is a significant difference between the pixel values of the two images in the river region, and the pixels in the river region can be easily classified as a changed class.

In addition, we add the Zhengzhou data sets, and use the proposed method to perform experiments on all data sets of different sizes under the same conditions and record the computation time. The relationship between calculation time and size is shown in Table 8. Obviously, larger sizes require more computation time.Discussion

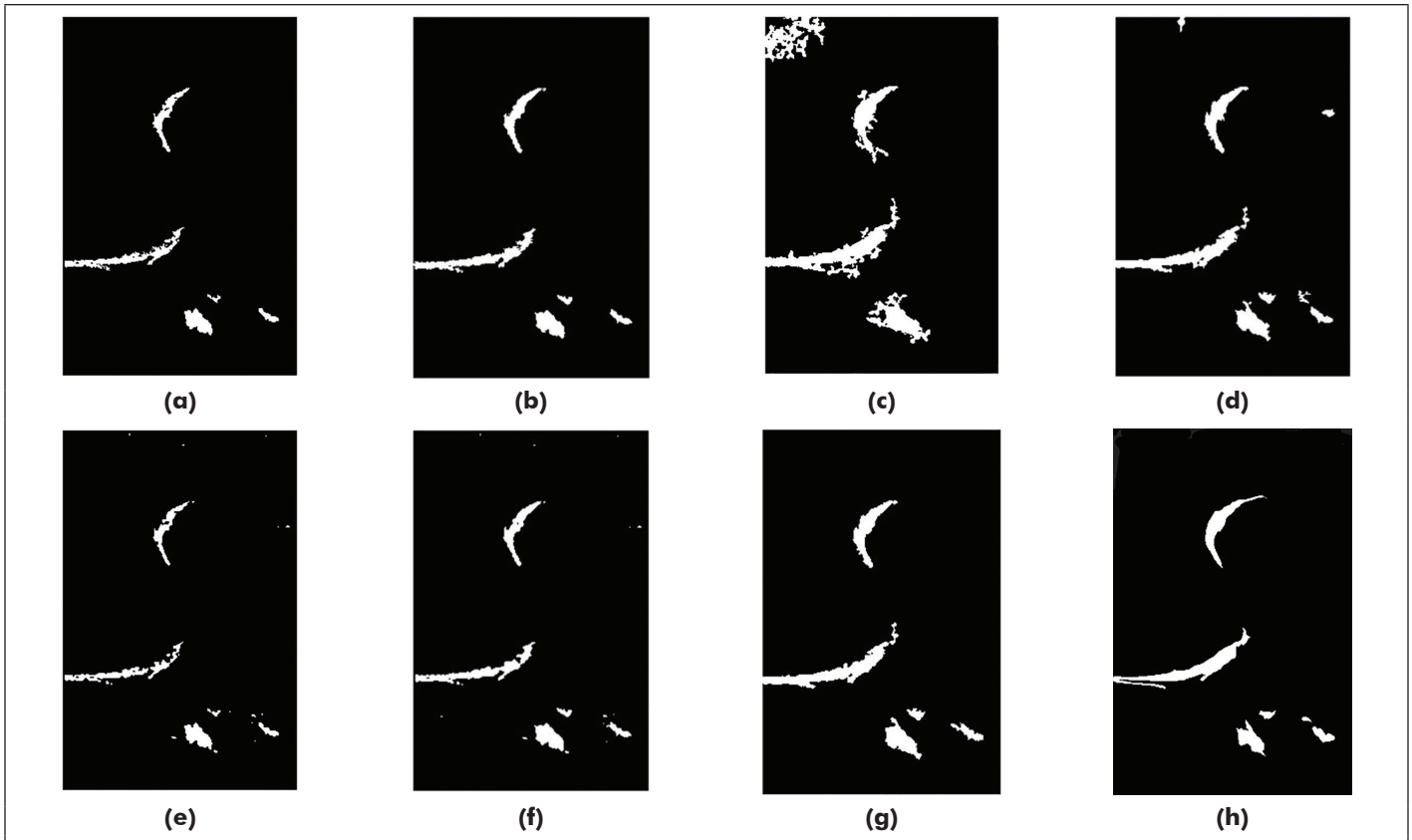

Figure 11. Final change detection images of the river of the Yellow River Estuary data set obtained by different methods. (a) Achieved by neighborhood-based ratio and extreme learning machine (NR_ELM). (b) Achieved by clustering fusion and extreme learning machine (CF_ELM). (c) Achieved by convolutional wavelet neural network (CWNN). (d) Achieved by clustering fusion and convolutional wavelet neural network (CF_CWNN). (e) Achieved by neighborhood-based ratio and cooperative representation (NR_CR). (f) Achieved by clustering fusion and cooperative representation (CF_CR). (g) Achieved by using our proposed approach. (h) Ground truth.

Table 6. Change detection results of the Inland of the Yellow River Estuary data set obtained by different methods. The excellent value for each metric is shown in bold.

Method	FP	FN	OE	PCC	KC
NR_ELM	192	1019	1.46	98.54	73.17
CF_ELM	319	740	1.28	98.72	78.36
CWNN	3238	369	4.35	93.65	54.72
CF_CWNN	868	**269**	1.37	98.63	80.55
NR_CR	**175**	1167	1.62	98.38	69.22
CF_CR	282	794	1.30	98.70	77.62
Proposed method	697	283	**1.18**	**98.82**	**82.72**

FP = false positive; FN = false negative; OE = total error; PCC = the ratio between correctly detected pixel number and total pixel number; KC = Kappa coefficient; NR_ELM = neighborhood-based ratio and extreme learning machine; CF_ELM = clustering fusion and extreme learning machine; CWNN = convolutional wavelet neural network; CF_CWNN = clustering fusion and convolutional wavelet neural network; NR_CR = neighborhood-based ratio and cooperative representation; CF_CR = clustering fusion and cooperative representation.

Table 8. Relationship between the size of data sets and computation time.

Data Sets	Bern	Farmland	San Francisco	Inland	Coastline	Zhengzhou
Size	301 × 301	291 × 291	256 × 256	233 × 356	296 × 184	1000 × 1000
Time (s)	562.46	576.30	564.83	589.80	605.82	989.71

Parameters Selection

In this section, two parameters will be discussed, namely, the nearest neighbor size of the NR operator in pre-classification and the patch size of the training sample in the deep neural network. These two parameters affect the learning ability of the deep learning change detection method based on hierarchical fuzzy c-means clustering fusion. As shown in Figure 13, with the coastline data as an example, when the nearest neighbor size is set to 5, the result is optimal. In our experiment, we set it uniformly to 3. For the training sample block size, when the value is 36, the result is optimal. In our experiment, it is uniformly set to 28. Figure 12 reflects the effect of the choice of two parameters on the results, i.e., the neighbor size of the NR difference image and the size of training sample patch of the deep neural network on the Kappa value, respectively.

Deep Learning Framework for Change Detection

In the proposed method, the clustering fusion algorithm in the pre-classification stage completes the initial pre-classification task, and the deep neural network in the deep learning stage completes the final classification task. The clustering fusion algorithm in the pre-classification stage can be applied to various other methods that take clustering as the pre-classification result (Gao et al. 2016), and other deep neural networks in the deep learning stage can also be used in place of the deep neural network designed by us. Therefore, the proposed approach can be regarded as two modules. It does not limit the use of deep learning models. Moreover, a clustering algorithm can also be applied to a variety of other deep learning change detection algorithms. If only a complete classification is used in two modules, many false positives and false negatives will

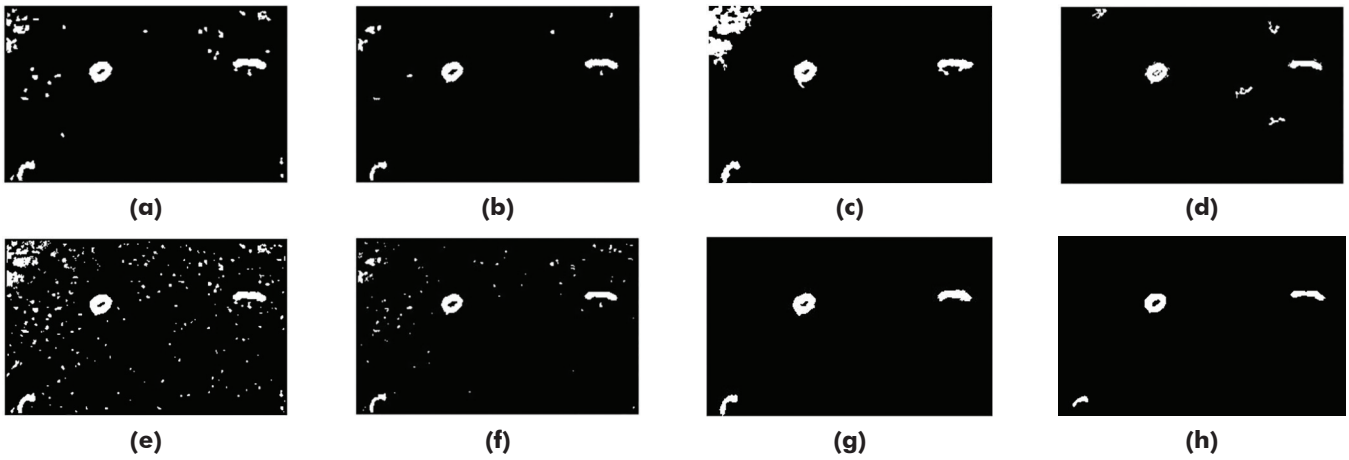

Figure 12. Final change detection images of the Coastline of Yellow River Estuary data set obtained by different methods. (a) Achieved by neighborhood-based ratio and extreme learning machine (NR_ELM). (b) Achieved by clustering fusion and extreme learning machine (CF_ELM). (c) Achieved by convolutional wavelet neural network (CWNN). (d) Achieved by clustering fusion and convolutional wavelet neural network (CF_CWNN). (e) Achieved by neighborhood-based ratio and cooperative representation (NR_CR). (f) Achieved by clustering fusion and cooperative representation (CF_CR). (g) Achieved by using our proposed approach. (h) Ground truth.

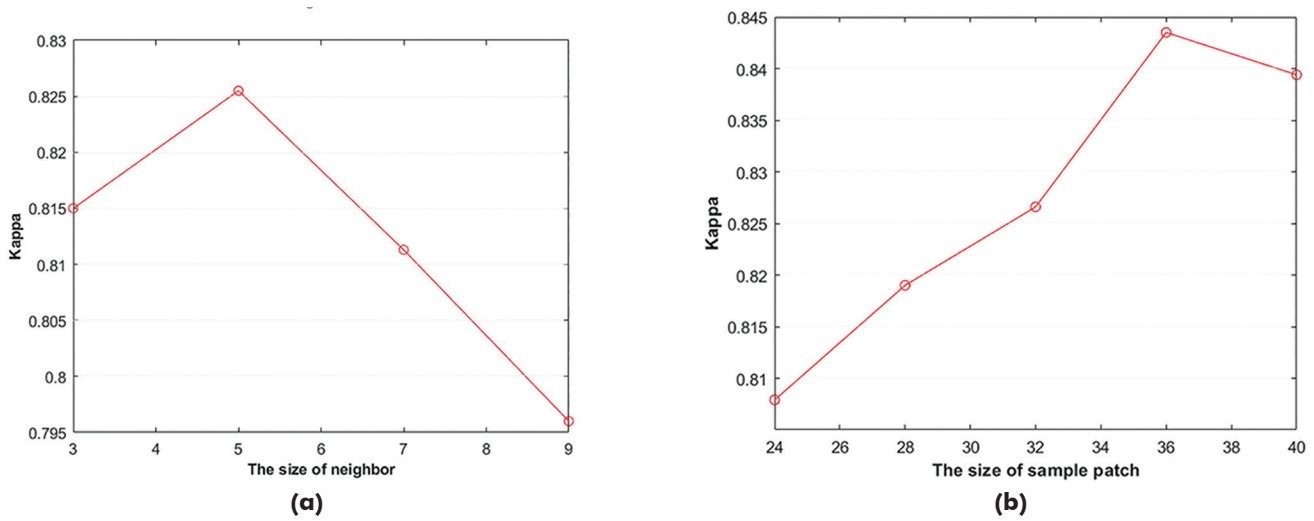

Figure 13. The influence of the size of neighbor and the sample patch for Kappa on the Coastline of Yellow River Estuary data set.

Table 7. Change detection results of the Coastline of Yellow River Estuary data set obtained by different methods. The excellent value for each metric is shown in bold.

Method	FP	FN	OE	PCC	KC
NR_ELM	934	10	1.73	98.27	54.76
CF_ELM	328	29	0.66	99.34	75.80
CWNN	1667	**9**	3.08	96.92	40.24
CF_CWNN	313	111	0.78	99.22	69.28
NR_CR	1948	10	3.60	96.40	36.39
CF_CR	540	47	1.08	98.92	64.75
Proposed method	**233**	19	**0.46**	**99.54**	**81.90**

FP = false positive; FN = false negative; OE = total error; PCC = the ratio between correctly detected pixel number and total pixel number; KC = Kappa coefficient; NR_ELM = neighborhood-based ratio and extreme learning machine; CF_ELM = clustering fusion and extreme learning machine; CWNN = convolutional wavelet neural network; CF_CWNN = clustering fusion and convolutional wavelet neural network; NR_CR = neighborhood-based ratio and cooperative representation; CF_CR = clustering fusion and cooperative representation.

be produced. All of them can be used as part of the other change detection methods and are suitable for engineering implementation.

Comparison with Other Methods

The proposed deep neural network based on hierarchical fuzzy c-means clustering and fusion is vital for obtaining the desired change detection performance. The former classifies pixels into three categories: variable class, invariant class, and intermediate class. Regardless of the change caused by strong speckle noise, or the change caused by the change of Israeli terrain, after our pre-classification, the uncertain change class and the unchanged class will be well divided into the intermediate classes. This is so that the neural network can be classified again, which greatly reduces the FP rate and FN rate. Based on this principle, in the deep neural network stage, although there is still a noise when the same target in SAR image has a strong correlation, our network output layer by regression output two lines characteristic vector, rather than using classification layer binary classification directly. The reason for this is that the conventional binary classification will result in a lot of pixels by mistake classification. Such misclassification is greatly reduced by using a regression output threshold, which greatly improves the identification of two previously indistinguishable changes.

Our method is evaluated theoretically by comparing several benchmark methods. The results showed the effectiveness and robustness of our proposed method. The advantage of this approach is that each part can be easily extended, and the entire framework can be developed into an end-to-end supervised network. In future studies, this method should monitor changes over a wider range of data.

Analysis of Unbalanced Training Samples

When selecting training samples, we use far fewer training samples of variable types in data sets than those of constant types, which are detrimental to the training network. To avoid the imbalance between variable training samples and constant training samples, virtual samples are used to enrich the training samples of a few classes. In contrast to other data enhancement methods, virtual samples can effectively capture the potential recognition information of changed classes by exploring the visual feature space through linear learning image blocks. The refined data maximizes the feature space of the changed class and supports network training. Different sample selection methods will have different effects on the results. In future work, the problem of unbalanced training samples for unsupervised change detection methods can also be improved.

Discussion on Regression Layer Output of Deep Neural Network

In the past, the neural network was either classified output or single regression output, and the detection results had low accuracy due to many FP or FN (Gao et al. 2019). Our depth layer neural network adopts the regression forecast samples of the middle class, and the output of the single feature vector to represent categories. With the two feature vectors by regression output, we take the difference from the difference characteristic vector, and then select the difference feature vector of the mean value as a threshold of feature vector binary classification, before the change detection results are obtained. This is our constant exploration and innovation of regression prediction, which reduces many misclassifications and improves detection accuracy.

Conclusions

In this paper, we proposed a change detection method for multi-temporal SAR images based on cluster fusion and deep neural networks. The algorithm first generates pre-classification results containing three classes: change class, unchanged class, and intermediate class by the cluster fusion algorithm, allowing more pixels that are easily misclassified to belong to the intermediate class and effectively selecting the change class and unchanged class. Then, virtual samples are used to solve the problem of imbalance between the samples of changed and unchanged classes. For the reclassification of intermediate classes, a deep neural network was designed to train both change and unchanged class samples. In the network results, the regression layer was used to replace the classification layer. The difference between the two feature vectors output by the regression layer is set as a threshold for the resultant classification again, thus reducing most of the false alarms in the detection results. As a result, erroneous pixels in both pre-classification and final classification can be corrected. The results on five different SAR image data sets validate the feasibility and effectiveness of the proposed method.

The main challenge in the detection of the changes in SAR images in the future is speckle noise, which varies from the human vision mechanism and unique imaging form. However, in terms of image understanding, deep learning neural networks have proved their great potential through their ability to extract high-dimensional features and fit nonlinear functions. Therefore, deep learning neural networks are the preferred method to solve the above problems, but this method will identify false positives and missed positives. Ergo, two problems need to be solved. The first problem is to enhance the recognition ability of deep learning, and the other is to recognize the noise characteristics of SAR images and effectively distinguish the actual changed pixels from noisy pixels.

Acknowledgments

The authors would like to thank all the editors and reviewers for their valuable time and suggestions on this paper, which have greatly improved the quality of this paper.

References

Bazi, Y., F. Melgani and H. D. Al-Sharari. 2010. Unsupervised change detection in multispectral remotely sensed imagery with level set methods. *IEEE Transactions on Geoscience and Remote Sensing* 48(8):3178–3187.

Bazi, Y., L. Bruzzone and F. Melgani. 2005. An unsupervised approach based on the generalized Gaussian model to automatic change detection in multitemporal SAR images. *IEEE Transactions on Geoscience and Remote Sensing* 43(4):874–887.

Blaschke, T. 2010. Object based image analysis for remote sensing. *ISPRS Journal of Photogrammetry and Remote Sensing* 65(1):2–16.

Celik, T. 2010. Change detection in satellite images using a genetic algorithm approach. *IEEE Geoscience and Remote Sensing Letters* 7(2):386–390.

Chen, Y., A. B. Cremers and Z. Cao. 2014. A variational change detection method for multitemporal SAR images. *Remote Sensing Letters* 5(4):342–351.

De, S., D. Pirrone, F. Bovolo, L. Bruzzone and A. Bhattacharya. 2017. A novel change detection framework based on deep learning for the analysis of multi-temporal polarimetric SAR images. Pages 5193–5196 in *Proceedings 2017 IEEE International Geoscience and Remote Sensing Symposium (IGARSS)*. https://doi.org/10.1109/IGARSS.2017.8128171.

Dekker, R. 1998. Speckle filtering in satellite SAR change detection imagery. *International Journal of Remote Sensing* 19(6):1133–1146.

Gao, F., J. Dong, B. Li, Q. Xu and C. Xie. 2016. Change detection from synthetic aperture radar images based on neighborhood-based ratio and extreme learning machine. *Journal of Applied Remote Sensing* 10(4):046019.

Gao, F., X. Wang, Y. Gao, J. Dong and S. Wang. 2019. Sea ice change detection in SAR images based on convolutional-wavelet neural networks. *IEEE Geoscience and Remote Sensing Letters* 16(8):1240–1244.

Gao, G., X. Wang, M. Niu and S. Zhou. 2014. Modified log-ratio operator for change detection of synthetic aperture radar targets in forest concealment. *Journal of Applied Remote Sensing* 8(1):083583.

Gao, Y., F. Gao, J. Dong and S. Wang. 2018. Sea ice change detection in SAR images based on collaborative representation. Pages 7320–7323 in *Proceedings IGARSS 2018-2018 IEEE International Geoscience and Remote Sensing Symposium*. https://doi.org/10.1109/IGARSS.2018.8519461.

Gong, M., Y. Cao and Q. Wu. 2011. A neighborhood-based ratio approach for change detection in SAR images. *IEEE Geoscience and Remote Sensing Letters* 9(2):307–311.

Hou, B., Q. Wei, Y. Zheng and S. Wang. 2014. Unsupervised change detection in SAR image based on Gauss-log ratio image fusion and compressed projection. *IEEE Journal of Selected Topics in Applied Earth Observations and Remote Sensing* 7(8):3297–3317.

Hu, H. and Y. Ban. 2014. Unsupervised change detection in multitemporal SAR images over large urban areas. *IEEE Journal of Selected Topics in Applied Earth Observations and Remote Sensing* 7(8):3248–3261.

Hussain, M., D. Chen, A. Cheng, H. Wei and D. Stanley. 2013. Change detection from remotely sensed images: From pixel-based to object-based approaches. *ISPRS Journal of Photogrammetry and Remote Sensing* 80:91–106.

Jiang, J., C. Chen, Y. Yu, X. Jiang and J. Ma. 2017. Spatial-aware collaborative representation for hyperspectral remote sensing image classification. *IEEE Geoscience and Remote Sensing Letters* 14(3):404–408.

Li, F., F. Fang and G. Zhang. 2016. Unsupervised change detection in SAR images using curvelet and L1-norm based soft segmentation. *International Journal of Remote Sensing* 37(14):3232–3254.

Li, W. and Q. Du. 2014. Joint within-class collaborative representation for hyperspectral image classification. *IEEE Journal of Selected Topics in Applied Earth Observations and Remote Sensing* 7(6):2200–2208.

Liu, F., L. Jiao, X. Tang, S. Yang, W. Ma and B. Hou. 2018. Local restricted convolutional neural network for change detection in polarimetric SAR images. *IEEE Transactions on Neural Networks and Learning Systems* 30(3):818–833.

Liu, T., Y. Li, Y. Cao and Q. Shen. 2017. Change detection in multitemporal synthetic aperture radar images using dual-channel convolutional neural network. *Journal of Applied Remote Sensing* 11(4):042615.

Longbotham, N., F. Pacifici, T. Glenn, A. Zare, M. Volpi, D. Tuia, E. Christophe, J. Michel, J. Inglada, J. Chanussot and Q. Du. 2012. Multi-modal change detection, application to the detection of flooded areas: Outcome of the 2009–2010 data fusion contest. *IEEE Journal of Selected Topics in Applied Earth Observations and Remote Sensing* 5(1):331–342.

Lu, J., L. Giustarini, B. Xiong, L. Zhao, Y. Jiang and G. Kuang. 2014. Automated flood detection with improved robustness and efficiency using multi-temporal SAR data. *Remote Sensing Letters* 5(3):240–248.

Lv, N., C. Chen, T. Qiu and A. K. Sangaiah. 2018. Deep learning and superpixel feature extraction based on contractive autoencoder for change detection in SAR images. *IEEE Transactions on Industrial Informatics* 14(12):5530–5538.

Oliver, C. and S. Quegan. 2004. *Understanding Synthetic Aperture Radar Images.* Raleigh, N.C.: SciTech Publishing.

Pantze, A., M. Santoro and J. E. Fransson, 2014. Change detection of boreal forest using bi-temporal ALOS PALSAR backscatter data. *Remote Sensing of Environment* 155:120–128.

Schlaffer, S., P. Matgen, M. Hollaus and W. Wagner. 2015. Flood detection from multi-temporal SAR data using harmonic analysis and change detection. *International Journal of Applied Earth Observation and Geoinformation* 38:15–24.

Schubert, A., A. Faes, A. Kääb and E. H. Meier. 2013. Glacier surface velocity estimation using repeat TerraSAR-X images: Wavelet-vs. correlation-based image matching. *ISPRS Journal of Photogrammetry and Remote Sensing* 82:49–62.

Su, M. A., K.-Z. Deng, H.-f. Zhuang and Y.-f. Han. 2017. Change detection of SAR images based on KI criterion and mathematical morphology filter. *Laser Journal* 38(235): 36–40.

Szegedy, C., V. Vanhoucke, S. Ioffe, J. Shlens and Z. Wojna. 2016. Rethinking the inception architecture for computer vision. Pages 2818–2826 in *Proceedings 2016 IEEE Conference on Computer Vision and Pattern Recognition (CVPR)*. https://doi.org/10.1109/CVPR.2016.308.

Rignot, E. J. and J. J. Van Zyl. 1993. Change detection techniques for ERS-1 SAR data. *IEEE Transactions on Geoscience and Remote Sensing* 31(4):896–906.

Villasensor, J., D. R. Fatland and L. D. Hinzman. 1993. Change detection on Alaska's north slope using repeat-pass ERS-1 SAR images. *IEEE Transactions on Geoscience and Remote Sensing* 31(1):227–236.

Wuhan University. 2006. Change detection in multitemporal SAR images using MRF models. *Geomatics and Information Science of Wuhan University* 31(4):312–315. https://doi.org/10.1016/S0379-4172(06)60092-9.

Yousif, O. and Y. Ban. 2013. Improving urban change detection from multitemporal SAR images using PCA-NLM. *IEEE Transactions on Geoscience and Remote Sensing* 51(4):2032–2041.

Zhang, L., M. Yang and X. Feng. 2011. Sparse representation or collaborative representation: Which helps face recognition? Pages 471–478 in *Proceedings 2011 International Conference on Computer Vision*. https://doi.org/10.1109/ICCV.2011.6126277.

Zhang, X., H. Su, C. Zhang, X. Gu, X. Tan and P. M. Atkinson. 2021. Robust unsupervised small area change detection from SAR imagery using deep learning. *ISPRS Journal of Photogrammetry and Remote Sensing* 173:79–94.

Zhang, Y., H. Wu, H. Wang and S. Jin. 2016. Distance measure based change detectors for polarimetric SAR imagery. *Photogrammetric Engineering & Remote Sensing* 82(9):719–727.

Zheng, Y., X. Zhang, B. Hou and G. Liu. 2013. Using combined difference image and *k*-means clustering for SAR image change detection. *IEEE Geoscience and Remote Sensing Letters* 11(3):691–695.

Strategies for Forest Height Estimation by High-Precision DEM Combined with Short-Wavelength PolInSAR TanDEM-X

Hongbin Luo, Wanqiu Zhang, Cairong Yue, and Si Chen

Abstract

The purpose of this article is to explore forest height estimation strategies using topographic data (DEM) combined with TanDEM-X while comparing the effect of volume scattering complex coherence selection on forest height estimation in the traditional random volume over ground (RVoG) three-stage algorithm. In this study, four experimental strategies were designed for comparison based on TanDEM-X polarized interferometric synthetic aperture radar (PolInSAR) data, TanDEM-DEM, and 42 field-measured data. Our results show that in the RVoG model, (1) a reference ground phase to select the volume scattering complex coherence provides greater accuracy in determining forest height, (2) forest height estimation can be achieved by directly using DEM as ground phase information without relying on model solving and obtaining a more accurate forest height than TanDEM-X alone, and (3) the highest estimation accuracy is obtained by using DEM as coherence information among all schemes. Although the difference in forest height estimation results is not significant in this study, it still proves that the forest height estimation strategy of high-precision DEM combined with short-wavelength PolInSAR can not only improve the forest height estimation accuracy but also simplify the solving process of the RVoG model, which is an important reference for global forest parameter estimation and ecosystem detection based on spaceborne PolInSAR.

Introduction

Forests are an important component of terrestrial ecosystems, and monitoring forests is particularly crucial in the context of global climate change (Gholz 1982; Houghton 2005; Hall *et al.* 2011). As a key parameter of forest vertical structure, height is an effective indicator of forest biomass, carbon stock, and forest health, and it also can be used to describe forest succession and change (Goetz and Dubayah 2011; Huang *et al.* 2012; Bispo *et al.* 2019) Therefore, for dynamic forest resource monitoring, it is important to acquire forest height information accurately and efficiently. However, traditional forest height measurement relies mainly on manual field surveys, which are accurate but inefficient and expensive in terms of manpower and money, so the traditional method is not suitable for large-area surveys. On the other hand, remote sensing technology can considerably improve the efficiency of forest resource surveys, and it has been widely used in this context (Chirici *et al.* 2016).

At present, remote sensing techniques applied in forest surveys include mainly optical remote sensing, lidar, remote sensing, microwave remote sensing, and so on (Xu *et al.* 2019). Optical remote sensing has the advantages of a short revisit period, wide coverage, and many data sources, and it has been widely used to estimate forest stock volume or biomass, classify forest types, and monitor forest change; however, it is vulnerable to bad weather and can acquire only optical reflectance information, which is not sensitive to the forest vertical structure (Cao *et al.* 2012). Lidar can obtain information about the forest canopy and the 3D structure inside a forest (Maltamo *et al.* 2020) and is not limited by weather conditions, but the observation coverage of lidar is often limited by the use of an airborne platform, and its data acquisition cost is high (Gang and Hay 2011; Wang *et al.* 2020). As for spaceborne lidar platforms, such as ICEsat1, ICEsat2, and GEDI, although they can cover large-scale areas, they can acquire only strip-scale data and cannot obtain continuous surface data (Silva *et al.* 2021). Different from optical remote sensing and lidar, microwave remote sensing not only is active and independent of weather but also can collect data over large areas, so it has significant advantages in monitoring forests (Zhang *et al.* 2017).

As a part of microwave remote sensing, polarized interferometric synthetic aperture radar (PolInSAR) is a combination of polarimetric SAR (PolSAR) and interferometric SAR (InSAR), so it has the characteristics of both PolSAR and InSAR and is sensitive to the shape, backscatter orientation, space distribution, and vertical structure of vegetation over the ground (Graham 1974; Garestier and Le Toan 2010). Therefore, PolInSAR has become one of the main techniques used to estimate forest height. The random volume over ground (RVoG) coherence scattering model is the most widely used model in PolInSAR forest height estimation (Treuhaft *et al.* 1996; Liao *et al.* 2018), and the three-stage forest height inversion method was developed on the basis of the RVoG model (Cloude and Papathanassiou 2003). The three-stage method can use quad-polarized SAR data to first estimate the ground phase through the distribution of multiple interferometric complex coherence, and it then uses a lookup table to invert forest height; it has been successfully applied to different frequencies, including C-, L-, P-, and X-bands (Wang *et al.* 2016; Schlund *et al.* 2019; Kumar *et al.* 2020).

In 2010, the German Aerospace Center (DLR) launched the first dual-satellite simultaneous observation mission—TanDEM-X—which eliminates the temporal decorrelation problem and increases the possibility of accurately estimating forest height and other forest parameters (Kumar *et al.* 2017; Persson *et al.* 2017; Chen *et al.* 2019). However, in forest areas, TanDEM-X could present a problem in obtaining the ground scattering information due to its short-wavelength X-band, the penetration of which into the forest is weak, so the coherence phase centers of various polarized scattering calculated from TanDEM-X data are usually close to the top of the forest canopy. As a result, it is hard for the coherence optimization algorithms to extract phase centers relevant to the surface scattering of the ground. In addition, the observed polarimetric interference complex coherence values of the forest area can deviate from their ideal values for system errors, signal noise, and terrain, and this could cause errors in the ground phase

Hongbin Luo, Wanqiu Zhang*, and Cairong Yue* are with the College of Forestry, Southwest Forestry University, Kunming 650224, China; and the Forestry 3S Engineering Technology Research Center, Southwest Forestry University, Kunming 650224, China (Wanqiu_mou@hotmail.com, cryue@163.com).

Si Chen is with the College of Forestry, Southwest Forestry University, Kunming 650224, China.

**Corresponding authors.*

Contributed by Hongyan Zhang, September 7, 2022 (sent for review February 18, 2023; reviewed by Lianhuan Wei, Alper Yilmaz).

Photogrammetric Engineering & Remote Sensing
Vol. 89, No. 6, June 2023, pp. 385–392.
0099-1112/22/385–392

doi: 10.14358/PERS.22-00116R2

estimation of the three-stage algorithm (Cloude *et al.* 2013; Kugler *et al.* 2014; Managhebi *et al.* 2018). Poor estimation of the ground phase impairs the inversion of the forest height in the next steps. Therefore, improving the accuracy of the ground phase estimation is one of the key approaches to improving TanDEM-X forest height inversion. Many previous studies have used a DTM acquired by airborne lidar as external terrain data to perform forest height inversion with single-pole TanDEM-X data (Cloude *et al.* 2013; Kugler *et al.* 2014; Qi *et al.* 2019), and these studies fully illustrated that an accurate ground phase, obtained from high-precision external terrain data, can improve the inversion accuracy of forest height from TanDEM-X data. Usually, high-precision topographic data can be obtained by airborne or UAV lidar; however, the cost of these data is too high to be applied in a large area. SRTM-DEM, ASTER-DEM, and TanDEM-DEM are medium-precision topographic data with wide regional coverage. In particular, the DEM from the TanDEM-X mission has an overall absolute elevation accuracy of about 3.5 m; when excluding ice-, forest-, and desert-covered areas, the absolute elevation accuracy reaches 0.88 m (Rizzoli *et al.* 2017), and it is currently the global DEM product with the highest accuracy.

The goal of this article is to develop TanDEM-X polarized interferometric data combined with topographic data (DEM) to improve forest height estimation and compare the effect of volume scattering complex coherence selection on forest height estimation results in the traditional RVoG three-stage algorithm. The results of this study will help improve forest height inversion accuracy supported by topographical data for short-wavelength SAR data and also simplify the RVoG three-stage algorithm by reducing model parameters and improving efficiency.

Study Area and Data

Study Area

The study area is located in Simao District, P'er City, Yunnan Province, China. Being a mountainous region with undulating terrain, this area has an average elevation of 1366 m and a maximum height difference of 1036 m. It has a typical southern subtropical monsoon climate, with indistinct dry and wet seasons. Due to its low latitude, this place has a high temperature, high humidity, and much rain year-round, and its average annual temperature and precipitation are 17.8°C and 1524 mm, respectively. This region has high forest coverage; the main forest type in our study area is needle leaf forest, dominated by natural forests, with the dominant species being *Pinus kesiya* var. *langbianensis*. Under abundant moisture and heat conditions, the vegetation under the forest canopy is also more complex.

Field-Measured Data

The field data were acquired in March 2017, and 42 sample plots were examined in the study area. In this region, the dominant tree species is P. kesiya var. langbianensis, and most parts of the forest are mature or middle-aged forests. Here, the forest stand mean height was chosen as a reference for the canopy height. Circular plots were adopted. First, the center of the sample plot was determined by GPS, then the diameter at breast height (DBH) of each tree within the circular field was recorded and the average DBH calculated. Next, three or four trees within the same diameter order of the average DBH were selected as the standard trees, and the heights of the standard trees were measured. Finally, the average height of the standard trees was calculated as the output height of the plot. In the field survey, the tree height was obtained by using a combination of a scale bar, a laser rangefinder, and ultrasonic height measurement. The statistical characteristics of the heights of the sample plots are shown in Table 1.

Table 1. Statistics of the heights of sample plots (unit: m).

Number of Plots	Minimum	Maximum	Average Height	Standard Deviation
42	8.21	20.23	16.11	2.98

TanDEM-X and TanDEM-DEM Data

TanDEM-X consists of two nearly identical SAR satellite constellations. TanDEM-X data, provided by DLR, were acquired on October 6, 2015, in bistatic mode. The data were a quad-polarized single-look complex in the CoSSC format. The effective baseline was 361.31 m, and height of ambiguity(hoa) was 17.7 m.

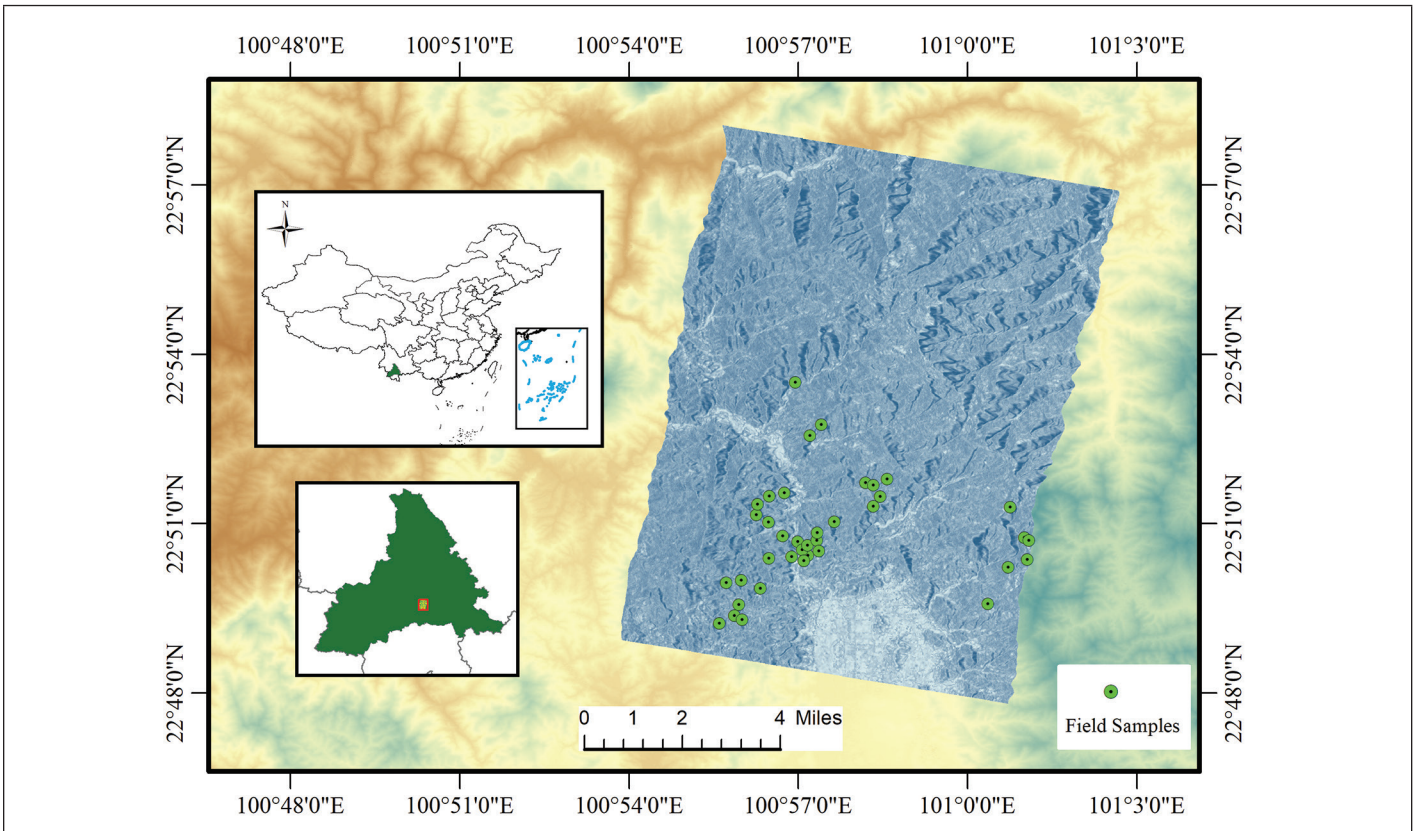

Figure 1. Geographical location of the study area.

The TanDEM-DEM data used in the study were provided by DLR at a resolution of 12×12 m. When generating a global DEM product, the spatial baseline of the two satellites of the TanDEM-X mission is controlled between 120 and 500 m.

Methodology

3RVoG Coherence Scattering Model and Three-Stage Algorithms

RVoG model is a widely used two-layer coherence scattering model (Figure 2) capable of inverting the physical forest height based on the PolInSAR complex coherence (Treuhaft *et al.* 1996; Papathanassiou and Cloude 2001; Hajnsek *et al.* 2009; Kugler *et al.* 2014). In the RVoG model, the forest is regarded as a random-volume scattering layer with a height of h_v, and the ground is an impenetrable layer at a vertical location of Z_0.

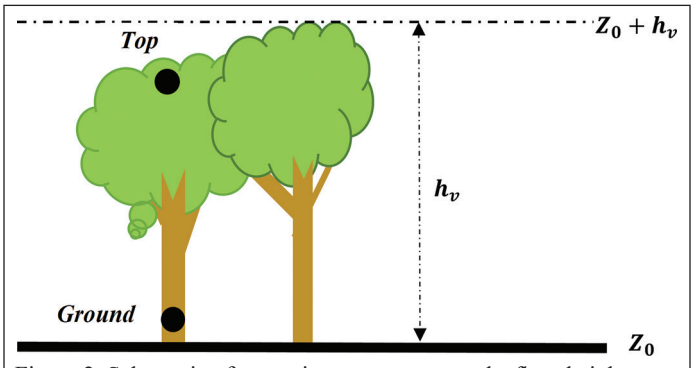

Figure 2. Schematic of scattering centers versus the floor height.

In the RVoG model, when not considering temporal decorrelation, the observed interferometric complex coherence with polarization ω can be expressed as

$$\begin{cases} \gamma(\omega) = e^{j\varphi_0}\left[\gamma_v + L(\omega)(1-\gamma_v)\right] \\ L(\omega) = \dfrac{m(\omega)}{1+m(\omega)} \end{cases} \tag{1}$$

where $m(\omega)$ is the effective ground-to-volume amplitude ratio. When $m(\omega) = 0$, the surface scattering contribution is zero ($\gamma(\omega) = e^{j\varphi_0}\gamma_v$), and when $m(\omega) = \infty$, the phase is on the surface ($\gamma(\omega) = e^{j\varphi_0}$). Here, $e^{j\varphi_0} = e^{jk_z z_0}$ denotes the ground phase, while γ_v denotes the decorrelation caused by vegetation only. γ_v can be expressed as

$$\begin{cases} \gamma_v = \dfrac{2\sigma}{\cos\left(e^{\frac{2\sigma h_v}{\cos(\theta)}} - 1\right)} \displaystyle\int_0^{h_v} e^{jk_z z} e^{\frac{2\sigma z}{\cos(\theta)}} dz = \frac{p}{p_1}\frac{e^{p_1 h_v} - 1}{e^{p h_v} - 1} \\ p = \dfrac{2\sigma\cos(\alpha)}{\cos(\theta-\alpha)} \\ p_1 = p + jk_z \\ k_z = \dfrac{2n\pi\Delta\theta}{\lambda\sin(\theta-\alpha)} = \dfrac{2n\pi B_\perp}{\lambda R\sin(\theta-\alpha)} \end{cases} \tag{2}$$

where h_v is the vegetation height; σ is the extinction coefficient; k_z is the vertical effective wave number, which indicates the sensitivity of the phase to height change; α and R are the range-facing terrain slope angle and the slant distance, respectively; θ is the incident angle; $B_\perp$ is the vertical baseline length; and n depends on the acquisition mode of the radar image (Kugler *et al.* 2015): $n = 2$ for bistatic mode, and $n = 1$ for monostatic mode.

Based on the RVoG model, the three-stage forest height inversion method was proposed by Cloude and Papathanassiou (2003) and is mainly used to invert forest height from single-baseline PolInSAR data. From Equation 1, it can be seen that the interferometric complex coherence values of different polarization states are linearly distributed in the complex plane. Then, based on this linear distribution of multiple polarimetric interferometry complex coherence, the three-stage inversion can solve out the ground phase through a linear-fitting process and then estimate the forest height via Equation 2. The whole process is divided into three stages.

Stage 1

Fit the coherence line using the least squares method with a set of complex coherence values. Here, 15 interferometric complex coherence values under different polarization states were calculated from the polarization interferometry coherence matrix of the master and slave images, including seven coherence values under the linear polarization basis (γ_{HH}, γ_{HHmVV}, γ_{HHpVV}, γ_{HHVV}, γ_{HV}, γ_{HVpVH}, and γ_{VV}), three coherence values under the circular polarization basis (γ_{LL}, γ_{LR}, and γ_{RR}), and five optimized coherence values (γ_{Opt1}, γ_{Opt2}, and γ_{Opt3}) via singular value decomposition coherence optimization (Cloude and Papathanassiou 1998) and γ_{PDhigh} and γ_{PDlow} via phase-diversity coherence optimization (Xie *et al.* 2015).

Stage 2

Solve the ground phase φ_0 from the two intersections (γ_0 and γ_1) where the coherence line intersects the unit circle. According to the physical scattering mechanism of a forest, the HV channel is usually dominated by the volume scattering of the forest canopy and contains little information from the ground; as a result, γ_{HV} should be far away from the coherence corresponding to the ground. Thus, the ground phase can be determined by judging the distances between the two coherence points (γ_0 and γ_1) and γ_{HV}, as shown in Equation 3. Finally, the intersection farthest from γ_{HV} is selected to calculate the ground phase φ_0:

$$\begin{cases} \varphi_0 = \arg(\gamma_0) & |\gamma_{HV} - \gamma_0| > |\gamma_{HV} - \gamma_1| \\ \varphi_0 = \arg(\gamma_1) & |\gamma_{HV} - \gamma_0| < |\gamma_{HV} - \gamma_1| \end{cases} \tag{3}$$

Stage 3

Estimate the forest height h_v and extinction coefficient σ. According to the relationship between γ_v and (h_v, σ) in Equation 2, a two-dimensional lookup table (LUT) is created based on a set of reasonable h_v and σ values. By looking for the smallest distance between γ_{ω_v} and the $e^{j\varphi_0}\gamma_v$ from the LUT, the pair (h_v, σ) fulfilling Equation 4 is taken as the output. Here, we assume the effective ground-to-volume amplitude ratio ($m(\omega) = 0$) for the volume scattering complex coherence γ_{ω_v}:

$$\min_{h_v,\sigma} L = \left\| \gamma_{\omega_v} - e^{j\varphi_0}\frac{p}{p_1}\frac{e^{p_1 h_v} - 1}{e^{p h_v} - 1} \right\| \tag{4}$$

Effect of Volume Scattering Complex Coherence Selection on Inversion Results

In the traditional three-stage inversion algorithm, after the ground phase is determined, the farthest complex is selected as the volume scattering complex to invert the forest height. The HV channel is considered to contain mainly volume scattering from the vegetation layer, so the coherence γ_{HV} is often directly used as the volume scattering coherence in the RVoG three-stage algorithm. However, related studies show that the HV channel includes not only volume scattering but also part of the ground surface scattering; thus, the ground-to-volume magnitude ratio $m(\gamma_{HV})$ is not zero, and the scattering phase center of the HV channel may not be the closest to the top of canopy among all the complex coherence values (Cloude and Papathanassiou 2003).

Therefore, in this study, we examine the effects of volume scattering complex coherence selection on the forest height inversion. In Experiment A, γ_{HV} was used as the volume scattering complex coherence, and in Experiment B, the interferometric complex coherence

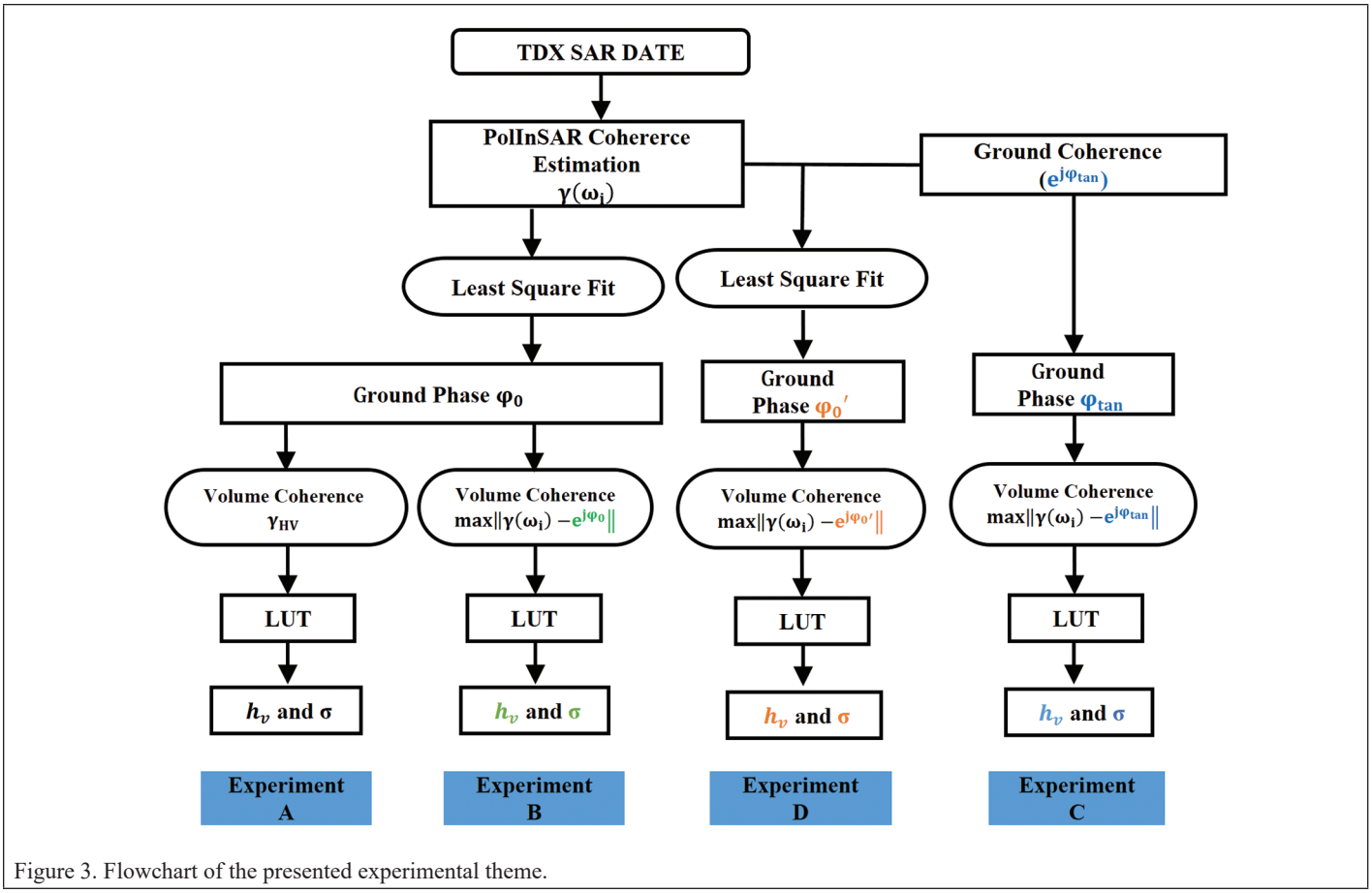

Figure 3. Flowchart of the presented experimental theme.

farthest from the ground phase was selected pixel by pixel as the volume scattering complex coherence to invert the forest height.

Experiment A: In this experiment, we used the traditional RVoG three-stage method to invert forest height (as shown in Figure 4a). In this experiment, the least squares method was used to fit the coherence line and solve the ground phase φ_0, and the complex coherence γ_{HV} was used as the volume scattering complex coherence in the two-dimensional LUT in the third stage:

$$\min_{h_v,\sigma} L = \left\| \gamma_{HV} - e^{j\varphi_0} \frac{p}{p_1} \frac{e^{p_1 h_v} - 1}{e^{p h_v} - 1} \right\| \tag{5}$$

Experiment B: In this experiment, the method of ground phase estimation was the same as that in Experiment A, using the least squares method to fit the coherence line and solving the ground phase φ_0. However, for the volume scattering complex coherence, instead of using γ_{HV}, the complex coherence farthest from φ_0 was chosen according to Equation 6 and written as $\gamma(\omega_{far})$. Its scattering phase center is considered to be closer to the top of the canopy (as shown in Figure 4b):

$$\begin{cases} \max\limits_{\gamma(\omega_{far})} D = \left\| \gamma(\omega) - e^{j\varphi_0} \right\| \\ \min\limits_{h_v,\sigma} L = \left\| \gamma(\omega_{far}) - e^{j\varphi_0} \frac{p}{p_1} \frac{e^{p_1 h_v} - 1}{e^{p h_v} - 1} \right\| \end{cases} \tag{6}$$

The RVoG Three-Stage Inversion Method Combined with Topographic Data

The ground phase φ_0 in the RVoG three-stage inversion method is obtained by fitting the coherence line in different polarization states based on the scattering mechanism of the forest at long-wavelength electromagnetic waves. For the L-band or P-band SAR, radar waves can penetrate the forest canopy to reach the ground and effectively bring back the ground phase information. Therefore, the ground phase could be deduced from the L- or P-band PolInSAR data. However, during real signal capture, the PolInSAR data are affected by the baseline, signal-to-noise ratio, and terrain conditions, so the observed complex coherence could be greatly different from its supposed theoretical value. Further, for the short-wavelength X-band of TanDEM-X, its weak penetration makes it difficult to obtain the surface scattering information, so the distribution of the complex coherence in the complex plane often deviates from the ideal coherence line (Treuhaft *et al.* 1996; Kumar *et al.* 2017; Chen *et al.* 2019). As a result, for the X-band PolInSAR data, the ground phase φ_0 can easily be misestimated.

The topographic data can be used to replace the ground phase solved by the RVoG three-stage method in order to better estimate forest height (Cloude *et al.* 2013; Kugler *et al.* 2014; Qi *et al.* 2019). Therefore, in this study, we used TanDEM-DEM as ground phase information and designed two experimental protocols to explore topographic data–assisted TanDEM-X inversion of forest height (Experiments C and D, as shown in Figure 4c and Figure 4d, respectively).

Experiment C: We replaced the ground phase of Experiment B with the one calculated from the TanDEM-DEM to invert the forest height. First, the height (h_{tan}) of TanDEM-DEM was converted into the ground phase φ_{tan} using the vertical effective wave number kz according to Equation 7, and then φ_{tan} was used as the ground phase in the three-stage algorithm. Then the complex coherence farthest from φ_{tan} was chosen as the volume scattering complex coherence to invert the forest height:

$$\begin{cases} e^{j\varphi_{tan}} = e^{jk_z h_{tan}} \\ \max\limits_{\gamma(\omega_{far-tan})} D = \left\| \gamma(\omega) - e^{j\varphi_{tan}} \right\| \\ \min\limits_{h_v,\sigma} L = \left\| \gamma(\omega_{far-tan}) - e^{j\varphi_{tan}} \frac{p}{p_1} \frac{e^{p_1 h_v} - 1}{e^{p h_v} - 1} \right\| \end{cases} \tag{7}$$

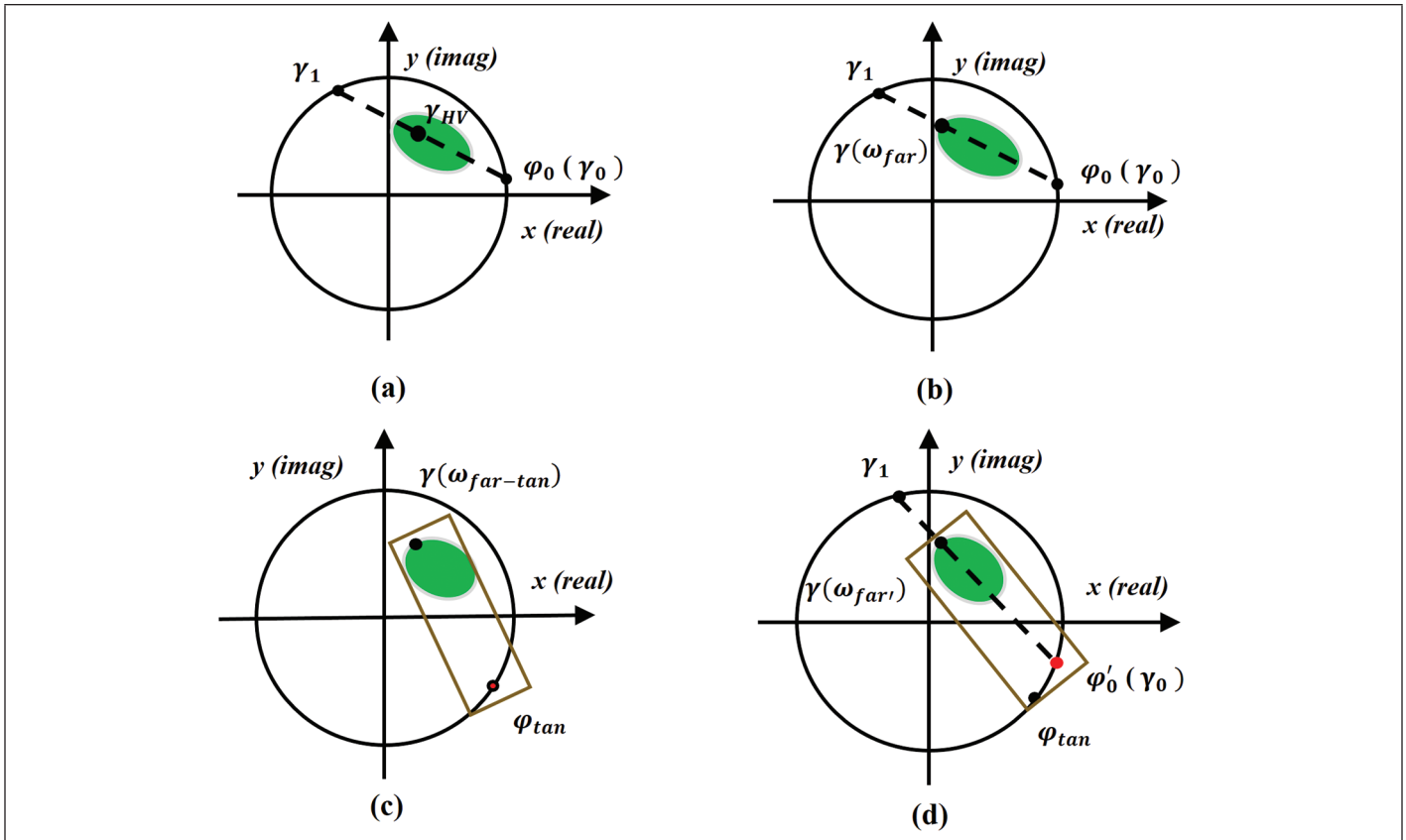

Figure 4. Four experimental plans corresponding to the ground phase and volume scattering complex coherence: (a) Experiment A; (b) Experiment B; (c) Experiment C; (d) Experiment D.

Experiment D: We merged the ground phase calculated from TanDEM-DEM into the three-stage method to invert the forest height. In this experiment, the ground phase $\varphi_{\tan}$ was first calculated from TanDEM-DEM, the ground coherence γ_0 was added into the traditional three-stage algorithm as a coherence point, and then the ground phase φ_0' was estimated according to the coherence line fitting in the three-stage algorithm, and the farthest complex coherence from φ_0' was selected as the volume scattering complex coherence and written as $\gamma(\omega_{\text{far}}')$ in Equation 8. Finally, the forest height was inverted through the LUT. The purpose of this method is to constrain the direction of the coherence line in the traditional three-stage inversion by adding an a priori ground coherence point on the unit circle:

$$\begin{cases} \max\limits_{\gamma(\omega_{\text{far}}')} D = \left\| \gamma(\omega) - e^{j\varphi_0'} \right\| \\ \min\limits_{h_v,\sigma} L = \left\| \gamma(\omega_{\text{far}}') - e^{j\varphi_0'} \dfrac{p}{p_1} \dfrac{e^{p_1 h_v} - 1}{e^{p h_v} - 1} \right\| \end{cases} \tag{8}$$

Evaluation Criteria

Determination coefficient (R^2, Equation 9) and mean square error (MSE, Equation 10) were used to evaluate the inversion accuracy

$$R^2 = 1 - \frac{\sum_{i=1}^{n} (H_i - \hat{H}_i)^2}{\sum_{i=1}^{n} (H_i - \hat{H})^2} \tag{9}$$

$$MSE = \frac{\sum_{i=1}^{n} (H_i - \hat{H}_i)^2}{n} \tag{10}$$

where H_i is the measured height value, $\overline{H}$ is the model-predicted value, $\hat{H}_i$ is the average value of the predicted height.

Results

In this study, the ground-measured forest heights of 42 sample plots were adopted to evaluate the estimation performance of the four experiments. The R^2 and the MSE between the measured forest height and the estimated results were calculated separately for the four experiments, as shown in Figure 5 and Table 2.

Table 2. Results of forest height inversion with different cases.

	Ground Phase	Volume Scattering Complex Coherence	Number of Samples	R^2	MSE (m²)
Experiment A	φ_0	γ_{HV}	42	0.35	7.10
Experiment B	φ_0	$\gamma(\omega_{\text{far}})$		0.38	5.76
Experiment C	$\varphi_{\tan}$	$\gamma(\omega_{\text{far-tan}})$		0.43	5.97
Experiment D	φ_0'	$\gamma(\omega_{\text{far}}')$		0.43	5.27

R^2 = determination coefficient; MSE = mean square error.

Experiment A showed an R^2 of 0.35 and an MSE of 7.10 m². Its scattering plot showed obvious underestimation and overestimation, and a small number of samples were relatively discrete in their distribution. In Experiment B, the result showed an R^2 of 0.38 and an MSE of 5.76 m². Its scattering plot showed that the phenomena of underestimation and overestimation were improved to some extent compared to those in Experiment A. Experiment B used the same method as Experiment A to estimate the ground phase, selecting the complex coherence farthest from the ground phase as the volume scattering complex coherence. As a result, Experiment B had a better forest height estimation than Experiment A, with R^2 increasing from 0.35 to 0.38 and the MSE decreasing by 1.34 m². This indicated that the volume scattering complex coherence optimization was better than directly using γ_{HV} as the volume scattering complex coherence.

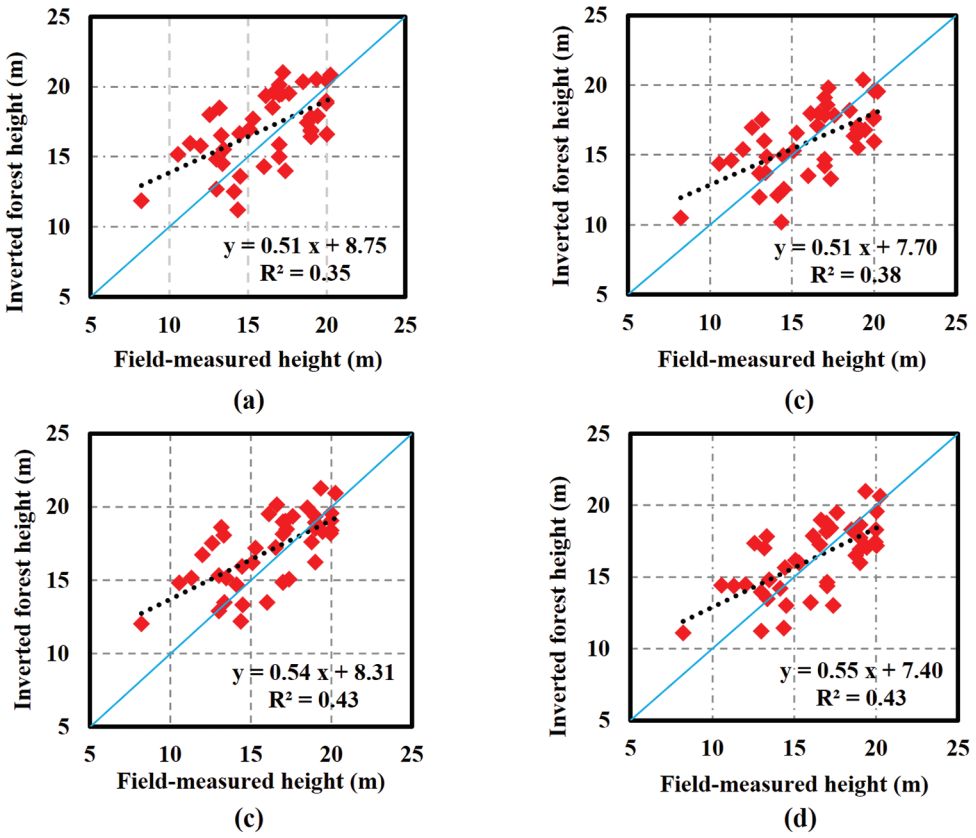

Figure 5. The validation scatter plots for different inversion scheme: (a) Experiment A; (b) Experiment B; (c) Experiment C; (d) Experiment D.

Experiment C had an R^2 of 0.43 and MSE of 5.97 m^2. Its scatter plot shows more convergence in the sample distribution, but underestimation and overestimation are still obvious. The R^2 value was improved significantly compared to those for Experiments A and B. This shows that using φ_{tan} as the ground phase in Experiment C obtained a better forest height, and R^2 increased from 0.38 to 0.43. However, in Experiment C, a small number of samples had relatively large errors, so the MSE difference between Experiments B and C was not significant.

Experiment D obtained the best accuracy among the four experiments, with an R^2 of 0.43 and an MSE of 5.27 m. It was noted in the scattering plot of Experiment D that underestimation and overestimation were improved, with a more convergent distribution for all samples. Compared to Experiment B, Experiment D increased the R^2 value by 12.27% and decreased the MSE by 8.36%. Compared to Experiment C, Experiment D also showed improvements, with the MSE decreasing from 5.97 m^2 to 5.27 m^2. The results show that merging the ground phase calculated from TanDEM-DEM into the three-stage algorithm to invert forest height obtained better results compared to the traditional three-stage algorithm.

Discussion

In this study, TanDEM-DEM data were used to improve the accuracy of forest height inversion based on the TanDEM-X data by using the ground phase φ_{tan} from the DEM, and different experimental protocols were designed for comparison.

Experiment B selected the complex coherence farthest from the ground phase to estimate the volume scattering complex coherence, so the volume scattering phase center in Experiment B was closer to the top of the forest canopy than that used in Experiment A (the traditional three-stage algorithm of RVoG, which employed the coherence of the HV channel as the volume scattering complex coherence. As a result, the inversion result of Experiment B was better than that of Experiment A. This also verified the previous hypothesis. The main scattering mechanism of the complex coherence γ_{HV} of the HV polarization channel is not only volume scattering; it also contains a part of surface scattering, so the ground–volume magnitude ratio $m(\omega)$ of γ_{HV} is not zero where the scattering phase center of the HV channel is not the closest to the top of the canopy among all the complex coherences (Cloude and Papathanassiou 2003). Therefore, it is not accurate to use γ_{HV} directly as the forest height for the inversion of the volume scattering complex coherence. Selecting the volume scattering complex coherence with the ground phase as a reference takes into account the difference between the canopy phase and the ground phase; therefore, the inversion results are improved.

In Experiment C, the ground phase φ_{tan} calculated by TanDEM-DEM was used instead of the ground phase in the traditional three-stage algorithm, and the complex coherence farthest from φ_{tan} was selected as the volume scattering complex coherence. As a result, Experiment C obtained better results than Experiments A and B. It could be concluded that the ground phase φ_{tan} from the TanDEM-DEM is reasonable in the three-phase algorithm and that the volume scattering complex coherence obtained by using φ_{tan} as a reference could be suitable. With high-precision topographic data as a reference, an accurate ground phase can be obtained, thereby improving forest height inversion via TanDEM. Our conclusions in this research are consistent with those of other studies (Cloude *et al.* 2013; Kugler *et al.* 2014; Qi *et al.* 2019). In addition, as mentioned previously, the overall absolute elevation accuracy of TanDEM-DEM is about 3.5 m; when ice, forest-covered areas, and desert are excluded, its absolute elevation accuracy reaches 0.88 m (Rizzoli *et al.* 2017). Compared with the DEM obtained by lidar, the elevation accuracy of TanDEM-DEM is slightly lower. Moreover, error in the interferometric complex coherence affects the final inversion results as well. Although the accuracy improvement is not significant for Experiment C, it shows that without relying on the model solution,

forest height estimation can be achieved by directly using DEM as ground phase information and obtaining more accurate forest heights than using TanDEM-X alone. This is an important reference for the extension and simplification of the RVoG model.

Experiment D also obtained satisfactory results. It added the coherence point ($e^{j\varphi_{tan}}$) from TanDEM-DEM into the fitting of the coherent straight line and produced a more accurate forest height. This indicates that the inclusion of TanDEM-DEM as auxiliary coherence information could change the intersection of the coherence line with the unit circle; in case of errors in the TanDEM-X interferometric complex coherence, the inclusion of TanDEM-DEM could improve the estimation of the ground phase to improve the forest height inversion accuracy. While the accuracy improvement is not significant in this experiment, it is a strategy to improve the RVoG model, which will have a more profound impact on the upcoming spaceborne PolInSAR. We can further validate this approach in future studies.

Nevertheless, the differences among the results of the four experiments are not so significant, and the total inversion accuracy obtained in this study is still relatively lower than that in other studies (Kugler *et al.* 2015; Kumar *et al.* 2017; Qi *et al.* 2019). On the one hand, the number of sample plots (42) is inadequate to show the differences among the experiments. On the other hand, the forest in the testing site is a natural forest with rich understory vegetation and large forest cover, which make the radar scattering signal much more complicated than the ideal scenario in the RVoG model. Meanwhile, the topography of the study area is very complex, with an average slope of 23° and the maximum height difference of 1036 m (according to TanDEM-DEM). In addition, TanDEM-X data could also be affected by the baseline, signal-to-noise ratio, and system errors. All of these factors could bring errors and make the observed complex coherence greatly deviate from the ideal coherence line. Therefore, the final accuracy of the inversion result in this study is not ideal.

In future studies, more accurate verification data, like forest height data from lidar or GEDI, will be adopted. The topographic products of lidar or GEDI and ICESat-2 can also be considered as alternatives in the selection of DEM data.

Conclusions

PolInSAR has great potential for use in forest height inversion at the regional scale, and TanDEM-X provides dual-base station observation, which could avoid the effect of temporal decorrelation, in addition to a high signal-to-noise ratio and high resolution. Therefore, TanDEM-X PolInSAR data have been widely used in forest height inversion. However, due to the weak penetration of the X-band in forests, especially in dense forest areas, it is difficult for TanDEM-X to obtain surface phase information, which has become one of the main reasons for the low accuracy of forest height estimation. Therefore, introducing external topographic data to improve ground phase estimation could be a novel strategy by which to improve the forest height inversion accuracy of TanDEM-X.

In this study, the ground phase φ_{tan} calculated from TanDEM-DEM was used in the RVoG three-stage algorithm to invert the forest height, and four experiments were designed for comparison. It was found that in the RVoG model, the reference ground phase to select the volume scattering complex phase provides higher accuracy in estimating the forest height. Forest height estimation can be achieved by directly using the DEM as ground phase information without relying on the model solution and obtaining more accuracy than TanDEM-X alone; in addition, the highest estimation accuracy was obtained by using the DEM as coherent information. Although the difference in the forest height estimation results of this study is not significant, it proves that high-precision DEM in collaboration with short-wavelength PolInSAR can achieve accurate and fast forest height estimation. This strategy not only will optimize the RVoG model but also will have far-reaching implications for the spaceborne PolInSAR global forest parameter estimation and ecosystem detection.

Acknowledgments

Thanks to the German Aerospace Center (DLR) for providing the TanDEM-X PolInSAR and TanDEM-DEM data needed for this study. This research was funded by the National Natural Science Foundation of China, "Multi-Frequency SAR Polarized Interferometric Data for Forest Tree Height Inversion" (grant no. 42061072); the Major Science and Technology Special Project of Yunnan Provincial Science and Technology Department, "Forest Resources Digital Development and Application in Yunnan" (grant no. 202002AA100007-015); and the Scientific Research Fund Project of Yunnan Provincial Education Department, "Forest Height Inversion from Starborne Microwave Data TanDEM-X Combined with Topographic Data" (grant no. 2022Y579).

References

Bispo, P., M. Pardini, K. P. Papathanassiou, F. Kugler, H. Balzter, D. Rains, J. R. Santos, G. I. Rizaev, K. Tansey, M. N. Santos and L. Araujo. 2019. Mapping forest successional stages in the Brazilian Amazon using forest heights derived from TanDEM-X SAR interferometry. *Remote Sensing of Environment* 232:111194.

Cao, C., Y. Bao, W. Chen, R. Tian, Y. Dang, L. Li and G. Li. 2012. Extraction of forest structural parameters based on the intensity information of high-density airborne light detection and ranging. *Journal of Applied Remote Sensing* 6(1):063533.

Chen, H., A. Beaudoin, D. A. Hill, S. R. Cloude R. S. Skakun and M. Marchand. 2019. Mapping forest height from TanDEM-X interferometer coherence data in Northwest Territories. *Canadian Journal of Remote Sensing* 45(6):1–18.

Chirici, G., M. Chiesi, P. Corona, R. Salvati, D. Papale, L. Fibbi, C. Sirca, D. Spano, P. Duce, S. Marras, G. Matteucci, A. Cescatti and F. Maselli. 2016. Estimating daily forest carbon fluxes using a combination of ground and remotely sensed data. *Journal of Geophysical Research: Biogeosciences* 121(2):266–279.

Cloude, S. R. and K. P. Papathanassiou. 2003. Three-stage inversion process for polarimetric SAR interferometry. *IEE Proceedings—Radar, Sonar and Navigation* 150(3):125–134.

Cloude, S. R. and K. P. Papathanassiou. 1998. Polarimetric SAR interferometry. *IEEE Transactions on Geoscience and Remote Sensing* 36(5):1551–1565.

Cloude, S. R., H. Chen and D. G. Goodenough. 2013. Forest height estimation and validation using Tandem-X polinsar. Pages 1889–1892 in *Proceedings of the IEEE International Geoscience and Remote Sensing Symposium (IGARSS)*, held in Melbourne, VIC, Australia , 21-26 July 2013, New York: IEEE.

Gang, C. and G. J. Hay. 2011. An airborne lidar sampling strategy to model forest canopy height from Quickbird imagery and GEOBIA. *Remote Sensing of Environment* 115(6):1532–1542.

Garestier, F. and T. Le Toan. 2010. Forest modeling for height inversion using single-baseline InSAR/Pol-InSAR data. *IEEE Transactions on Geoscience and Remote Sensing* 48(3):1528–1539.

Gholz, H. L. 1982. Environmental limits on aboveground net primary production, leaf area, and biomass in vegetation zones of the Pacific Northwest. *Ecology* 63(2):469–481.

Goetz, S. and R. Dubayah. 2011. Advances in remote sensing technology and implications for measuring and monitoring forest carbon stocks and change. *Carbon Management* 2(3):231–244.

Graham, L. C. 1974. Synthetic interferometer radar for topographic mapping. *Proceedings of the IEEE* 62(6):763–768.

Hajnsek, I., F. Kugler, S. K. Lee and K. P. Papathanassiou. 2009. Tropical-forest-parameter estimation by means of Pol-InSAR: The INDREX-II campaign. *IEEE Transactions on Geoscience and Remote Sensing* 47(2):481–493.

Hall, F. G., K. Bergen, J. B. Blair, R. Dubayah, R. Houghton, G. Hurtt, J. Kellndorfer, M. Lefsky, J. Ranson, S. Saatchi, H. H. Shugart and D. Wickland. 2011. Characterizing 3D vegetation structure from space: Mission requirements. *Remote Sensing of Environment* 115(11):2753–2775.

Houghton, R. A. 2005. Aboveground forest biomass and the global carbon balance. *Global Change Biology* 11:945–958.

Huang, W., G. Sun, R. Dubayah, Z. Zhang and W. Ni. 2012. Mapping forest above-ground biomass and its changes from LVIS waveform data. Pages 6561–6564 in *Proceedings of the IEEE International Geoscience and Remote Sensing Symposium (IGARSS)* , held in Munich, Germany, 22-27 July 2012, New York: IEEE.

Kugler, F., S. K. Lee, I. Hajnsek and K. Papathanassiou. 2015. Forest height estimation by means of Pol-InSAR data inversion: The role of the vertical wavenumber. *IEEE Transactions on Geoscience and Remote Sensing* 53(10):5294–5311.

Kugler, F., D. Schulze, I. Hajnsek, H. Pretzsch and K. P. Papathanassiou. 2014. TanDEM-X Pol-InSAR performance for forest height estimation. *IEEE Transactions on Geoscience and Remote Sensing* 52(10):6404–6422.

Kumar, S., H. Govil, P. K. Srivastava and S.P.S. Kushwaha. 2020. Spaceborne multifrequency PolInSAR-based inversion modelling for forest height retrieval. *Remote Sensing* 12(24):4042.

Kumar, S., R. D. Garg, S.P.S. Kushwaha, W.G.N.N. Jayawardhana and S. Agarwal. 2017. Bistatic PolInSAR inversion modelling for plant height retrieval in a tropical forest. *Proceedings of the National Academy of Sciences, India Section A: Physical Sciences* 87(4):817–826.

Liao, Z. B. He, A. van Dijk, X. Bai and X. Quan. 2018. The impacts of spatial baseline on forest canopy height model and digital terrain model retrieval using P-band PolInSAR data. *Remote Sensing of Environment* 210:403–421.

Maltamo, M., H. Kinnunen, A. Kangas and L. Korhonen. 2020. Predicting stand age in managed forests using National Forest Inventory field data and airborne laser scanning. *Forest Ecosystems* 7(1):1–11.

Managhebi, T., Y. Maghsoudi and M.J.V. Zoej. 2018. A volume optimization method to improve the three-stage inversion algorithm for forest height estimation using PolInSAR data. *IEEE Geoscience and Remote Sensing Letters* 15(8):1214–1218.

Papathanassiou, K and S. R. Cloude. 2001. Single-baseline polarimetric SAR interferometry. *IEEE Transactions on Geoscience and Remote Sensing* 39(11):2352–2363.

Persson, H. J., H. Olsson, M. J. Soja, L. M. Ulander and J. E. Fransson. 2017. Experiences from large-scale forest mapping of Sweden using TanDEM-X data. *Remote Sensing* 9(12):1253.

Qi, W., S. K. Lee, S. Hancock, S. Luthcke, H. Tang, J. Armston and R. Dubayah. 2019. Improved forest height estimation by fusion of simulated GEDI LiDAR data and TanDEM-X InSAR data. *Remote Sensing of Environment* 221:621–634.

Rizzoli, P., M. Martone, C. Gonzalez, C. Wecklich, D. B. Tridon, B. Bräutigam, D. Schulze, T. Fritz and M. Huber. 2017. Generation and performance assessment of the global TanDEM-X digital elevation model. *ISPRS Journal of Photogrammetry and Remote Sensing* 132:119–139.

Schlund, M., P. Magdon, B. Eaton, C. Aumann and S. Erasmi. 2019. Canopy height estimation with TanDEM-X in temperate and boreal forests. *International Journal of Applied Earth Observation and Geoinformation* 82:101904.

Silva, C. A., L. Duncanson, S. Hancock, A. Neuenschwander, N. Thomas, M. Hofton, L. Fatoyinbo, M. Simard, C. Z. Marshak and J. Armston. 2021. Fusing simulated GEDI, ICESat-2 and NISAR data for regional aboveground biomass mapping. *Remote Sensing of Environment* 253:112234.

Treuhaft, R. N., M. Moghaddam and J. J. van Zyl. 1996. Vegetation characteristics and underlying topography from interferometer radar. *Radio Science* 31(6):1449–1485.

Wang, C., L. Wang, H. Fu, Q. Xie and J. Zhu. 2016. The impact of forest density on forest height inversion modeling from polarimetric InSAR data. *Remote Sensing* 8(4):291.

Wang, D., B. Wan, J. Liu, Y. Su, Q. Guo, P. Qiu and X. Wu. 2020. Estimating aboveground biomass of the mangrove forests on northeast Hainan Island in China using an upscaling method from field plots, UAV-LiDAR data and Sentinel-2 imagery. *International Journal of Applied Earth Observation and Geoinformation* 85:101986.

Xie, Q. H., C. C. Wang, J. J. Zhu and H. Q. Fu. 2015. Forest height inversion by combining S-RVOG model with terrain factor and PD coherence optimization. *Acta Geodaetica et Cartographica Sinica* 44(6):686.

Xu, M., H. Xiang, H. Yun, X. Ni, W. Chen and C. X. Cao. 2019. Retrieval of forest canopy height jointly using airborne LiDAR and ALOS PALSAR data. *Journal of Applied Remote Sensing* 14(2):022203.

Zhang, L., B. Duan and B. Zou. 2017. Research on inversion models for forest height estimation using polarimetric SAR interferometry. *International Archives of the Photogrammetry, Remote Sensing and Spatial Information Sciences* 42(0):659–663.

SUSTAININGMEMBERS

ACI USA Inc.
Weston, Florida
https://acicorporation.com/
Member Since: 2/2018

Aerial Services, Inc.
Cedar Falls, Iowa
www.AerialServicesInc.com
Member Since: 5/2001

Airworks Solutions Inc.
Boston, Massachusetts
Member Since: 3/2022

Applanix
Richmond Hill, Ontario, Canada
http://www.applanix.com
Member Since: 7/1997

Ayres Associates
Madison, Wisconsin
www.AyresAssociates.com
Member Since: 1/1953

Cardinal Systems, LLC
Flagler Beach, Florida
www.cardinalsystems.net
Member Since: 1/2001

Dewberry
Fairfax, Virginia
www.dewberry.com
Member Since: 1/1985

Esri
Redlands, California
www.esri.com
Member Since: 1/1987

Geographic Imperatives LLC
Centennial, Colorado
Member Since: 12/2020

GeoWing Mapping, Inc.
Richmond, California
www.geowingmapping.com
Member Since: 12/2016

GPI Geospatial Inc.
Orlando, Florida
www.aca-net.com
Member Since: 1/1994

Halff Associates, Inc.
Richardson, Texas
www.halff.com
Member Since: 8/2021

Keystone Aerial Surveys, Inc.
Philadelphia, Pennsylvania
www.kasurveys.com
Member Since: 1/1985

Kucera International
Willoughby, Ohio
www.kucerainternational.com
Member Since: 1/1992

L3Harris Technologies
Broomfield, Colorado
www.l3harris.com
Member Since: 6/2008

Merrick & Company
Greenwood Village, Colorado
www.merrick.com
Member Since: 4/1995

Miller Creek Associates
SeaTac Washington
www.mcamaps.com
Member Since: 12/2014

Nearmap
South Jordan, Utah
www.nearmap.com
Member Since: 6/2023

NV5 Geospatial
Sheboygan Falls, Wisconsin
www.quantumspatial.com
Member Since: 1/1974

Pickett and Associates, Inc.
Bartow, Florida
www.pickettusa.com
Member Since: 4/2007

PixElement
Belmont, Michigan
https://pixelement.com
Member Since: 2/2017

Riegl USA, Inc.
Orlando, Florida
www.rieglusa.com
Member Since: 11/2004

Robinson Aerial Surveys, Inc.(RAS)
Hackettstown, New Jersey
www.robinsonaerial.com
Member Since: 1/1954

Sanborn Map Company
Colorado Springs, Colorado
www.sanborn.com
Member Since: 10/1984

Surdex Corporation
Chesterfield, Missouri
www.surdex.com
Member Since: 12/2011

Surveying And Mapping, LLC (SAM)
Austin, Texas
www.sam.biz
Member Since: 12/2005

T3 Global Strategies, Inc.
Bridgeville, Pennsylvania
https://t3gs.com/
Member Since: 6/2020

Towill, Inc.
San Francisco, California
www.towill.com
Member Since: 1/1952

Woolpert LLP
Dayton, Ohio
www.woolpert.com
Member Since: 1/1985

SUSTAININGMEMBER**BENEFITS**

Membership

- ✓ Provides a means for dissemination of new information
- ✓ Encourages an exchange of ideas and communication
- ✓ Offers prime exposure for companies

Benefits of an ASPRS Membership

- Complimentary and discounted Employee Membership*
- E-mail blast to full ASPRS membership*
- Professional Certification Application fee discount for any employee
- Member price for ASPRS publications
- Discount on group registration to ASPRS virtual conferences
- Sustaining Member company listing in ASPRS directory/website
- Hot link to company website from Sustaining Member company listing page on ASPRS website
- Press Release Priority Listing in *PE&RS* Industry News
- Priority publishing of Highlight Articles in *PE&RS* plus, 20% discount off cover fee
- Discount on *PE&RS* advertising
- Exhibit discounts at ASPRS sponsored conferences (exception ASPRS/ILMF)
- Free training webinar registrations per year*
- Discount on additional training webinar registrations for employees
- Discount for each new SMC member brought on board (Discount for first year only)

*quantity depends on membership level

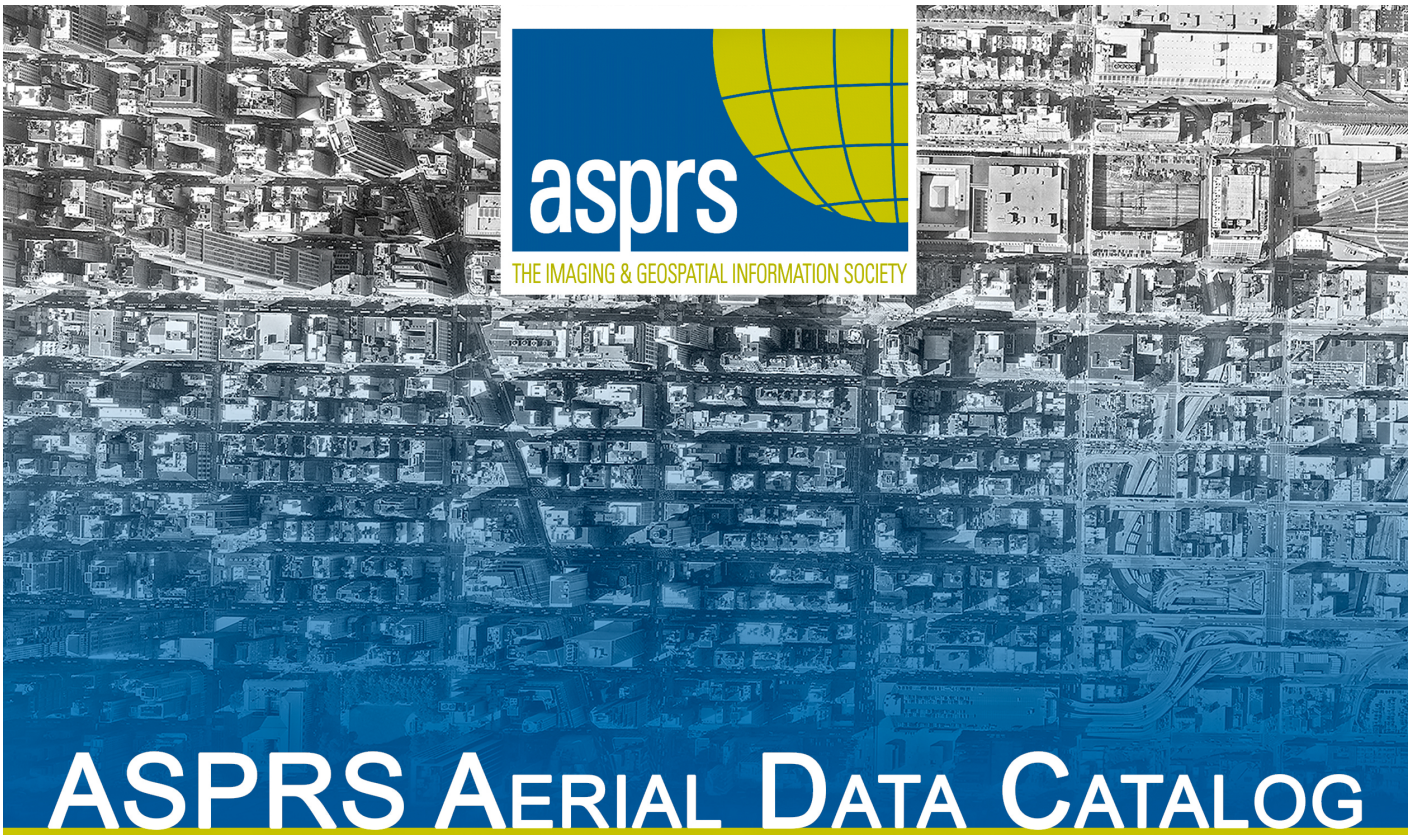

asprs
THE IMAGING & GEOSPATIAL INFORMATION SOCIETY

ASPRS Aerial Data Catalog

"The Source for Finding Aerial Collections"

http://dpac.asprs.org

The ASPRS Aerial Data Catalog is a tool allowing owners of aerial photography to list details and contact information about individual collections.

By providing this free and open metadata catalog with no commercial intrests, the Data Preservation and Archiving Committee (DPAC) aims to provide a definitive metadata resource for all users in the geospatial community to locate previously unkown imagery.

DPAC hopes this Catalog will contribute to the protection and preservation of aerial photography around the world!

ASPRS Members: We Need Your Help!
There are three ways to get involved

1 USE — Use the catalog to browse over 5,000 entries from all 50 states and many countries. Millions of frames from as early as 1924!

2 SUPPLY — Caretakers of collections, with or without metadata, should contact DPAC to add their datasets to the catolog free of charge!

3 TELL — Spread the word about the catalog! New users and data collections are key to making this a useful tool for the community!

For More Details or To Get Involved Contact:

David Ruiz • druiz@quantumspatial.com • 510-834-2001 OR David Day • dday@kasurveys.com • 215-677-3119

Special Advertising Opportunities

FRONT COVER SPONSORSHIP

A *PE&RS* cover sponsorship is a unique opportunity to capture the undivided attention of your target market through three premium points of contact.

1— *PE&RS* FRONT COVER

(Only twelve available, first-come, first-served)
PE&RS is world-renowned for the outstanding imagery displayed monthly on its front cover—and readers have told us they eagerly anticipate every issue. This is a premium opportunity for any company, government agency, university or non-profit organization to provide a strong image that demonstrates their expertise in the geospatial information industry.

2— FREE ACCOMPANYING "HIGHLIGHT" ARTICLE

A detailed article to enhance your cover image is welcome but not a condition of placing an image. Many readers have asked for more information about the covers and your article is a highly visible way to tell your story in more depth for an audience keenly interested in your products and services. No article is guaranteed publication, as it must pass ASPRS editorial review. For more information, contact Rae Kelley at rkelley@asprs.org.

3— FREE TABLE OF CONTENTS COVER DESCRIPTION

Use this highly visible position to showcase your organization by featuring highlights of the technology used in capturing the front cover imagery. Limit 200-word description.

Terms: Fifty percent nonrefundable deposit with space reservation and payment of balance on or before materials closing deadline.

Cover Specifications: Bleed size: 8 5/8" × 11 1/4", Trim: 8 3/8" × 10 7/8"

PRICING

	Sustaining Member Exhibiting at a 2023 ASPRS Conference	Sustaining Member	Exhibitor	Non Member
Cover 1	$1,850	$2,000	$2,350	$2,500

Belly Bands, Inserts, Outserts & More!

Make your material the first impression readers have when they get their copy of *PE&RS*. Contact Bill Spilman at bill@innovativemediasolutions.com

VENDOR SEMINARS

ASPRS Sustaining Members now have the opportunity to hold a 1-hour informational session as a Virtual Vendor Seminar that will be free to all ASPRS Members wishing to attend. There will be one opportunity per month to reach out to all ASPRS Members with a demonstration of a new product, service, or other information. ASPRS will promote the Seminar through a blast email to all members, a notice on the ASPRS web site home page, and ads in the print and digital editions of *PE&RS*.

The Virtual Seminar will be hosted by ASPRS through its Zoom capability and has the capacity to accommodate 500 attendees.

Vendor Seminars	
Fee	$2,500 (no discounts)

DIGITAL ADVERTISING OPPORTUNITIES

EMPLOYMENT PROMOTION

When you need to fill a position right away, use this direct, right-to-the-desktop approach to announce your employment opportunity. The employment opportunity will be sent once to all ASPRS members in our regular Wednesday email newsletter to members, and will be posted on the ASPRS Web site for one month. This type of advertising gets results when you provide a web link with your text.

Employment Opportunity	Net Rate
30-Day Web + 1 email	$500/opportunity
Web-only (no email)	$300/opportunity

Do you have multiple vacancies that need to be filled? Contact us for pricing details for multiple listings.

NEWSLETTER DISPLAY ADVERTISING

Your vertical ad will show up in the right hand column of our weekly newsletter, which is sent to more than 3,000 people, including our membership and interested parties. **Open Rate: 32.9%**

Newsletter vertical banner ad	Net Rate
180 pixels x 240 pixels max	$500/opportunity

DEDICATED CONTENT EMAIL BLAST

Send a dedicated email blast to the ASPRS email list. Advertiser supplies HTML (including images). Lead time: 14 days.

Materials	Net Rate
Advertiser supplies HTML, including images.	$3000/ opportunity

PE&RS Digital Edition

Digital Edition Announcement E-Mail: 5,800+

PE&RS is available online in both a public version that is available to anyone but does not include the peer-reviewed articles, and a full version that is available to ASPRS members only upon login.

The enhanced version of *PE&RS* contains hot links for all ASPRS Sustaining Member Companies, as well as hot links on advertisements, ASPRS Who's Who, and internet references.

Become a sponsor today!

The e-mail blast sponsorship opportunity includes a **180 x 240 pixel ad** in the email announcement that goes out to our membership announcing the availability of the electronic issue.

Digital Edition Opportunities	Net Rate
E-mail Blast Sponsorship*	$1,000

PUBLISHING OPEN-ACCESS IN *PE&RS* IS NOW EASIER!

ASPRS is changing the subscription model of our monthly journal, *PE&RS*. ASPRS is waiving open-access fees for primary authors from subscribing institutions. Additionally, primary authors who are Individual Members of ASPRS will be able to publish one open-access article per year at no cost and will receive a 50% discount on open-access fees for additional articles.

- **Open Access matters!** By providing unrestricted access to research we can advance the geospatial industry and provide research that is available to everyone.
- **Institutions and authors receive more recognition!** Giving permission to everyone to read, share, reuse the research without asking for permission, as long as the author is credited.
- **Reputation matters!** Known for its high standards, *PE&RS* is the industry leading peer-review journal. Adding open access increases authors' visibility and reputation for quality research.
- **Fostering the geospatial industry!** Open access allows for sharing without restriction. Research is freely available to everyone without an embargo period.

Under the previous subscription model, authors and institutions paid $1500 or more in open-access fees per article. This will represent a significant cost savings. Open-access publications benefit authors through greater visibility of their work and conformance with open science mandates of funding agencies.

Subscriptions asprs.org/subscribe
Membership asprs.org/membership

asprs THE IMAGING & GEOSPATIAL INFORMATION SOCIETY